REAL-TIME METHODS IN NEURAL ELECTROPHYSIOLOGY TO IMPROVE EFFICACY OF DYNAMIC CLAMP

A Dissertation
Presented to
The Academic Faculty

by

Risa J. Lin

In Partial Fulfillment
of the Requirements for the Degree
Doctor of Philosophy in the
Interdisciplinary Bioengineering Graduate Program

Department of Biomedical Engineering
Georgia Institute of Technology
August 2012

REAL-TIME METHODS IN NEURAL ELECTROPHYSIOLOGY TO IMPROVE EFFICACY OF DYNAMIC CLAMP

Approved by:

Professor Robert Butera, Advisor
School of Electrical and Computer Engineering
Georgia Institute of Technology

Professor Dieter Jaeger
Department of Biology
Emory University

Associate Professor Steve Potter
Dept. of Biomedical Engineering
Georgia Institute of Technology

Associate Professor Astrid Prinz
Department of Biology
Emory University

Assistant Professor Christopher Rozell
School of Electrical and Computer Engineering
Georgia Institute of Technology

Date Approved: 14 May 2012

ACKNOWLEDGEMENTS

My family, you have no idea what I've been working on but there was never any question that I would come out the other side. Frances, for backing me up about graduate school being as demanding as a "real job" and how nothing I do translates easily into Chinese. My friends, for sharing my excitement about each small accomplishment even when I have to re-explain what a neuron or Linux is. Sadiya, Michelle, for always thinking it was perfectly natural for me to have my head buried wherever it happened to be at the time. Zheng, MingJackPo, Patrick, Steve, Bill, for always being only a phone call away.

Throughout this work, specific research results would not be possible without the contributions from a number of people. I want to thank Steve Feng and Volker Gauck for performing the dynamic clamp experiments. Svenja Metz, Eric Hendrickson, Nathan Schultheiss, and Jeremy Edgerton all provided invaluable discussion for the simulation work. I want to thank Jonathan Bettencourt, Francis Ortega and many members of John White's and David Christini's research labs in providing technical support, user testing and feedback, and inspiring new ideas for the development of RTXI. I need to thank Henning Voss and members of Chris Rozell's lab for useful discussions and perspectives about Kalman filtering and statistical inference when I was very much still a n00b.

Finally, I need to thank my committee members and especially my advisors, Robert Butera and Dieter Jaeger. I've enjoyed a considerable amount of freedom to not only explore the scientific and technical challenges that I find interesting but also get involved in numerous aspects of engineering education and professional development at Georgia Tech. They always brought me back to focus on the biological significance of my work and I apologize now for all the time they spent wondering what I was doing with my time. This work was supported by the National Institute of Mental Health under Grant R01-MH065634 to Dieter Jaeger, the National Institutes of Health under Grant 2-R01RR020115-05 to David Christini, John White, and Robert Butera, and a NSF IGERT fellowship DGE-0333411.

TABLE OF CONTENTS

LIST OF TABLES

LIST OF FIGURES

SUMMARY

In the central nervous system, most of the processes ranging from ion channels to neuronal networks occur in a closed loop, where the input to the system depends on its output. In contrast, most experimental preparations and protocols operate autonomously in an open loop and do not depend on the output of the system. Real-time software technology can be an essential tool for understanding the dynamics of many biological processes by providing the ability to precisely control the spatiotemporal aspects of a stimulus and to build activity-dependent stimulus-response closed loops. So far, application of this technology in biological experiments has been limited primarily to the dynamic clamp, an increasingly popular electrophysiology technique for introducing artificial conductances into living cells. Since the dynamic clamp combines mathematical modeling with electrophysiology experiments, it inherits the limitations of both, as well as issues concerning accuracy and stability that are determined by the chosen software and hardware. In addition, most dynamic clamp systems to date are designed for specific experimental paradigms and are not easily extensible to general real-time protocols and analyses. The long-term goal of this research is to develop a suite of real-time tools to evaluate the performance, improve the efficacy, and extend the capabilities of the dynamic clamp technique and real-time neural electrophysiology. We demonstrate a combined dynamic clamp and modeling approach for studying synaptic integration, a software platform for implementing flexible real-time closed-loop protocols, and the potential and limitations of Kalman filter-based techniques for online state and parameter estimation of neuron models.

CHAPTER I

INTRODUCTION

In the central nervous system, most of the processes ranging from ion channels to neuronal networks occur in a closed loop, where the input to the system depends on its output. In contrast, most experimental preparations and protocols operate autonomously in an open loop and do not depend on the output of the system. Real-time software technology can be an essential tool for understanding the dynamics of many biological processes by providing the ability to precisely control the spatiotemporal aspects of a stimulus and to build activity-dependent stimulus-response closed loops. So far, application of this technology in biological experiments has been limited primarily to the dynamic clamp, an increasingly popular electrophysiology technique for introducing artificial conductances into living cells. Since the dynamic clamp combines mathematical modeling with electrophysiology experiments, it inherits the limitations of both, as well as issues concerning accuracy and stability that are determined by the chosen software and hardware. In addition, most dynamic clamp systems to date are designed for specific experimental paradigms and are not easily extensible to general real-time protocols and analyses. The long-term goal of this research is to develop a suite of real-time tools to evaluate the performance, improve the efficacy, and extend the capabilities of the dynamic clamp technique and real-time neural electrophysiology. The work described here covers the following three specific aims:

Aim 1: Use a morphologically realistic model of a deep cerebellar neuron to simulate dynamic clamp and compare the effects of purely somatic versus distributed dendritic inputs on synaptic integration.

The dynamic clamp applies conductance inputs at the location of current injection whereas biological inputs are distributed throughout the cell. We used computer simulations of a morphologically realistic model of DCN neurons to compare the effects of purely somatic (simulating dynamic clamp) versus distributed dendritic inputs. The same conductance

stimuli and data analysis methods used in published experiments were applied to the model. This work resulted in a set of benchmarks that can be used to assess synaptic integration and the validity of dynamic clamp results in neuronal cell types for which such models are available.

Aim 2: Implement algorithms in RTXI for closed-loop feedback, online data analysis, and online data visualization for neural electrophysiology experiments.

This aim seeks to develop a framework within the real-time RTXI computing platform for implementing closed-loop algorithms with online analysis of electrophysiological data. This includes event-triggered data analysis and stimulation, real-time data visualization, and online optimization of model parameters. These toolboxes allow users to quickly implement sophisticated experimental protocols and real-time feedback to inform experiment decisions.

Aim 3: Assess the potential of the unscented Kalman filter for online state and parameter estimation in neurophysiology experiments.

The Kalman filter is a recursive technique that gives the optimal solution to the filtering problem in which the state of a dynamical system is estimated from noisy measurements, which themselves are a function of the system state. The goal of this aim is to investigate applications of the Kalman filter for tracking unobservable states and parameters of the model system during a dynamic clamp experiment. The limitations of this approach were assessed in the context of errors in model assumptions, measurement error, and highly nonlinear, nonstationary system behavior such as bursting activity.

CHAPTER II

BACKGROUND AND SIGNIFICANCE

2.1 Dynamic Clamp

Traditionally, the properties of electrically excitable cells are assessed using current clamp and voltage clamp electrophysiology protocols. In *current clamp*, an electrical current waveform is specified and applied to the cell through a microelectrode while the transmembrane potential is recorded. In *voltage clamp*, a desired voltage waveform is specified and analog circuitry is used to determine and inject a current that is necessary to maintain, or clamp, the membrane potential at the specified values. The *dynamic clamp* allows the insertion of artificial membrane conductances, such as ion channels, by injecting current that is a function of the cell's membrane potential. The injected current is computed by computer software or analog circuitry based on the equivalent circuit model of the membrane of an excitable cell (Fig. 1). The artificial conductance is effectively in parallel with other membrane processes, each of which contributes to the total transmembrane current.

The total transmembrane current is related to changes in the membrane potential, V_m, through the following equation:

$$C_m \frac{dV_m}{dt} = -\Sigma I_i \tag{1}$$

where C_m is the membrane capacitance. Any conductance that can be described mathematically can be applied to a neuron using the dynamic clamp. The current passing through an ion channel, for example, is often described by Ohm's law using the following conductance-based equation:

$$I_i = g_i(V_m)(V_m - E_i) \tag{2}$$

$$g_i(V_m) = \bar{g}_i m^{\mathrm{p}} h^{\mathrm{q}} \tag{3}$$

where $\bar{g}$ is the maximal conductance, and m and h are voltage-dependent activation and inactivation gating variables (p and q are integers) that describe the kinetic activation of

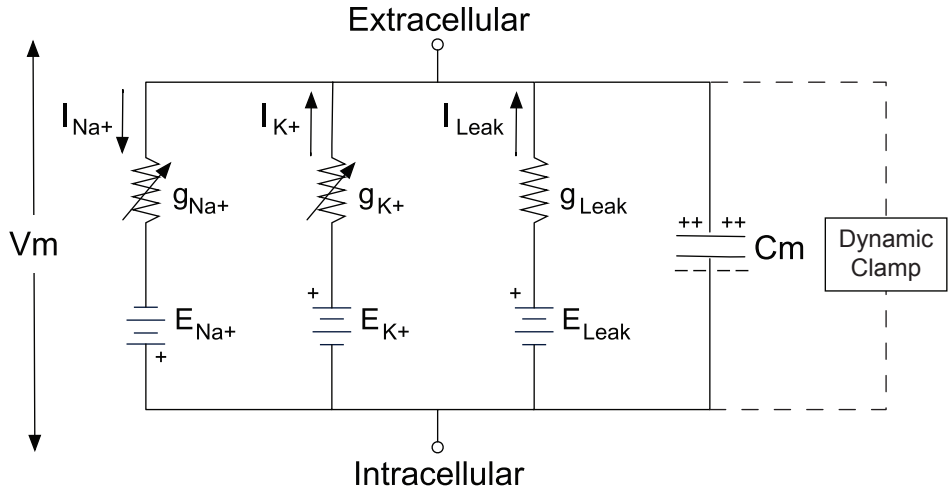

Figure 1: Equivalent circuit model of the membrane of an excitable cell where V_m represents the transmembrane potential, C_m represents the membrane capacitance, and each conductance is defined by a reversal potential E_i and a conductance g_i. In this model, the voltage-dependent sodium and potassium ion channels are depicted as variable resistors where $g_i = g_i(V_m)$. The reversal potential (or equilibrium potential) of an ion is the value of transmembrane voltage at which diffusive and electrical forces counterbalance, so that there is no net ion flow across the membrane. The reversal potential is represented as a battery since the potential difference $V_\mathrm{m} - E_i$ gives the driving force across the membrane for that ionic current.

the channel. Gating variables have values between 0 and 1 to scale the channel conductance and are typically described by a first order differential equation:

$$\frac{dx}{dt} = \frac{x_\infty(V_m) - x}{\tau_x(V_m)} \tag{4}$$

where x_∞ is the steady-state value of the gating variable and τ_x is its associated time constant of activation or inactivation. The membrane potential is re-sampled and the equations are re-evaluated on every computational cycle of the dynamic clamp system. As such, the dynamic clamp is also sometimes termed *conductance clamp* or *conductance injection*.

While the dynamic clamp was first demonstrated in cardiac electrophysiology to electrically couple embryonic chick myocytes [262], the technique was independently introduced [207, 220] and is now more prevalent in neural electrophysiology [70, 90, 197]. Applications of this technique include the insertion of non-native ion channels (a virtual "knock-in"), subtraction of native ion channels (a virtual "knock-out"), and simulation of synapses and electrical gap junctions to create small networks of biological and/or simulated neurons.

By varying the parameter values of a model channel or synapse, experiments can be conducted to determine how these properties shape membrane dynamics and neuron activity. These approaches have made the dynamic clamp a valuable tool for studying the intrinsic properties of single neurons and the behavior of small neural networks.

Dynamic clamp studies have also made important contributions to our understanding of neuronal dynamics under in vivo-like conditions. Artificial synaptic input can be constructed from pre-recorded activity of presynaptic neurons but is more commonly based on statistical descriptions of noisy conductance waveforms. The relationship between the amount of input conductance and the membrane voltage can be highly nonlinear and there are important differences between current-based and conductance-based inputs in neurons. This is significant when considering that neurons in vivo receive a constant barrage of synaptic inputs which can easily reach thousands of events per second. This condition results in a high-conductance state of these neurons in which synaptic conductances are severalfold larger than the leak conductance [9, 23, 29, 113].

In the cortex, these conductances are so large that they increase the total membrane conductance enough to reduce the neuron's effective time constant, decrease the input resistance, and result in a significantly depolarized average membrane potential [66, 184]. At the same time, the amplitude of propagating dendritic signals is diminished because of synaptic shunting. Functionally, this affects the efficacy of distal inputs to impact somatic spiking and could allow a neuron to independently integrate synaptic inputs received on different parts of the dendritic tree. In a high conductance state, the intracellular membrane potential can also closely track an effective reversal potential composed of the instantaneous synaptic inputs, allowing the neuron to resolve higher frequency inputs [66, 127, 222]. This high conductance state has been shown to enhance the cell's responsiveness to small inputs, also known as its gain [42, 66, 216], and can change the signal integration of synaptic input, creating distinct modes of firing patterns [65, 212, 231, 264].

Fluctuating background conductance input, or synaptic noise, also causes subthreshold membrane potential fluctuations, creating a regime in which spike generation and output spike patterns are better described probabilistically. Thus, the statistics of current-based

versus conductance-based input, such as correlations and relative balance between excitation and inhibition, are translated differently into output statistics such as the membrane potential distribution, the distribution of interspike intervals (ISIs), the coefficient of variation (CV), and the mean and variance of the neuron's output firing rate [73, 144, 211, 214, 240]. Together, these spatiotemporal factors result in a dynamical behavior of the neuron that is usually quite different from the intrinsic dynamics of the voltage-gated currents. An important implication of these considerations is that data from brain slice recordings absent this synaptic background noise should not be taken to represent the in vivo condition. The dynamic clamp has been used in many vertebrate cell types such as cortical pyramidal neurons [173, 179, 216], hippocampal CA1 pyramidal neurons [38, 75, 138, 192, 193, 251], neurons of the rat entorhinal cortex [76, 97, 140, 186], various types of thalamic neurons [51, 52, 59, 147, 185, 226, 234, 244], and midbrain dopaminergic neurons [60, 98, 161, 162].

Results from dynamic clamp experiments must be carefully interpreted due to several experimental limitations. Space-clamp problems arise in that the injected current is limited to a space around the recording electrode. Since current can usually only be injected at the soma, the dynamic clamp may be a poor approximation of dendritic input in some cell types. In some experimental studies, an artificial dendrite is modeled as well to simulate the cable effects of synaptic inputs propagating to the action potential initiation zone [121]. This issue is explored in Chapter 3. In most cells, the dynamic clamp is operated in discontinuous current clamp mode in which a single electrode switches between recording and current injection states. In this configuration, it is not possible to inject large conductances that approach the magnitude of the cell's intrinsic resting conductance while still accurately recording the membrane potential. The injected current induces a voltage drop across the electrode and causes measurement accuracies that are propagated through the closed feedback loop in the dynamic clamp system and may cause ringing artifacts in the recording [31, 126, 194, 195]. In larger cells, this effect can be minimized by using two electrodes, one to record and one to inject current. Researchers also typically use the same ion channel or synapse model parameters for all cells used in an experiment, assuming that neurons of the same cell type have identical intrinsic properties, both within an animal and between

animals [93]. There usually is not time during an experiment to manually adjust the model to optimal parameters for each cell. New techniques that can be implemented on modern real-time experiment platforms as described in Chapter 4 can address these issues.

2.2 Real-time Platforms for Closed-Loop Experiments

Using real-time control, scientists can quantify biological function via perturbations that change according to closed-loop analysis of measured system variables, rather than being restricted to measuring responses to pre-defined open-loop stimuli. There is a wide range of biological research endeavors for which real-time control can offer insight that cannot be obtained with traditional methods. In addition to dynamic clamp, these include (i) adaptive control of cardiac [43, 80, 100] and neuronal excitable systems [191, 217, 254], (ii) postural control via force-platform center-of-pressure feedback modulation of galvanic vestibular stimulation [180, 205], (iii) sensory and motor prostheses using brain computer interfaces [10, 34, 152, 168], and (iv) deep brain stimulation as therapy for, or investigation of, various brain disorders [32, 119, 141].

So far, real-time software technology has been primarily limited to various implementations of the dynamic clamp technique in cardiac and neural electrophysiology. These implementations span a combination of hardware and software solutions and include applications that run under a variety of operating systems for personal desktop computers, systems that utilize dedicated embedded processors or DSP boards for real-time computing, and systems that consist predominantly of analog components (Table 1). Other systems have been developed using commercial platforms such as the Real-Time Workshop® combined with the Simulink® graphical programming tool (MATLAB™, Natick, MA) [61, 65, 156, 228], LabVIEW™with the LabVIEW Real-Time Module (National Instruments, Austin, TX) [73, 74, 143], and LabWindows™/CVI (National Instruments) [15, 175]. These and other Windows-based dynamic clamp systems are popular for their ease of installation and users' previous familiarity with the software. However, most of these systems contain a limited set of template models for specifying artificial ion channel and synapses, have limited mechanisms by which users can create new custom models or experimental protocols, and require

Table 1: A review of dynamic clamp implementations reported in the literature. Systems that are programmable only through a GUI or custom scripting language typically have a limited set of template models that accept user-specified parameters for artificial ion channels and synapses. The "programming language" specified for each system is that used to specify model parameters, describe new models, or implement custom experimental protocols.

	Name	**Platform**	**Programming Language**	**RT GUI**	**Rate (kHz)**
1993	Sharp et. al [220, 221]	DOS			3-5
	Robinson & Kawai [207]	Embedded	-		17
1995	DCLAMP [1] [102, 139]	DOS			1-2
	LeMasson et. al [146]	Embedded			2.5
1996	RCC [123]	DOS + Analog			40
1998	Verheijck et. al [250]	DOS	Borland Pascal		7
1999	Dynamic Clamp [15]	Windows XP	C, GUI	✓	2-5
2001	SM-1 [2] [103, 208]	Analog	-		25-50
	DYNCLAMP2/4 [187]	Windows NT/2000	C++, GUI		10 [3]
	RTLDC [67, 257]	RT-Linux	C	✓	20-40
	MRCI [36, 201]	RT-Linux	Script		30
2003	Lien & Jonas [157, 252]	Embedded	C++	✓	80
2004	RT-NEURON [59, 112, 213]	Windows	Script, GUI	✓	10-15
	G-clamp [4, 143, 260]	Embedded	LabVIEW GUI	✓	48
2005	ITC-18 [4]	Analog	-		50
	DynaClamp [22]	RT-Linux	C++		25
2006	StdpC [137, 178]	Windows NT/2000	C++, Script	✓	20
	RTXI [24, 159]	RT-Linux	C++, GUI, Script	✓	80
2008	NeuReal [121]	Windows XP	C++, GUI	✓	50
	QuB [167]	Windows XP	GUI, Script	✓	50-80
	SM-2 [2] [206]	Embedded	Script		50
2010	Signal [5]	Embedded	GUI, Script	✓	30-100

[1] Dyna-Quest Technologies (Sudbury, MA)
[2] Cambridge Conductance (Cambridge, UK) [48]
[3] For 2 neurons, ∼5 kHz for 4 neurons
[4] HEKA Elektronik (Lambrecht, Germany) [108]
[5] Cambridge Electronic Design Limited (Cambridge, UK) [62]

expensive specialized hardware. Users usually must accept a trade-off between ease-of-use and flexibility. Furthermore, few users have rigorously tested the capabilities of their system, especially with regard to their real-time performance. There are only a few current dynamic clamp systems that address the technical issues described earlier.

The performance of a real-time platform usually refers to three attributes: system period, jitter, and latency. Latency, the time between receiving an input and updating the corresponding physical output channel, roughly determines the lower bound on the nominal system period, or time step. Latency exists because it takes a finite amount of time to perform analog to digital conversion, do some computation, and convert back from digital to analog. In practice, the actual system period that is observed is a random variable with a mean centered about the target period. This variation is called jitter, and is a direct result of the non-deterministic nature of modern computer architectures. Operating systems that can absolutely guarantee a maximum time for these operations are referred to as hard real-time while operating systems that can only guarantee a maximum most of the time are soft real-time. Hard real-time platforms are used in environments when a missed timing, or overrun, can cause critical failure of the entire system. A soft real-time platform can handle such lateness, usually by pausing processes with a lower priority.

Typically, real-time solutions based on general purpose operating systems such as Windows and Linux will always suffer from high levels of jitter because the underlying system is designed to distribute clock cycles and hardware resources fairly among many competing processes in a multitasking environment. Task rates up to 100 kHz are well within the capabilities of modern computer hardware, but true hard real-time performance is possible only if the computer is running an appropriate real-time control system. Commercial platforms are costly and often tailored for industrial applications such as chemical and manufacturing process control, medical monitoring equipment, and critical guidance and communication systems for automotive and aviation applications. While these platforms offer users commercial technical support and a great deal of flexibility in their software design, they require low-level programming expertise and typically do not provide the standard features of a typical desktop computing environment. However, with the development

of the Real-Time eXperiment Interface (RTXI), the installation and use of these systems is rapidly becoming easier.

RTXI is an open source project that merges the features of three previous systems for closed-loop biological experiments: RTLab [53, 54], Real-time Linux Dynamic Clamp (RTLDC) [67], and MRCI [36, 201]. RTXI is based on Linux, which is extended with the Real-time Application Interface (RTAI) [189] to provide a hard real-time platform with the comprehensive Linux desktop environment. Data acquisition is implemented in real-time using the Linux Control and Measurement Device Interface (COMEDI) [110], which provides access to a variety of commercial multifunction data acquisition cards. Experimental protocols and other real-time algorithms are implemented within a modular framework that supports multiple instantiations of modules and allows users to easily reuse existing code and construct complex protocols. User modules are compiled as shared object libraries that dynamically link to RTXI at runtime and support changes in parameter values "on-the-fly" without recompiling. Users can also take advantage of previously written code or other C++ libraries to add functionality to their modules. As such, RTXI can be a generic real-time platform with potential applications beyond dynamic clamp. At the moment, the installation and operation of a hard real-time operating system requires considerable expertise, which deters some users. Chapter 4 presents the development of modules that improve the usability of RTXI, expand its experiment base, and will make it an ideal platform for implementing real-time closed-loop electrophysiology experiments and other online analysis and control algorithms.

2.3 The Kalman Filter for State and Parameter Estimation in Neuron Models

The dynamic clamp utilizes mathematical models that have contributed much to our quantitative understanding of single neuron dynamics. The development of these models face technical challenges that are common to the simulation of most natural phenomena, which are typically very nonlinear and allow limited experimental measurements. Furthermore, measurements that can be made are usually contaminated by noise that can arise from sources within the system or from the equipment. When developing a conductance-based

neuron model as described before, the only experimentally observable quantity is the membrane voltage but there are multiple underlying states and parameters that also have to be determined.

The general problem of parameter estimation and system identification in computational neuroscience has been limited to parameter space explorations guided by numerical optimization approaches, evolutionary algorithms [1, 85], brute force systematic searches [25, 198], and expectation maximization techniques [124, 125]. These algorithms usually seek to minimize a cost or distance function that corresponds to the error (usually computed in a least squares sense) between the model's behavior and the real neuron's behavior. The terms of the cost function may include features such as spike shape, spike rate, and even the rate of change of V_m at certain points along the system's trajectory [68, 109]. A major challenge in these popular iterative approaches to model construction is that the cost function may become so complex that standard numerical optimization methods fail [69, 249]. These methods can also be highly dependent on the initial estimate and can converge onto local minima without exploring a broad range of parameters.

All these methods also apply a global minimization constraint on the parameter estimation process in order to capture the time-varying dynamics of the system. An alternative approach that guarantees continuity in time is a recursive technique that uses the model's current state to extrapolate its state at the next time step. When state variables can be directly observed or measured from the system, this information can also be used to adjust the prediction to produce a new, more accurate estimate. Algorithms that use these two steps are known as predictor-corrector methods and include estimators for hidden Markov models, sequential Monte Carlo methods, and the Kalman filter. These algorithms have been used extensively in other fields for system identification and process modeling. It has previously been demonstrated that these methods can also be used to fit neuron models to experimental data [124, 125, 183].

Since these are recursive techniques that generate predictions of the system's behavior, they are also candidates for generating control signals to change that behavior. These

model-based techniques can simultaneously provide information about the system that cannot be directly measured as well as guidelines for online feedback during an experiment. Model reference control is commonly used in industry for applications such as supply chain management, automotive control, and flight control in aviation. Model-based approaches are not common in biological applications for several reasons. Until recently, we lacked sufficiently accurate computational models of the biological system. The models that do exist have extremely nonlinear dynamics and most control engineering approaches depend on the ability to linearize a system. Some of these methods are too computationally inefficient for real-time observation and control. Finally, implementing these approaches has been difficult due to a lack of experiment platforms and actuators that can accommodate acquistion and control of biological signals in real-time with the required spatial and temporal resolutions in multiple modalities [151]. In cellular electrophysiology, the dynamic clamp is a first step towards introducing the principle of model-based control to biological applications. With advances in our understanding of neurons and the development of more sophisticated experiment platforms, the time is right to explore more advanced algorithms.

The Kalman filter is focused on here as a computationally simple recursive algorithm for deterministic nonlinear dynamical systems, such as those used in conductance-based neuron models. The Kalman filter is a natural extension of the state space descriptions of single neurons that are common in computational neuroscience and form the basis for implementing dynamic clamp. It has been demonstrated that this technique can successfully reconstruct the states and parameters of a neuron model and has been suggested as a possible way to implement dynamic clamp [218, 243, 253].

The Kalman filter [33] has its roots in statistical signal processing and modeling in which the desired signal is modeled as the output of a filter whose input signal is the data to be processed. In simple environments, a classical filter (such as a lowpass, bandpass, or highpass filter) may be sufficient to restore the desired signal from the measured data. Such filters will rarely be optimum in the sense that they produce the best estimate of the signal from the data. For a known signal, the optimum Wiener filter is designed to process a given signal, $x(n)$, which is assumed to be the desired signal, $d(n)$, with some added noise, $v(n)$,

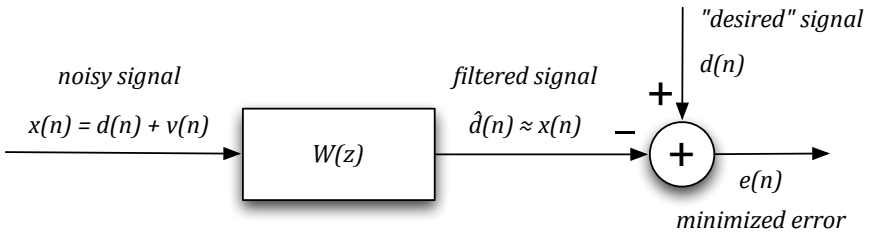

Figure 2: The Wiener filtering approach to a noise reduction problem uses a filter $W(z)$ to produce the minimum mean-square error estimate, $\hat{d}(n)$ of the desired signal, $d(n)$. $d(n)$ is statistically related to the actual given signal, $x(n)$, to be processed.

such that $x(n) = d(n) + v(n)$ as shown in Fig. 2. For a known input and output of the filter, $x(n)$ and $d(n)$ can be translated to the frequency domain and the coefficients of the filter can be determined after computing the transfer function of the filter $W(e^{jw})$:

$$W(e^{j\omega}) = \frac{D(e^{j\omega})}{X(e^{j\omega})} \tag{5}$$

The desired signal, $d(n)$, is not known in advance so that it is not possible to simply compute a transfer function for the filter. For a FIR Wiener filter with an unknown output signal, $d(n)$, the coefficients of the filter are determined by

$$\mathbf{R}_x \mathbf{w} = \mathbf{r}_{dx} \tag{6}$$

where $\mathbf{R}_x$ is a matrix of the autocorrelations of $x(n)$, $\mathbf{w}$ is the vector of filter coefficients, and $\mathbf{r}_{dx}$ is the cross-correlation between $d(n)$ and $x(n)$. $\mathbf{r}_{dx}$ is determined using the statistical properties of the two signals. The result is a filter that statistically minimizes the mean square error between the output of the filter and the desired signal:

$$\xi = E\big(|d(n) - \hat{d}(n)|^2\big) \tag{7}$$

This technique relies on the assumptions that: 1) the signals are stationary, 2) that the noise is a zero-mean random process and uncorrelated with the signal, and (3) the values of the state variables are normally distributed. These assumptions are often not satisfied by real signals and the computational load required for computing the correlations make this algorithm impractical for real-time signal processing applications.

The Kalman filter is closely related to the Wiener filter but is a recursive technique for finding the optimal estimate of the signal and is not restricted to stationary processes. Fig.

3 gives a block diagram for a linear model system represented in state space form. The Kalman filter internalizes a model of how the system behaves and how observable states of the system are related to the model states. $x(n)$ is a vector containing the state variables of the system and $y(n)$ is a vector containing observable quantities, or measurements made from the system. The vectors do not necessarily have the same dimension. The evolution of the state variables depends on the previous system state and is described by a transition matrix, $A(n)$, for a linear system. The measurements do not necessarily correspond directly to state variables defined by the system equations, but may be related to a transformation or combination of state variables, represented by $C(n)$. Both the evolution of the state variables and measurements in time are also subject to noise:

$$x(n) = A(n)x(n-1) + w(n) \tag{8}$$

$$y(n) = C(n)x(n) + v(n) \tag{9}$$

where $w(n)$ and $v(n)$ are uncorrelated Gaussian white noise processes. For parameter estimation, the state vector is augmented to include the parameters, which are treated as state variables that vary slowly in time due to intrinsic noise in the system.

On each time step, the filter estimates new model state values, the *a priori* estimate, and the expected observable values. The state estimates are corrected according to the scaled error between the expected observable values and actual measurements from the system to form the *a posteriori*. Since each measurement gives additional information about the system, this process is known as the *innovations* and the scaling factor is known as the Kalman gain, $K(n)$. The Kalman gain is used to compute a weighted average of the predicted value and the correction based on measured data for each state variable. Initially, the greater weight, and the greater confidence, is given to measured values since the model embedded within the filter is not yet optimized. Over time, however, the Kalman gain minimizes as the state predictions generated by the model are given more confidence.

The state values of the system are assumed to be normally distributed as Gaussian random variables and are completely described by their mean and covariance matrix, which captures the error in the state estimates. These statistics are updated on each time step and

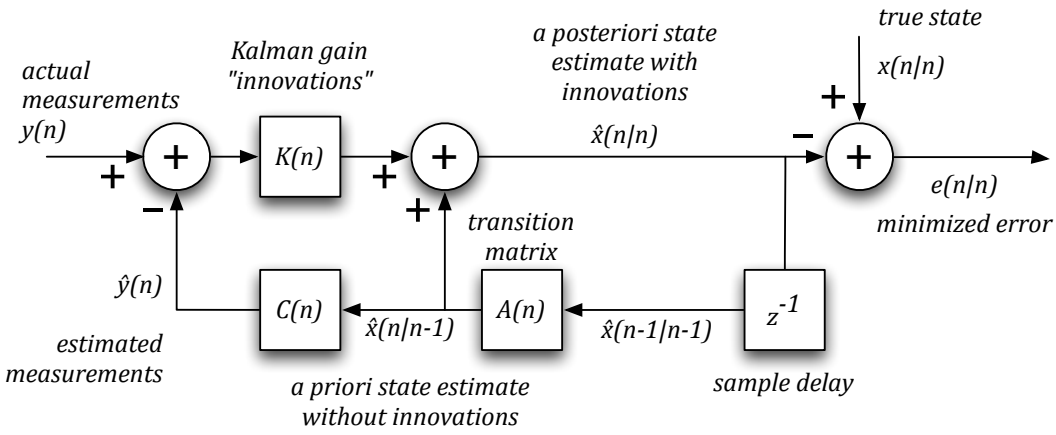

Figure 3: The Kalman filter is a recursive technique for producing the optimal state estimates that describe a system. This block diagram describes a linear state space model where $\hat{x}(n|n)$ is a vector containing the system states at time n given system measurements known up to time n. On each cycle, a new estimate of the system states, $\hat{x}(n|n-1)$, is formed by using the state transition matrix, $A(n)$. The expected system measurements, $\hat{y}(n)$ is formed by further applying a transformation matrix $C(n)$ that relates measureable quantities to system states. The expected measurements and the actual measurements, $y(n)$, are compared and the error between them is scaled by the Kalman gain, $K(n)$. This measurement and scaling is known as the innovations process and provides a correction factor to to give the next state estimate that includes all known information.

since the Kalman gain is chosen to minimize this error, it is also time-varying. Complete equations for the Kalman filter for a linear state model are given in Appendix B.1, Table 8. This formulation allows the Kalman gain to be turned "on" and "off" to optionally ignore system measurements, unlike classical filters which are essentially always on. Furthermore, changes in the structure of the internal model or the statistics of the noise processes can be imposed at any time. For example, if a sensor fails and gives unreliable data, it should be weighted less relative to the model prediction and measurements from other sensors when computing a new state estimate.

The discrete Kalman filter gives the optimal recursive estimate of the system states in a least-squares sense for a linear system, which biological systems are not. For weakly nonlinear systems, the *extended Kalman filter* (EKF) approximates the system with locally linear functions using low-order Taylor expansions [131]. This linearization can produce unstable filters if the local linearity is violated. Furthermore, for many systems, the determination of the Jacobian matrices are nontrivial and would be difficult to implement. The *unscented Kalman filter* (UKF) preserves the exact nonlinearity of the model system by approximating

the probability density of the possible state values [134,136]. This approach is motivated by the fact that is easier to approximate this distribution as a Gaussian than to approximate an arbitrary nonlinear function by linearization. The UKF uses a procedure known as the *unscented transform* that takes each state estimation and generates a weighted set of points that, as a population, capture the mean and variance of the distribution of state values. Each sigma point is propagated through the complete nonlinear system equations and the innovations step to produce a set of updated state estimates. This set is then condensed back into a single new state estimate with an updated mean and covariance [134–136]. The UKF preserves statistics up to second order in a Taylor series expansion but can give good results for even higher order nonlinearities if the time steps are small enough that the temporal dynamics of the systems are only weakly nonlinear [253]. Finally, there is no need to compute the partial derivatives; the nonlinear system equations are used directly.

It has been demonstrated that the UKF can successfully reconstruct the states and parameters of a neuron model and it has been suggested as a possible way to implement dynamic clamp [218, 243, 253]. However, its performance has not been rigorously evaluated in light of common challenges in computational neuroscience and neural electrophysiology. Previous research has only used the Kalman filter to reconstruct the states and parameters of a known model. Furthermore, the parameter estimation was limited only to the maximal conductance or conductance density of ion channels in conductance-based models. In order to actually implement the Kalman filter for real neurons, it is also necessary to determine the appropriate sampling rate, the appropriate initial conditions for the state variables, and how to initialize the error covariance matrices for the state estimates. The goal of the Kalman filter is to adjust the state variables and free parameters to match any observable quantities of the system. A filter that can closely track an observable quantity is not necessarily accurately tracking the hidden states and may not converge onto the "correct" parameter values. It is also possible for the filter to not converge at all and the error in the estimates to increase without bound.

Chapter 5 describes simulations that demonstrate the quality of estimation that can be expected from simple Kalman filter approaches to this problem and approaches for tuning

the filters for better performance. The objective is to develop specific recommendations for real-time implementation in terms of familiar experimental or simulation parameters. In addition to exploring its prospects as real-time model-fitting technique, the research described here also constitutes the first steps towards a method for estimating more complex time-varying quantities encountered in electrophysiology experiments. In particular, given a conductance-based membrane equation written in terms of intrinsic ion channels and synaptic input:

$$C_m \frac{dV_m}{dt} = -\sum \left\{ g_i(t)(V_m - E_i) \right\} + g_{ex}(t)(V_m - E_{ex}) + g_{in}(t)(V_m - E_{in}) \qquad (10)$$

the UKF could be used to estimate changes in $g_{ex}(t)$ and $g_{in}(t)$, the time-varying excitatory and inhibitory synaptic conductance inputs.

Methods for measuring these quantities have been the focus of numerous studies in the context of cortical sensory processing [64, 88, 89, 94, 95, 99, 188, 210, 263, 270]. Accurate estimates of these conductances can provide insights about the wiring architecture of the cortex, such as the significance of recurrent excitation and inhibition, and the existence and functional effect of shunting inhibition. Shunting inhibition has been shown to cause nonlinear effects by causing large increases in membrane conductance and can go undetected since it has a reversal potential that is close to that of the cell [29, 79, 171, 196]. Traditional methods for experimentally measuring conductance include using current pulse injections to periodically construct I-V plots throughout an experiment [9, 99, 172, 259], voltage-clamping the cell at multiple holding potentials to determine the average time course of synaptic inputs for a repeated stimulus [17, 104], and classical filtering techniques to estimate the combined synaptic reversal potential from the subthreshold membrane potential averaged over many trials [95, 188]. In the first two cases, dynamic changes in conductance are not observable. In the third case, estimates are very inaccurate when the neuron is spiking because the intrinsic membrane processes dominate over the synaptic input. More recently, a method has been developed based on particle filtering, a sequential Monte Carlo method, to infer the time course of synaptic input in the presence of rapidly-varying stimuli on a single trial basis [182]. This method was demonstrated in simulations and it too computationally

expensive to implement in real-time. There are currently no techniques for estimating conductance that can be implemented in real-time during an experiment. Such a technique could be used to dynamically track the balance between excitation and inhibition and the balance between intrinsic dynamics and synaptic input while delivering behaviorally relevant stimuli.

CHAPTER III

COMBINING DYNAMIC CLAMP AND MODELING TO INVESTIGATE DISTRIBUTED SYNAPTIC INTEGRATION

Dynamic clamping is an increasingly widely used technique, which allows the application of artificial conductances [207, 220] to a neuron using whole cell methods. However, a major limitation of dynamic clamp is that the artificial conductances are focally applied only at the site of the electrode, usually the soma, and may not realistically represent the effects of distributed dendritic synapses [197]. Due to passive cable properties, synaptic potentials from distal dendritic sites are delayed and attenuated before reaching the soma [202]. On the other hand, local dendritic voltage-gated currents can interact with synaptic potentials to amplify synaptic input or even initiate action potentials [133, 164]. Because many of these processes are nonlinear and depend on analytically non-solvable systems of equations, computer simulations provide the only tool to systematically investigate the role of dendritic morphology and voltage-gated conductances in affecting synaptic responses. These factors play an important role in the difference in responses for dynamic clamp stimuli applied at the soma and naturally distributed synaptic input.

In previous studies, the dynamic clamp was used to study how temporal modulation of inhibitory and excitatory inputs control the frequency and precise timing of spikes in neurons of the deep cerebellar nuclei. More recently, a morphologically realistic compartmental model has been developed with appropriate voltage-gated conductances to replicate current clamp data recorded in vitro [233]. This makes it an excellent model system for developing techniques for comparing the effects of focalized and distributed synaptic inputs, and challenging the assumptions of dynamic clamp by using a combined experimental and computational approach. The model can also be used to address how intrinsic membrane conductances interact with synaptic input to shape DCN activity.

In the present study, we develop a computer simulation approach and a set of benchmarks to assess differences in responses between distributed synaptic input and the same input applied focally at the soma. The same background synaptic input used in the previous experimental studies to the model neuron and determined how the output spike pattern, spike-timing precision, and spike rate differed for focalized and distributed input. In the case of our relatively electrotonically compact DCN neuron, distributing the same synaptic input patterns over the dendritic tree resulted in only minor differences in the resulting spike patterns. This simulation approach and benchmark tests are applicable to any neural morphology, however, and a higher degree of deviation between focal and distributed input conditions is expected in larger cell types with prominent local dendritic processing.

3.1 Dynamic Clamp Experiments

The methods for performing dynamic clamp in DCN neurons have previously been described by Gauck et al. (2000, 2003). Briefly, 300 μm sagittal cerebellar slices were obtained from 14- to 17-day old Sprague-Dawley rats and placed in a medium containing (in mM) 124 NaCl, 3 KCl, 1.2 KH_2PO_4, 26 $NaHCO_3$, 2 $CaCl_2$, 1.9 $MgSO_4$, and 20 glucose. The electrodes were filled with a solution of (in mM) 140 K-gluconate, 10 HEPES, 10 Nal, 0.2 EGTA, 4 MgATP, 0.4 NaGTP, 0.05 spermine, 5 glutathione, and 1

The synaptic kinetics used to construct the dynamic clamp stimuli were based on in vitro recordings [8]. Inhibitory GABAA-type Purkinje cell input was modeled as 400 presynaptic input elements and implemented as GENESIS synchan objects. The GENESIS timetable object was used to generate random distributions of synaptic events that activated the synapses at a mean rate of 35 Hz. The inhibitory synapses were modeled as dual-exponential functions with a rise time constant of 0.93 ms and a decay time constant of 13.6 ms. The sum of the inhibitory postsynaptic conductances from all 400 inhibitory synapses was used as the inhibitory conductance waveform (G_{in}) (Fig. 4, left). To isolate the effect of inhibition on spiking, the excitatory conductance (G_{ex}) was held at a constant level such that the ratio of total excitatory to mean inhibitory conductance was 3:4. We varied the level of synaptic strength by multiplying both the inhibitory and excitatory conductances by a gain factor.

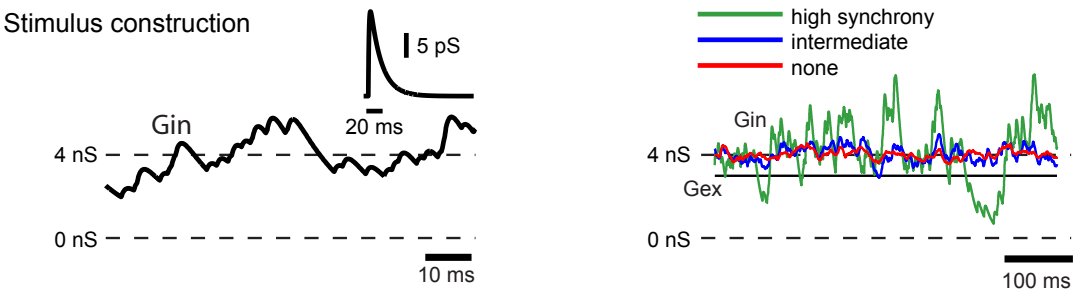

Figure 4: Construction of dynamic clamp conductance waveforms. The dynamic clamp inhibitory conductance waveform (G_{in}) is the sum of 400 inhibitory input conductances over time. The timing of inputs is stochastic and composed of single inhibitory post-synaptic conductances with a double-exponential time course. Inhibitory conductance waveforms for higher levels of synchronicity have larger transient fluctuations around the mean. Excitatory conductance (G_{ex}) is constant at a level of 3/4 that of mean inhibitory conductance.

The default amount of conductance used (gain 1) corresponded to a total mean inhibitory conductance of 2 nS and a unitary conductance of 8.6 pS, and this level was increased up to 16-fold (gain 16). Three different levels of input synchronization were also implemented (Fig. 4, right). At the highest level of synchronization, the 400 inhibitory synapses were divided into 10 groups of 40 synchronized synapses. To simulate an intermediate level of synchronization, the 400 inhibitory synapses were divided into 100 groups of 4 synchronized synapses.

The maximal conductance of a single inhibitory synapse and the level of tonic excitatory conductance were originally chosen by Gauck et al. (2000) to yield in vivo spike frequencies in dynamic clamp. The average combined synaptic reversal potential (E_{syn}) was -40 mV. E_{syn} is the weighted average of the inhibitory (E_{in}) and excitatory (E_{ex}) reversal potentials:

$$E_{syn} = \frac{E_{ex} * G_{ex} + E_{in} * G_{in}}{G_{ex} + G_{in}} \tag{11}$$

For dynamic clamp, the injected current can be formulated as

$$I_{inj} = (G_{ex} + G_{in}) * (E_{syn} - V_m) \tag{12}$$

such that I_{inj} is zero when the membrane potential equals E_{syn}. Higher levels of input synchronization correspond to larger transient fluctuations of E_{syn} around its mean. The reversal potentials for excitation and inhibition were 0 mV and -70 mV, respectively.

For simulations using synaptic excitation rather than tonic excitation, a population of 100 excitatory mossy fiber synapses was modeled with three components: an AMPA component, a fast NDMA component, and a slow NMDA component. The rise and decay time constants were 0.5 and 7 ms for AMPA, 5 and 20.2 ms for fast NMDA, and 5 and 136.4 ms for slow NMDA. The fast unitary NMDA conductance had a peak value of 57% of the AMPA peak, and the slow unitary NMDA conductance had a peak value of 28% of the AMPA peak. The unitary peak conductance amplitude of the AMPA conductance was set to 58.5 pS so that the sum of all excitatory conductances still had a mean of 1.5 nS at a gain of 1 to maintain the 3:4 ratio of mean excitatory to inhibitory conductance. These synapses were activated at a mean rate of 20 Hz.

3.2 DCN Model Construction

Our DCN model was developed in a previous study to closely match the membrane potential trajectory found during spontaneous pacemaking in brain slices as well as responses to positive and negative current injections [233]. We use the identical model here with the exception of added current noise to the soma as described below. Similarly, any compartmental model developed in the literature can be used to employ the same methods to compare different conductance locations for synaptic input (or in fact the location dependence of voltage-gated currents). We suggest that such modeling provides an important companion to all dynamic clamp studies.

3.2.1 Morphology, passive properties, and active conductances

The DCN model morphology was derived from a Neurolucida reconstruction of a biocytin labeled deep cerebellar neuron (Fig. 5A). In a previous study, a genetic algorithm was used to find passive model parameters that fit the neuron's voltage responses to positive and negative current injection in the presence of ion channel and synaptic blockers [232]. The resulting passive parameters were a uniform specific membrane resistance, R_M, of 3.56 Ωm^2, axial resistance, R_A, of 2.35 Ωm, and membrane capacitance, C_M, of 0.0156 F/m^2. These parameters yield a total membrane resistance of 271 $M\Omega$ (inverse of summed membrane conductance for the soma and 485 dendritic compartments). The model neuron

is relatively electrotonically compact with an average dendritic electrotonic distance from the soma of 0.2 λ and a maximum electrotonic distance of 0.53 λ from the soma to the most distal dendritic tip (Fig. 5B). A spike initiation zone was implemented by attaching a 30 compartment artificial axon, containing an axon hillock and initial segments with increased sodium channel density following a published method [223]. Simulations were run using a fixed time step of 0.01 ms.

The model features a full complement of membrane channels based on conductances known to be present in DCN neurons [3,129,160,203] and implemented using the Hodgkin-Huxley formalism in GENESIS [18]. They include a fast sodium current (NaF) that contains both a fast and slow inactivation component as shown by experiments in the DCN [7,203], a mixture of fast Kv3 family (fKdr) and slow Kv2 (sKdr) family delayed rectifiers based on a family of TEA-sensitive Kdr channels [12,13], a tonic non-specific cation current (TNC) to provide persistent inward current for tonic spiking [203], a high-voltage activated (HVA) calcium current [84,169,170], and a low-voltage activated T-type calcium current (CaT) that is implicated in fast rebound responses [3,160,169,170]. While several T-type channel isoforms are expressed in DCN neurons, only the CaV3.1 subtype is associated with strong rebound activity in DCN neurons [169] and is included in our model. We adapt the kinetics of a extensive CaT channel model previously developed for thalamocortical neurons [63]. Calcium influx through the HVA calcium conductance is coupled to an intracellular calcium pool that is modeled as a diffusion shell with an exponential decay time constant of 70 ms. This long time constant results in accumulation of intracellular calcium as observed experimentally during fast spiking in DCN neurons [174,269].

The final membrane conductances in the model are a calcium-gated voltage-independent potassium current (SK) that underlies the medium afterhyperpolarization [3,74,128,203], a hyperpolarization activated (IH) current [3,128,203,245], and a slowly inactivating persistent sodium current (NaP) [129,160]. The density of active conductances in the model was variable between four major divisions of the model: axonal, somatic, proximal dendritic, and distal dendritic (Table 7). In particular, there were no NaF or Kdr conductances in the distal dendrites of the model since there is no experimental evidence showing a dendritic

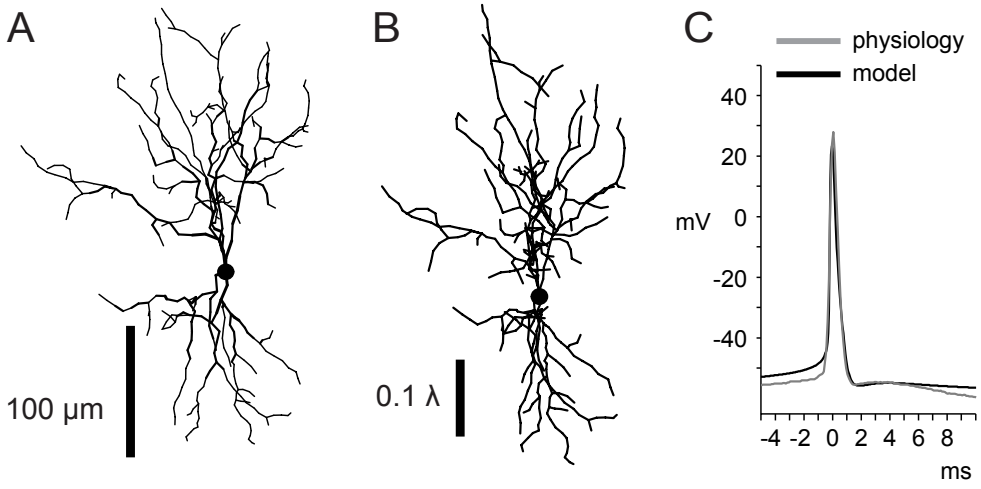

Figure 5: Match of DCN model neuron to physiological properties. A) Morphological reconstruction of the DCN neuron used in model simulations. B) The same morphological reconstruction of the DCN neuron in (A), redrawn to electronic scale. C) There is a good match in spike shape and afterhyperpolarization properties between a physiological slice recording and a sample simulation.

location for these channels in the DCN. The SK conductance was also primarily somatic to match the strong somatic mAHP seen in recordings. Both the CaT and HCN conductances were distributed in a gradient with a higher density in the dendrites following experimental findings [84, 203]. All channel kinetics were adjusted to a temperature of 32°C as used for the slice recordings by applying a Q10 value of 3.0 for all Hodgkin-Huxley rate constants. The density of each channel type in the model was manually adjusted until a good match of current clamp responses with model traces was achieved. The spike shape and AHP trajectory of recordings were used as targets as well as spontaneous spike rate and f/I curves. Detailed equations for the channel kinetics and values used for the channel conductance densities are given in Appendix A.

3.2.2 Simulation of Synaptic Input

The simulations used the same synaptic conductance waveforms as were used in the original experiments. While some synaptic kinetic parameters for AMPA and GABA-A synapses onto DCN neurons have since been updated in the literature [199, 200, 237], using the original model synapses allows us to exactly reproduce the experimental dynamic clamp input conductance waveforms. The reversal potentials of the excitatory and inhibitory

synaptic conductances were initially set to 0 mV and -70 mV, respectively. Since the original dynamic clamp recordings were not corrected for a junction potential of 10 mV, as calculated with JPcalc [14], the reversal potentials of the synapses in the model were shifted downward by 10 mV. They were then further shifted by the difference in the mean value of the subthreshold membrane potential between the slice recordings (-49.4 $\pm$ 3.0 mV) and the model (-53.8 $\pm$ 1.83 mV). These values were calculated after removing a window of 3 ms before and after the peak of each action potential. The final reversal potentials of the excitatory and inhibitory synapses in the simulations were set at $\pm$14.4 mV and -84.4 mV, respectively. The result of these manipulations was that the amplitude of total synaptic current generated in the model was comparable to the current injected by dynamic clamp in the experiments by Gauck et al. (2000) for a given input condition.

DCN neurons in vivo are likely subject to strongly patterned synaptic input due to bursts and pauses in Purkinje cell and mossy fiber activity in vivo. Prolonged increases or decreases in the simple spike firing rate of Purkinje cells have been observed in response to both sensory stimulation [163] and motor behavior [166]. Numerous studies have demonstrated correlations in simple and complex spike activity [145, 266, 267] that can be modulated by behavior [106, 107, 225] as well as correlated pauses in Purkinje cell firing that can mediate DCN activity [56,224]. This correlated activity produces sharp fluctuations in input to DCN neurons that can then be encoded with high reliability. Mossy fiber input to the DCN is less well understood but their firing rate is known to be strongly modulated by movement with complex biphasic or triphasic activity patterns and high frequency bursts that can last up to several hundreds of milliseconds [204, 247]. To determine how strongly patterned synaptic input can shape the response of DCN neurons and whether the distributed input condition still resembles the focalized one, we added inhibitory and excitatory burst and pause features in addition to the background synaptic input in the model. The total amount of injected current that would be needed to implement these conductance inputs in a dynamic clamp experiment would not have been possible using the original experimental equipment due to large artifacts in the recordings and potential damage to the electrode.

3.2.3 Focalized vs. distributed synaptic input

To simulate dynamic clamp in the model, all synapses were focalized completely on the soma, which is the site of current injection with a somatic whole cell recording. The total synaptic current generated in the model is analogous to the current injected by the dynamic clamp. For the distributed input condition, the same number of inhibitory synapses was randomly distributed with 12% (48) on the soma, 37% (148) on the proximal dendrites, and 51% (204) on the distal dendrites to approximate experimentally observed input distributions [181]. Since nearly all somatic synapses are inhibitory for DCN neurons, no excitation was placed on the soma for either the tonic or synaptic excitation input conditions [41,58,181]. For the tonic input condition, a flat excitatory conductance was added to each proximal or distal dendritic compartment that contains an inhibitory synapse and scaled so that the total amount of excitatory conductance was the same for both the focalized and distributed input conditions. For synaptic excitation, the 100 excitatory synapses were placed on randomly chosen proximal and distal dendritic compartments. The total amount of inhibitory and excitatory synaptic conductance as well as the temporal input patterns was the same for both focalized and distributed input conditions.

3.2.4 Simulation of noise

In the absence of excitatory or inhibitory synaptic inputs, the model was able to reproduce the spontaneous spike waveforms and spike rates observed in DCN neurons in brain slices (Fig. 6). In fact, for each target measure such as spike height and width, spike afterdepolarization, spontaneous spike rate and f/I curve the model's performance was within the variability of the same measures observed in recordings. To simulate biological variability in the model's spontaneous activity as well as repeated trials of the dynamic clamp stimuli, noise was introduced to the model as a fluctuating somatic current injection. The noise is constructed as a white noise stimulus with a mean of 0 pA and a standard deviation of 200 pA. Since the noise has zero mean, the net membrane current remains unchanged over the course of the stimulus and results in very little baseline shift in the subthreshold membrane potential. The model without noise fires spontaneously at 11.20 Hz and at 11.17 $\pm$ 0.15

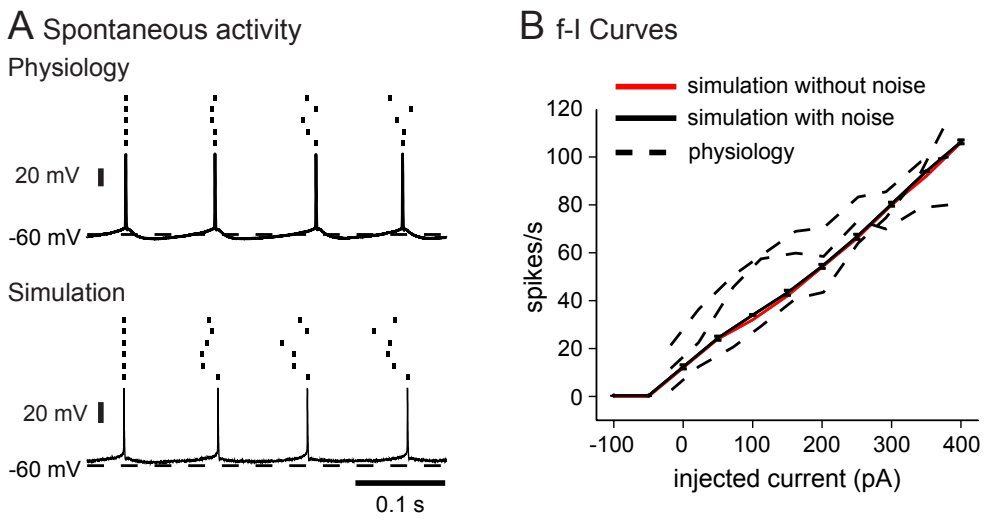

Figure 6: A) The added white current noise produces similar variability in the spontaneous firing activity in the model. B) Spike frequency increases in response to current injection pulses similarly for the model neuron (solid) and three recorded neurons (dashed). Note that the addition of noise had virtually no effect on the f-I curve of the model. Error bars represent one standard deviation (n = 6). Error bars for simulations with noise representing one standard deviation are plotted but due to their small size are mostly within the line width of the graph.

Hz (n = 6) with noise. The subthreshold membrane potential of the model was calculated after removing spikes to be -53.8 mV without noise and -53.9 mV with noise (Fig. 6A). The additional somatic noise current also did not significantly affect the model's spike rate increases in response to injected current pulses (Fig. 6B). This compared well to a subthreshold membrane potential in experimental recordings of -49.4 mV (n = 33 neurons) after removing the 10 mV junction potential.

The added noise introduced small irregularities to the spontaneous firing pattern of the model (CV = 0.143), which settled to nearly perfectly regular pacemaker activity in the absence of noise. The irregularity of spontaneous spiking in our experimental recordings was similar to the model with added noise (CV = 0.126, n = 9 neurons). This similarity served as an independent verification of the validity of adding noise in the form of somatic current injection, as our noise amplitude was originally chosen to match the level of subthreshold membrane potential fluctuations found in the experimental recordings (Fig. 7B). This current was always applied somatically in the model for both focalized and distributed synaptic input conditions. Six waveforms of frozen noise were obtained using different

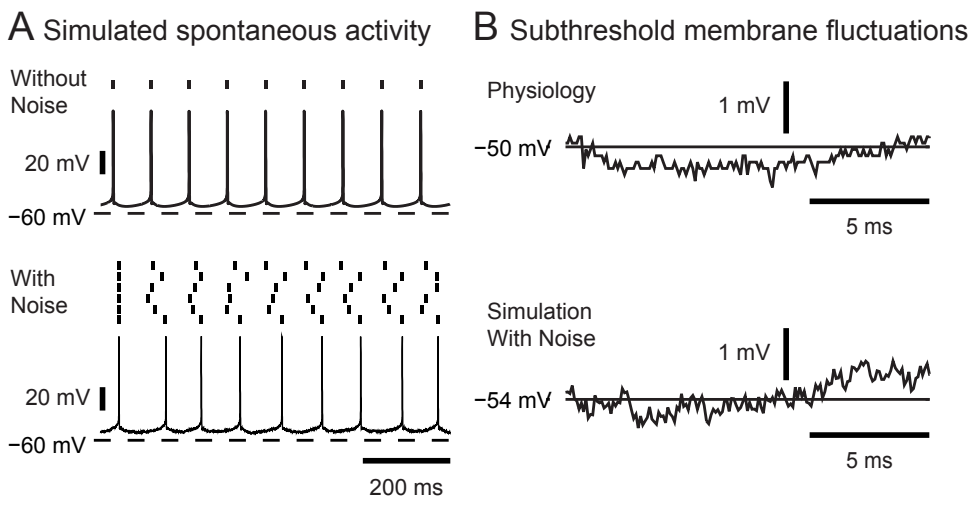

Figure 7: Effect of noise on spontaneous spiking and subthreshold voltage oscillations in the model. A) The model without noise spikes perfectly regularly (top). The effect of the additional white noise current introduces variability in spike timing that simulates variability of spontaneous spiking seen in vitro even in the presence of synaptic blockers (bottom). B) The good match in the amplitude of the subthreshold voltage fluctuations between a recorded neuron (top) validates our noise model.

random seeds to result in 6 repeated runs with identical synaptic input conditions under varying noise conditions as we had previously obtained in our recordings. In test simulations, we also applied current noise to the action potential initiation zone in the axon hillock and initial segment, which has a two-fold increase in sodium channels compared to the soma [233].

The power spectra of the voltage noise at the soma for the electrophysiology recordings and our simulations were very similar (Fig. 8). The power spectral density of the membrane potential was estimated using a multitaper method to reduce bias [268]. A window of 3 ms before and after the peak of each spike was removed prior to the analysis. Because noise affects spike timing predominantly through effects in the spike initiation zone, we examined the subthreshold noise trajectory in our simulated axon hillock and initial segment with a somatic noise source and compared this result with a direct application of the same noise to the axon hillock and the axon initial segment (Fig. 9). The noise fluctuations in V_m were nearly indistinguishable in all cases, which can be explained by the electrotonically close proximity of the axon initial segment to the soma in the model. When noise is applied to the soma of the model during spontaneous activity, there is very little attenuation of the

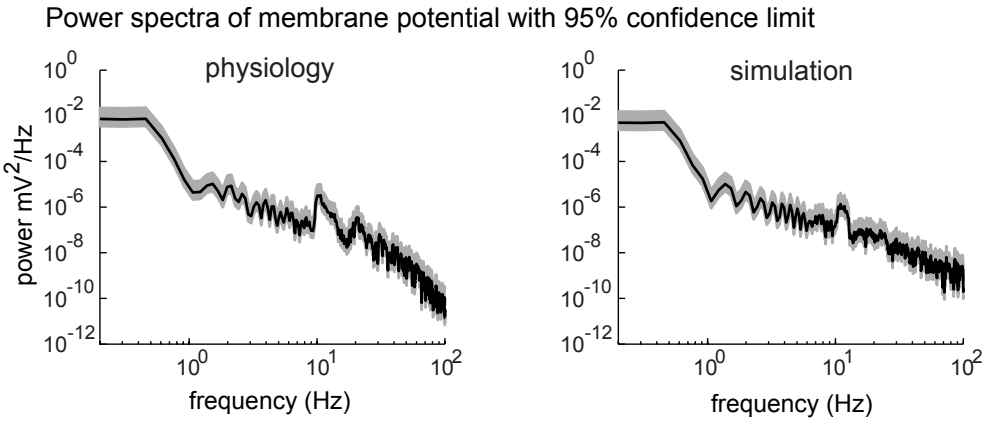

Figure 8: The power spectra of the subthreshold membrane potential show a good match between recordings and simulations with noise. Spikes were removed before analysis using a window of ±3 ms around each spike time. The residual effect of the spike appears as a peak at 10 Hz in both the recordings and the model. The shaded area indicates the 95% confidence level for the power spectral estimate.

spike and subthreshold noise fluctuations from the soma to the axon initial segment (IS). Simulations were also performed in which the the same noise was applied instead to the axon hillock or the axon IS. During spontaneous activity, there is initially no significant difference in spike timing, but small differences in how spikes were generated in the IS eventually accumulated and led to diverging spike times after long simulation times. During simulated dynamic clamp, the output spike pattern remained the same when the noise was applied to different compartments, and differences in spike times were always less than 1 ms.

3.2.5 Data Analysis

Previous dynamic clamp experiments show that DCN neurons spike with millisecond precision that varies with artificial synaptic input parameterized for synchrony, gain, and mean input rate [82,83]. In the experiments (Fig. 10A), the subthreshold membrane potential was increasingly controlled by the trajectory of the synaptic input conductance when the average level of input was increased from 4 to 16 nS. Spike alignment for repeated applications of the same synaptic conductance trajectory was apparent from the raster plots. The same data analysis techniques used to analyze the original dynamic clamp experiment results will

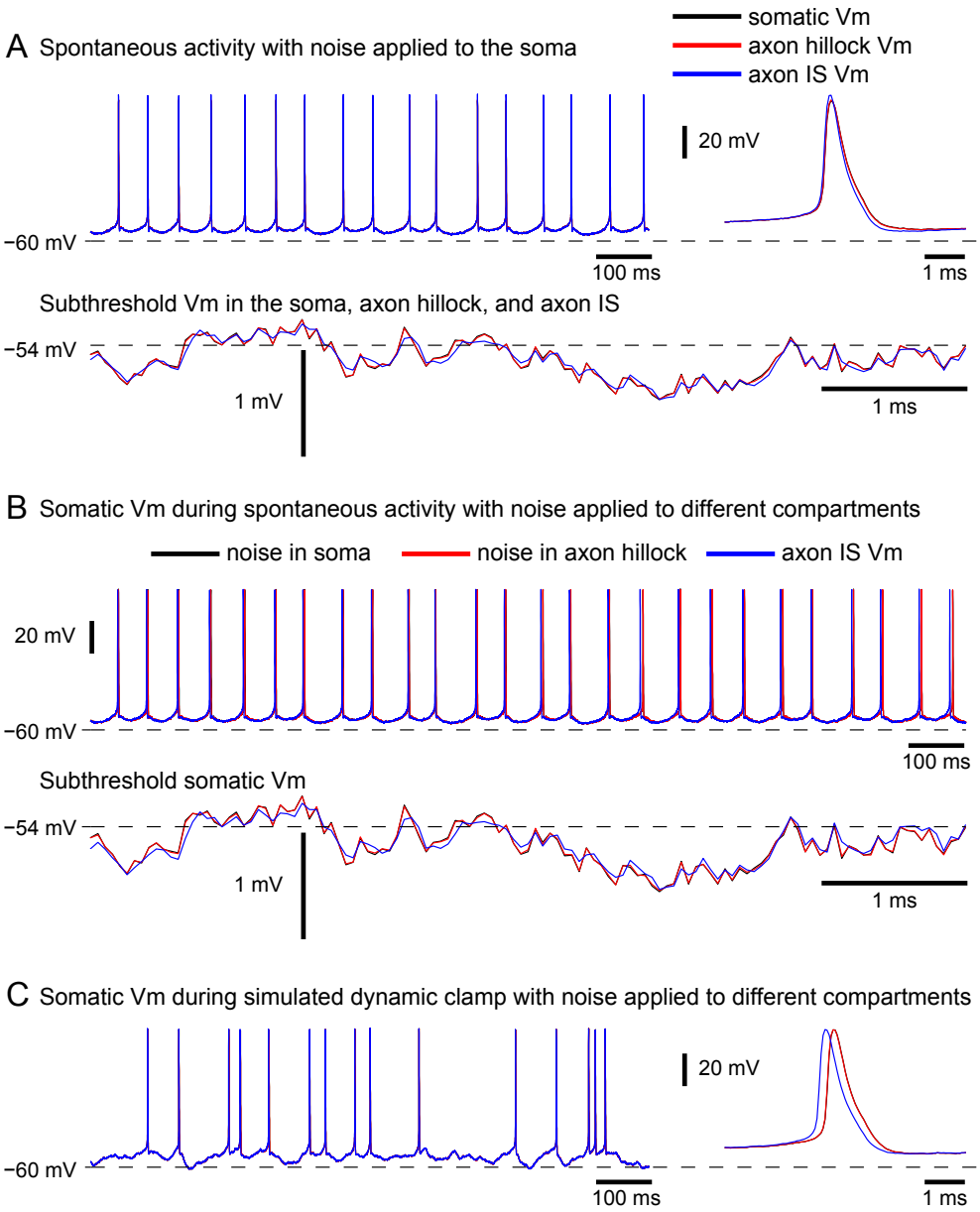

Figure 9: Effect of noise on spontaneous spiking and subthreshold voltage oscillations in the model. A) When noise is applied to the soma of the model during spontaneous activity, there is very little attenuation of the spike and subthreshold noise fluctuations from the soma to the axon initial segment (IS). B) Simulations were also performed in which the the same noise was applied instead to the axon hillock or the axon IS. During spontaneous activity, there is initially no significant difference in spike timing, but small differences in how spikes were generated in the IS eventually accumulated and led to diverging spike times after long simulation times. The subthreshold noise fluctuations in V_m are nearly indistinguishable from those in (A), which can be explained by the electrotonically close proximity of the axon IS to the soma in the model. C) During simulated dynamic clamp, the output spike pattern remained the same when the noise was applied to different compartments, and differences in spike times were always less than 1 ms.

be repeated for the the simulations. The spike alignment is quantified by computing the cross-correlogram with 1 ms bin width from the spike times of pair-wise combinations of trials obtained with repeated stimuli. The raw correlogram will be corrected for its dependency on spike frequency by computing the expected level of correlation from spike trains with shuffled interspike intervals and subtracting it from the raw correlogram. A spike-time precision metric is further defined as the percentage of spikes that occurred within 1 ms or 5 ms in the corrected cross-correlogram. To analyze the input events responsible for spike generation, we also computed the spike-triggered average (STA) of the excitatory and inhibitory input conductances in a window of ± 150 ms around detected spike times. This technique is a reverse correlation method often used in neural electrophysiology to determine the optimal features of a time-varying stimulus that elicit a specific response by providing an estimate of a neuron's linear receptive field [2, 26, 55]. These metrics will allow us to quantify how well the model reproduces the biological neurons' response to dynamic clamp stimuli and analyze the use of this technique in this cell type.

3.3 Results

We found that the model was capable of reproducing responses to complex fluctuating inhibitory and excitatory conductances previously recorded with dynamic clamping without further tuning the model parameters. With additive white current noise applied to the soma, the model could also reproduce the millisecond precision in spike times. In our DCN neuron model, there were only minor differences in spike pattern generation between focalized or distributed input in the model, even when strong inhibitory bursts and pauses or excitatory bursts were applied. The relationships between spike-time precision and spike frequency with different input levels and input synchronicity were also very similar. The lack of differences in responses to focalized or distributed synaptic inputs suggests that deep cerebellar nucleus neurons essentially do not rely on their morphology for input processing. Different cell types and in particular larger types of neurons, will likely show more pronounced local dendritic processing and hence less similar results for focal somatic and

distributed dendritic synaptic input. Our results highlight the ability to study the interaction of intrinsic properties and synaptic input in the control of output spiking with a combined dynamic clamp and modeling approach.

3.3.1 Simulation of dynamic clamp experiments in the model

To isolate the effect of Purkinje cell inhibition on the control of DCN spiking, excitation was held constant while inhibitory inputs were constructed from spike trains of 400 inhibitory presynaptic elements that generated inhibitory postsynaptic conductances in the model. This input pattern exactly matched our previous dynamic clamp input used in published experiments (Gauck et al., 2000; see Methods). In close parallel, both in the experiment (Fig. 10A) and in the model (Fig. 10B), the subthreshold membrane potential was increasingly controlled by the trajectory of the synaptic input conductance when the average level of input was increased from 4 to 16 nS. As we previously described in our dynamic clamp studies [82, 83], the subthreshold membrane potential was forced to follow the combined reversal potential of excitation and inhibition (E_{syn}) because any deviation from this trajectory leads to a sharp increase in synaptic driving force and a resulting corrective current. This effect was quantified by computing the cross-correlation between the subthreshold membrane potential and the combined synaptic reversal potential, E_{syn}. The subthreshold membrane potential was obtained by removing spikes from the recordings of the membrane potential and replacing it with a straight line connecting the endpoints of a $\pm$3ms window around each detected spike time. The magnitude of the central peak in the cross-correlogram increased as the average level of synaptic input was increased showing that the subthreshold membrane potential was increasingly controlled by the trajectory of the synaptic input conductance. Data is shown for simulations in which inhibitory synapses and excitation applied as a constant conductance were localized in the soma only to simulate dynamic clamp (Fig. 11).

At a mean inhibitory input conductance of 4 nS the activation of intrinsic currents of the neuron still results in substantial deviations of the subthreshold membrane potential from E_{syn}, most notably during activation of the post-spike afterhyperpolarizing (AHP) currents.

At an increased mean inhibitory conductance of 16 nS, the shunting effect of inhibition was increased such that both in the dynamic clamp data and in the model the spike AHPs were almost completely suppressed, and the subthreshold membrane potential converged onto E_{syn}. The average spike waveform was computed from recordings of a biological neuron and the model neuron while spiking spontaneously or under dynamic clamp with a mean inhibitory conductance of 4 nS or 16 nS (Fig. 12). At an increased mean inhibitory conductance of 16 nS, the shunting effect of inhibition was increased such that both in the dynamic clamp data and in the model the spike AHPs were almost completely suppressed. There is a difference of 1-2 mV in the AHP for these two levels of inhibitory conductance for both the biological neuron and the model.

Spike alignment for repeated applications of the same synaptic conductance trajectory was apparent from the raster plots (Fig. 10). We quantified this spike alignment using a cross-correlation analysis, which showed an increasingly pronounced central peak for spike alignment between trials when the mean synaptic conductance level was increased (Fig. 10C). For all input conditions, the spike time cross-correlograms were very similar between the model and the experimental data. The percentage of spikes that were aligned within a window of ± 1 ms for the sample neuron shown and the model, respectively, were 12% and 11.5% for a 4 nS mean inhibitory conductance and 42% and 38.7% for 16 nS. Therefore, the model provided a close match to our slice recordings with respect to the conductance amplitude needed to control spiking by somatic conductance application.

Synchronicity of spiking between Purkinje cells might provide an important coding feature in the cerebellum [56,145,224,266,267], and therefore we had used partly synchronized inhibitory input patterns in our dynamic clamp study to determine the consequences of input synchronization. When our 400 inhibitory inputs were divided into 40 or 4 groups of synchronously firing subpopulations, the ensuing fluctuations in total inhibitory conductance were much larger and strong depolarizing shifts in E_{syn} were more frequent (Fig. 4, right). This change in input conductance resulted in a similar increase in spike rate as well as spike precision in the model and the slice recordings (Fig. 13A). Another benchmark, the spike-triggered average (STA) of input conductance, was computed for a duration of ± 150

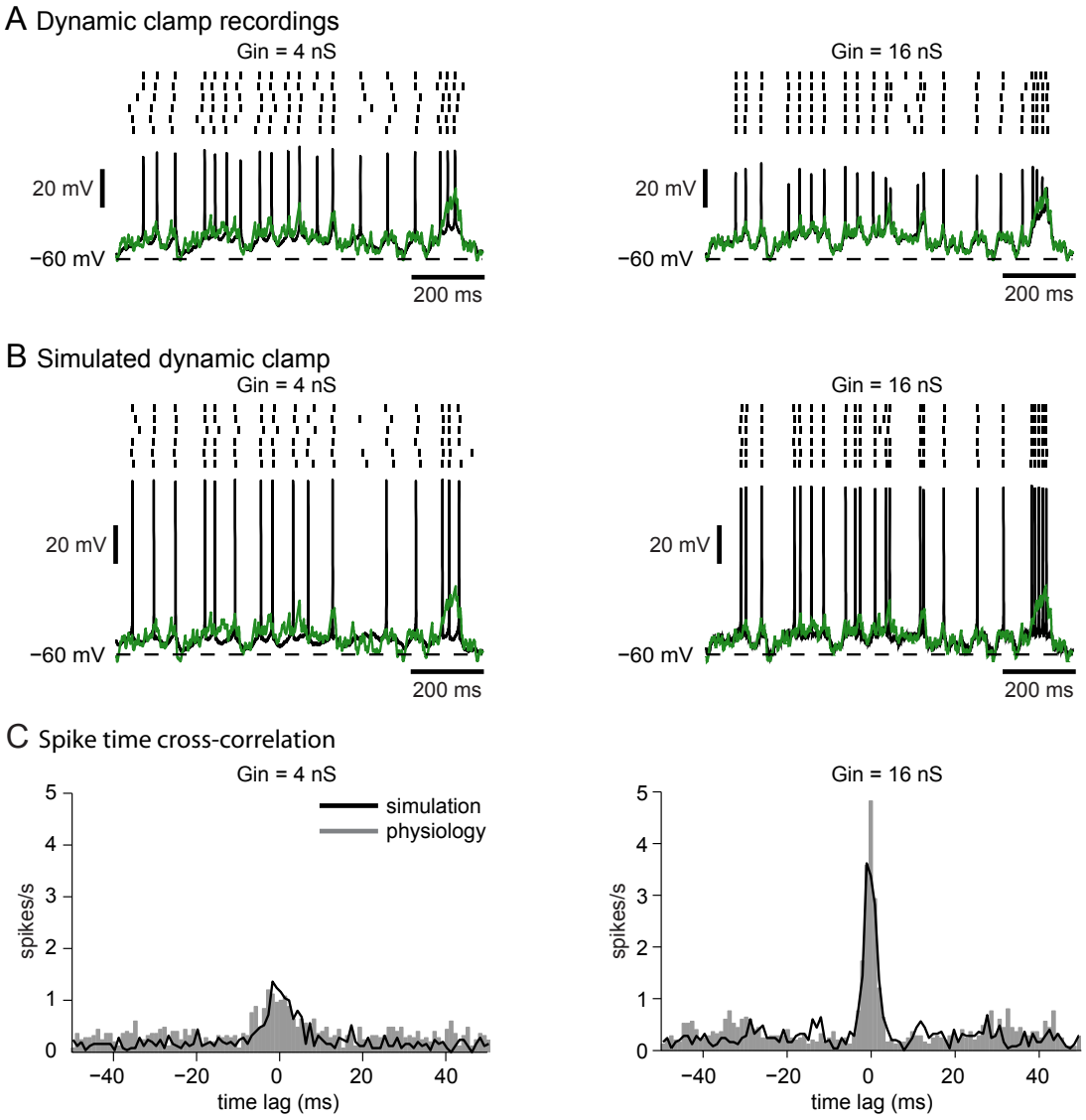

Figure 10: Match of DCN dynamic clamp simulations to slice recordings. A) Sample recordings of dynamic clamp voltage traces are shown for high input synchronization and two levels of inhibition. For a mean inhibitory conductance of 16 nS, the subthreshold membrane potential (black) closely follows the synaptic driving force (green). B) Voltage traces from the computer model with the exact same synaptic inputs applied to the soma, simulating dynamic clamp. C) There is a more prominent central peak in the spike-time cross-correlogram for a G_{in} of 16 nS than 4 nS, indicating greater spike-time precision at higher input gains. The spike time cross-correlograms are very similar between the model (black line) and the experimental data (gray bars).

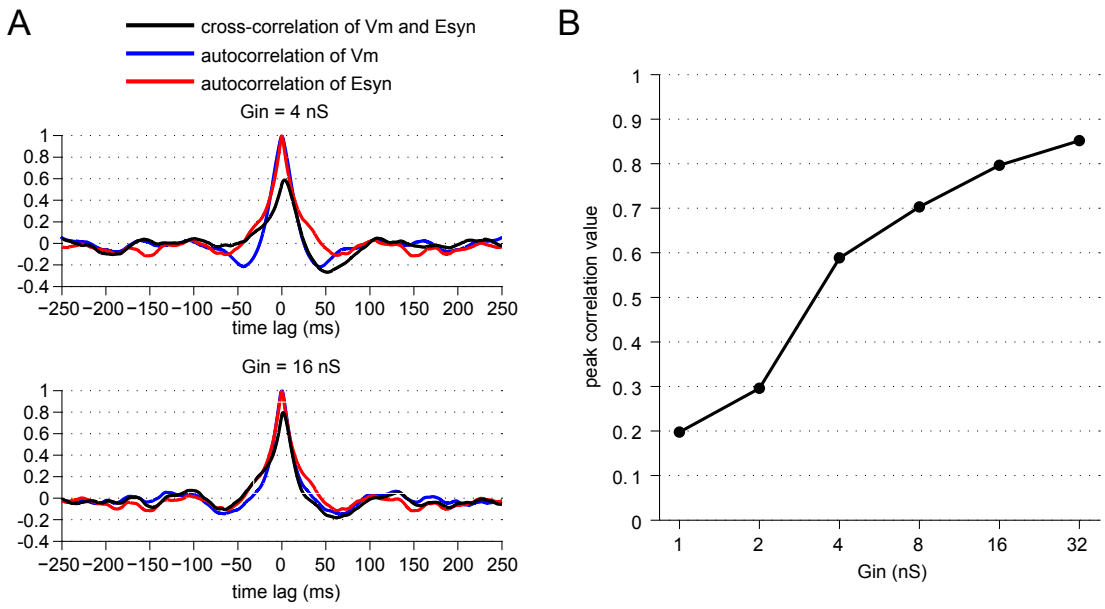

Figure 11: Cross-correlation analysis shows that the subthreshold membrane potential tracks the combined synaptic reversal potential more closely as input gain increases A) The cross-correlation between the subthreshold membrane potential and the combined synaptic reversal potential, E_{syn} (black). The cross-correlation shows a strong positive central peak. The autocorrelations of the subthreshold membrane potential (blue) and E_{syn} (red) explain the strong negative correlation in the major side lobes at ± 50 ms lag. B) The magnitude of the central peak in the cross-correlogram between E_{syn} and the subthreshold membrane potential increases smoothly from a value of 0.20 to 0.85 as the average level of input was increased from 1 to 32 nS.

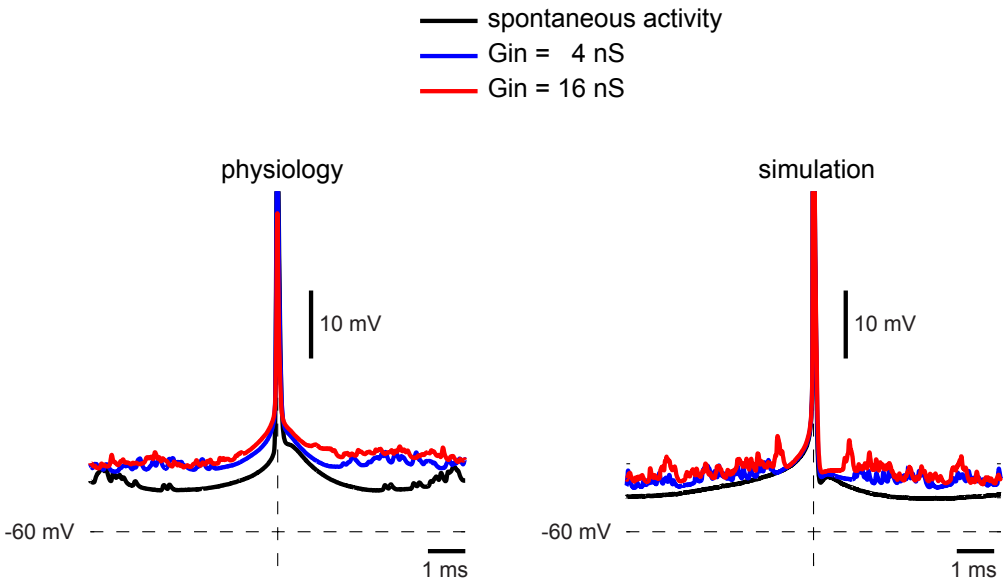

Figure 12: Average spike waveforms from the biological (left) and model (right) neurons spiking spontaneously and under dynamic clamp with a mean inhibitory conductance of 4 nS or 16 nS. At an increased mean inhibitory conductance of 16 nS, the shunting effect of inhibition was increased such that both in the dynamic clamp data and in the model the spike AHPs were almost completely suppressed.

ms around the peak of the action potentials and normalized to a mean value of 1.0. This measure shows that a transient decrease in inhibition caused by brief pauses in Purkinje cell input served as a reliable trigger for spikes. Both the amplitude and the time course of the STA for inhibitory conductance were similar between the recording and the model (Fig. 13A, right).

Both the recordings and the model also showed that at high input gains but low levels of synchronization the spike rate precipitously dropped to near zero, although the mean conductance levels were identical with those at higher levels of synchronization that elicited much faster spike rates. This effect is of high physiological interest as it suggests that DCN spiking may primarily be due to input fluctuations, and that in the presence of completely random Purkinje cell inputs, DCN neurons would not spike due to a high steady-state GABA conductance. In contrast, in the presence of input fluctuations due to synchronous input populations, an increase in input level leads to an increase in output spike rate in recordings, an effect that was also matched by the model (Fig. 13A). One should note that

the balance of excitatory and inhibitory conductance and the trajectory of the combined reversal potential are identical at all input levels. Therefore, an increase in spike rate at higher input levels is due to the increase in synaptic current that occurs for the same driving force when the conductance is increased. Overall, the good matches observed between model responses and our previous dynamic clamp study indicate that the model and the recorded neurons responded reliably to the same features in inhibitory input conductance.

Spike precision of spontaneous activity in the model was highly dependent on the amplitude of the added noise. Although the level of noise was tuned only to replicate the amplitude of subthreshold voltage fluctuations, the model also reproduced comparable values of spike-time precision in spontaneous spiking. In addition, our simulations with dynamic clamp stimuli show that the model with this level of noise also replicated the spike timing precision benchmark measurement and its dependence on input gain and synchronicity as observed in recordings, although some deviations in the absolute values of precision existed at low and intermediate levels of synaptic gain (Fig. 13A). In additional simulations, we sought to address the question of what role the level of membrane noise plays in the control of spike timing precision by synaptic input. To address this question we repeated the dynamic clamp simulations for two additional levels of noise, a high level of noise with a standard deviation of 720 pA (Fig. 13C) and a low level of noise with a standard deviation of 60 pA (Fig. 13B). As expected, for a low level of noise, the spike-time precision increased across all input conditions. This effect was especially pronounced in the absence of input synchronicity where noise contributed most to spike timing variability. In contrast, a low level of noise did not result in a change in output spike rate nor in the spike-triggered average of inhibitory conductance.

This independence of output spike rate and spike triggered conductance average was also seen at a high level of applied noise current (Fig. 13C). The effect of a high noise level on spike timing precision was opposite to that of reduced noise, as the spike-time precision decreased for all combinations of input gain and synchronization. This resulted actually in a improved match between model and recordings for spike time precision in the case of no or intermediate input synchronicity, but a worse match for high input synchronicity. These

observations suggest that our simplified simulation of noise as a purely somatic current may not fully reproduce the biological noise source in its effects on spike precision under different input conditions. However, the simulations using our default level of noise showed all qualitative dependencies of input conditions on spike precision seen in recordings as well as reasonable quantitative matches for all input conditions, and was therefore fully sufficient to examine how distributing the same synaptic input patterns across dendrites may affect the control of spike output.

3.3.2 Contributions of the SK conductance to synaptic coding

The SK current has been implicated in regularizing spiking [60, 265] through forming a medium-duration spike-afterhyperpolarization (mAHP), suppressing bursts [39] and reducing sensitivity to small input fluctuations [60]. In order to determine the role of different amounts of SK current in an individual neuron we first compared responses to inhibitory dynamic clamp input patterns before and after blocking SK with the highly selective drug apamin. Apamin has been shown to abolish the SK-dependent mAHP and induce a switch from rhythmic pacemaker activity to spontaneous bursting activity in DCN neurons [3, 74] and in other neurons with SK channels [21, 57, 176]. Electrophysiological recordings were made from DCN neurons in rat cerebellar slices before and after SK block. These experiments were performed by Steven Feng in the lab of Dieter Jaeger. With native AMPA/NMDA and GABA synaptic input blocked, we observed tonic spontaneous regular spiking at frequencies ranging from ∼7 to 15.2 Hz before apamin block (Fig. 14A). Recordings were obtained from a total of 17 neurons from all three cerebellar nuclei. Sampled neurons consisted of both transient and weak burst rebound phenotypes [170]. Negative current injection pulses revealed the different responses to hyperpolarization exhibited by these two types of bursters (Fig. 14B). We also observed three neurons without a fast AHP preceding the mAHP, likely corresponding to GABAergic neurons as previously reported [245]. However, the SK- dependent mAHP depth was not significantly different between cells with different rebound or fast AHP types. After the application of 100 nM apamin, we observed the abolishment of the mAHP, and subsequent bursting behavior in

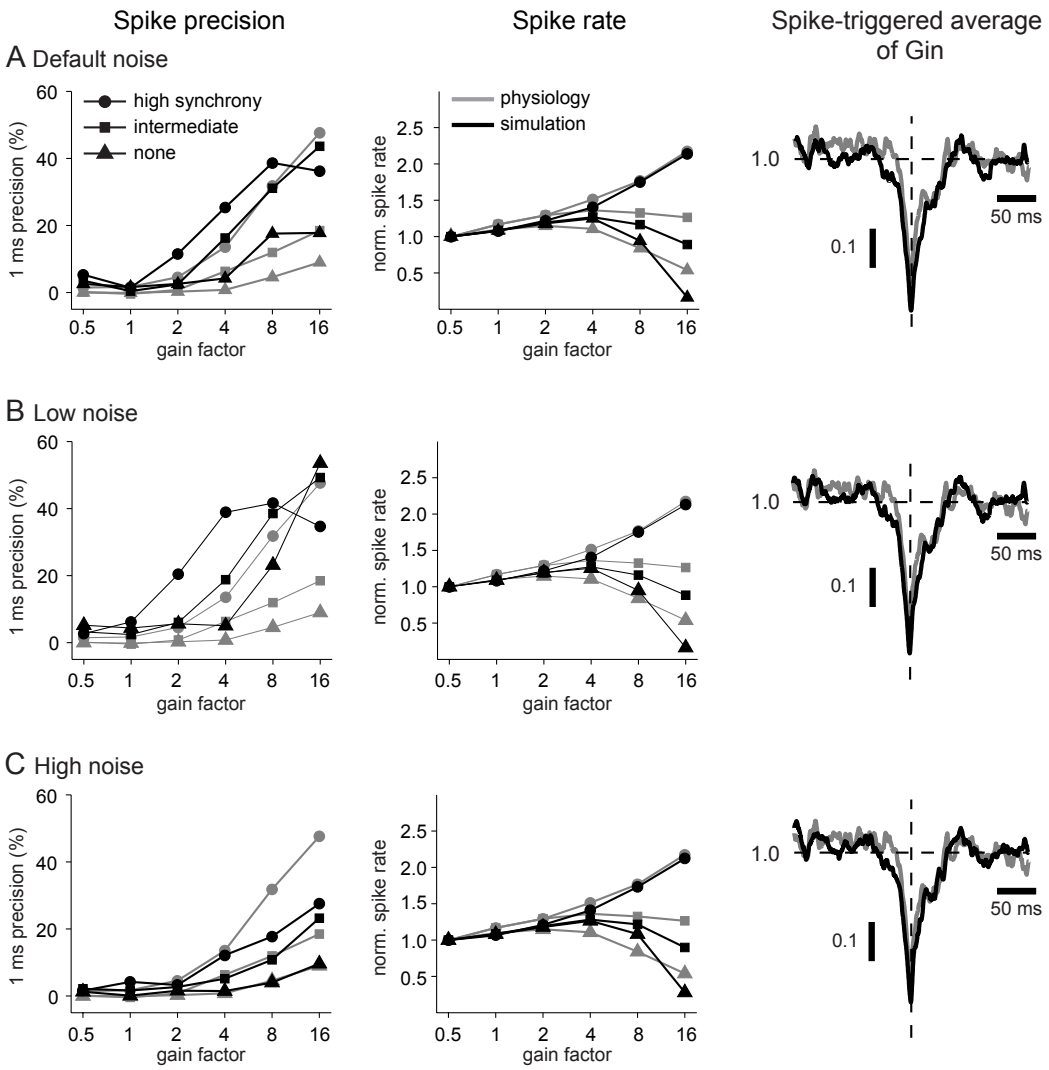

Figure 13: Spike-time precision and spike frequency for three different levels of noise in the model. (A, left) Spike-time precision increases with both input gain and synchronicity for recorded neurons (gray) and for the model (black). The relationships between precision and gain are preserved in the model although precision values are slightly higher. (A, middle) Spike frequency increases with input gain at high input synchronicity but actually decreases for intermediate or no input synchronicity. Spike frequency is normalized by the value at a gain of 0.5. The mean spike frequencies at a gain of 0.5 for the model were 12.4 Hz (high synchronicity), 12.7 Hz (intermediate synchronicity), and 12.7 Hz (no synchronicity). The mean spike frequencies at a gain of 0.5 for the recordings were 10.0 Hz (high input synchronicity), 9.0 Hz (intermediate synchronicity), and 10.2 Hz (no synchronicity). (A, right) The spike-triggered average (STA) of inhibitory conductance (normalized to the mean conductance value) for high input synchronicity and gain 16 is similar for both the model and recorded neurons. The transient drop in STA conductance indicates that spikes were triggered by brief pauses in Purkinje cell input. The relationships between precision and output spike rate with input gain and synchronicity and the STA of inhibitory conductance are shown for additional levels of low noise (B) and high noise (C). For low noise, the mean spike frequencies at the gain of 0.5 were 12.4 Hz (high input synchronicity), 12.6 Hz (intermediate synchronicity), and 12.6 Hz (no synchronicity). For high noise, the mean spike frequencies at the gain of 0.5 were 12.4 Hz (high input synchronicity), 12.7 Hz (intermediate synchronicity), and 12.7 Hz (no synchronicity).

all cells (Fig. 14C). For the remainder of this study concerned with effects of SK current on the synaptic transfer function, all recorded cell types are treated as a single population.

To examine the effect of SK channels on DCN spike coding of Purkinje cell inputs, the same previously described dynamic clamp stimulus was applied before and after apamin block. This sample of cells (n = 17) exhibited the same spontaneous behavior as previously observed in response to apamin application as well as to the dynamic clamp. After apamin block resulted in a transition from regular pacemaking to pronounced bursting (Fig. 15A) the same dynamic clamp stimulus was applied (Fig. 15B). Several important observations can be made from these data. First, the apamin-induced burst pattern is stopped by the application of a synaptic conductance input pattern because the ongoing baseline of GABA conductance forces the membrane potential (V_m) close to the chloride reversal potential, here set at -70 mV with the dynamic clamp. This effect shows the advantage of dynamic clamping over a current waveform application without real-time feedback, as only dynamic clamping includes the changing driving forces with changing V_m that result in this critical stabilizing feature of synaptic conductances.

The second important observation is that the output spike pattern with the same synaptic input pattern has changed, indicating a strong influence of the SK current on the synaptic transfer function of DCN neurons. Blocking the mAHP allows much faster spike trains in the depolarized state. This allows depolarizing transients in the input waveform to result in a much stronger high-frequency response after apamin block than before (Fig. 15B, right). However, the faster spiking is not uncontrolled as the overall level of spike precision for repeated applications of the same input pattern is high, and is actually significantly increased after SK block for the sample of 8 neurons quantitatively analyzed (Fig. 16). A second effect that we observed in this condition is that the spike responses to weaker depolarizing input transients were diminished (Fig. 2B, right panel) in that spikes reliably triggered by such transients before apamin application were missing afterwards. Both effects taken together resulted in a synaptic transfer function that showed an increase in both shorter and longer inter-spike intervals (ISIs), while showing diminished ISIs of intermediate duration (Fig. 17A) that were set by the pacemaker properties of the SK dependent mAHP.

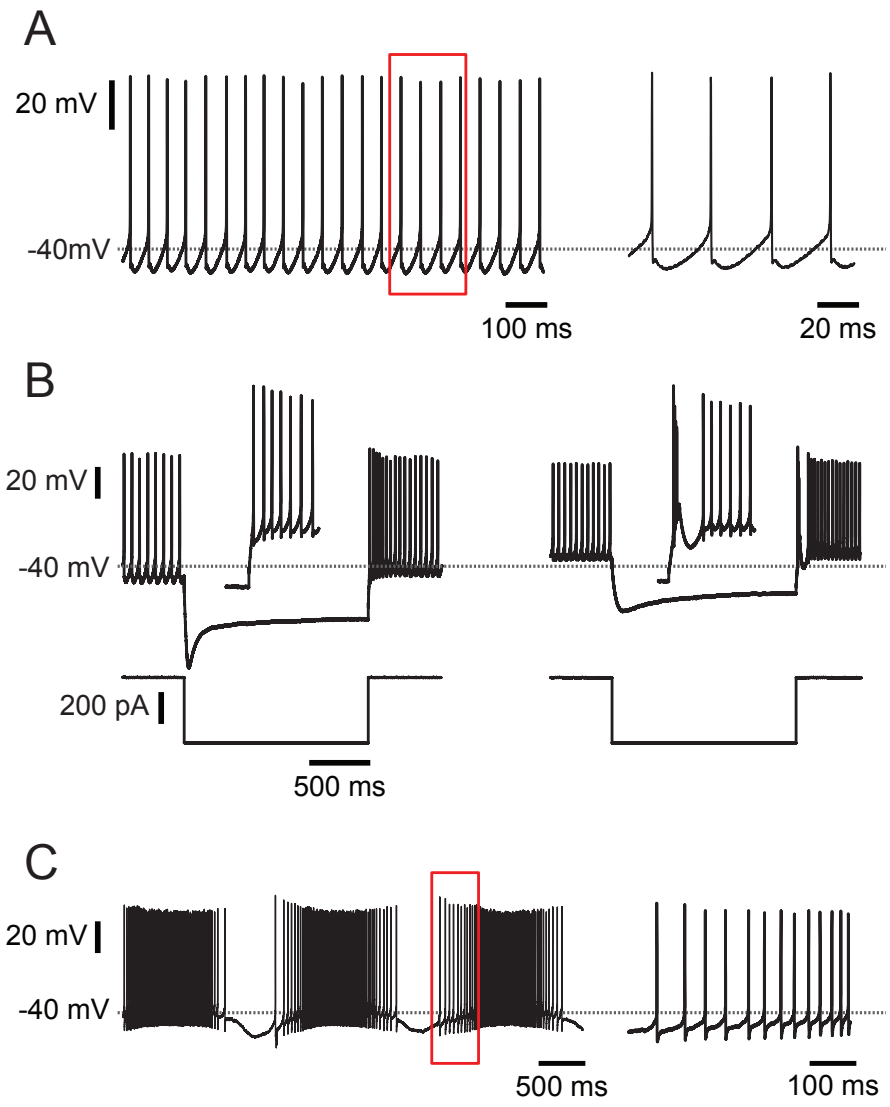

Figure 14: A) Membrane voltage of baseline spontaneous activity of a DCN neuron. On the right is an expanded inset of the boxed area. Note the pronounced mAHP waveform. B) Voltage response of a weak rebound burster (left) and a transient rebound burster (right) to -400 pA current pulse injections. C) Membrane voltage of spontaneous activity of neuron from (A) after superfusion of 100 nM apamin. On the right is an expanded inset of the boxed area. Note that the mAHP is fully blocked.

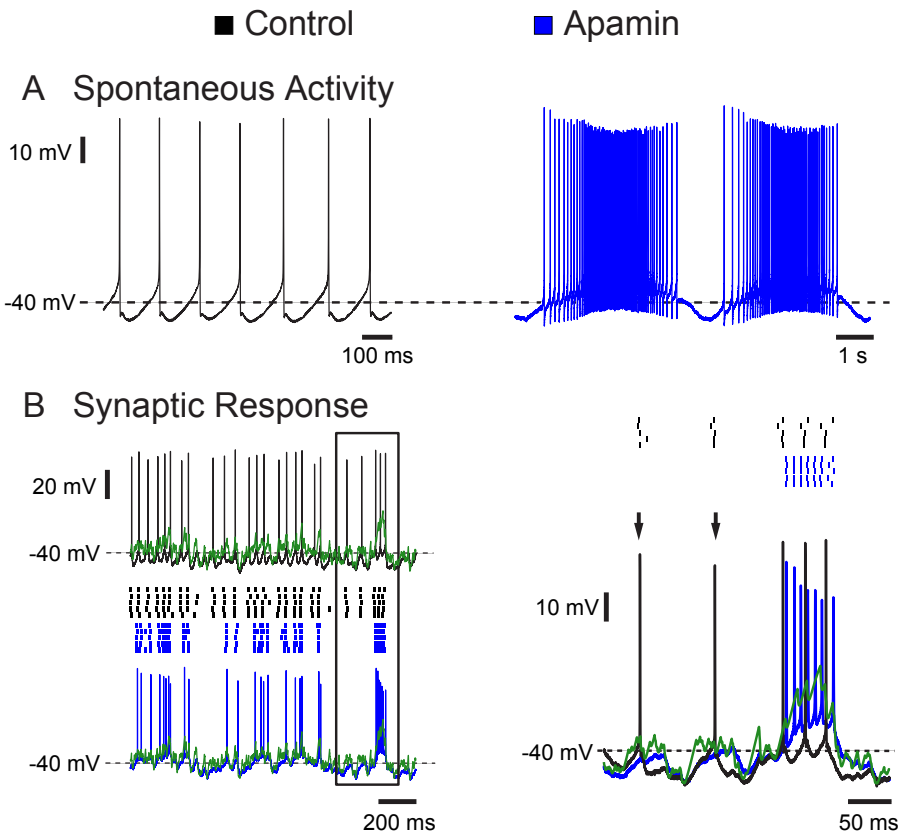

Figure 15: SK Block by apamin alters the spike response pattern elicited by synaptic input applied via dynamic clamp. A) Spontaneous activity of a DCN neuron before (black) and after superfusion of 100 nM apamin (blue). B) Stimulus-aligned voltage responses to a synaptic conductance input pattern applied via dynamic clamping on the left before (black) and after apamin (blue) superfusion. Spike raster plots for 5 stimulus repetitions are shown in the center and the temporal waveform of the combined reversal potential of inhibition and excitation (E_{syn}) is shown in green. On the right is an expanded inset of the boxed area overlaying the voltage traces. The loss of certain isolated spike events (arrows) and the presence of fast frequency spiking with a large depolarizing stimulus event are evident after the application of apamin.

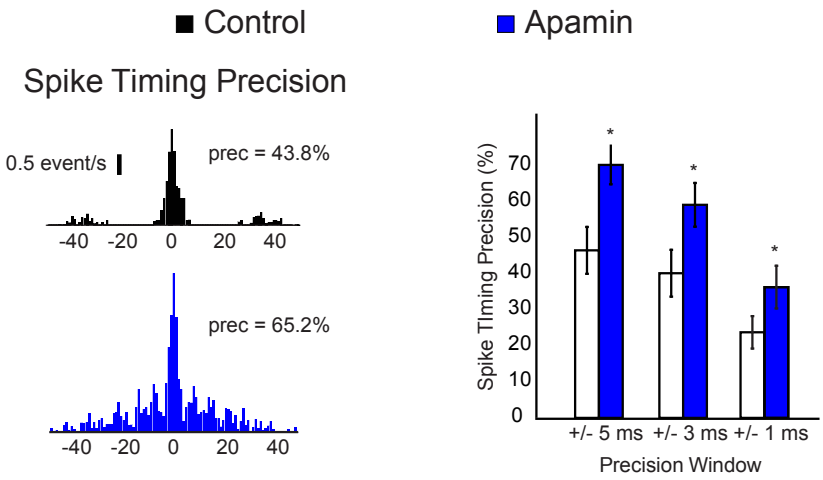

Figure 16: Spike timing cross-correlograms reveal time-locked responses to specific input events across trials. Left) Cross-correlograms of the spike responses across 5 repeated applications of the same synaptic conductance waveform applied both before (top) and after apamin presentation (bottom). For a precision window of ±3 ms, this neuron had 43.8% of spikes repeated at the same time across trials in the baseline condition and 65.2% following apamin. Right, the percentages of aligned spikes for ± 5, 3, and 1 ms precision windows for 8 recorded neurons. For all tested precision windows, the SK blocked condition yielded significant higher spike precision values ($p < 0.05$, $n = 8$).

Therefore the overall function of the SK current could be described by increasing a contrast function by which weak and strong input transients were able to control output spiking, resulting in stronger spike responses to large input transients and weaker ones for small input transients.

I used computer simulations to replicate the mechanisms underlying the changed synaptic response function after SK block. While we had a clear hypothesis that the increased spike response to strong input transients are explained by an abolished mAHP, the reduction of responses of weaker transients is hard to explain by a reduced potassium current that should result in a more depolarized V_m. We hypothesized that a plausible mechanism for this effect was an increased steady-state inactivation of the fast voltage-gated Na channel (NaF) and a concomitant increase in spike threshold. The NaF conductance in DCN neurons was previously shown to have a high component of steady-state inactivation at baseline [203]. However, in our experimental data we could not determine a clear depolarized shift in spike threshold after SK block. A small shift that is experimentally hard to determine could have been missed, and one goal of our computer simulations that included

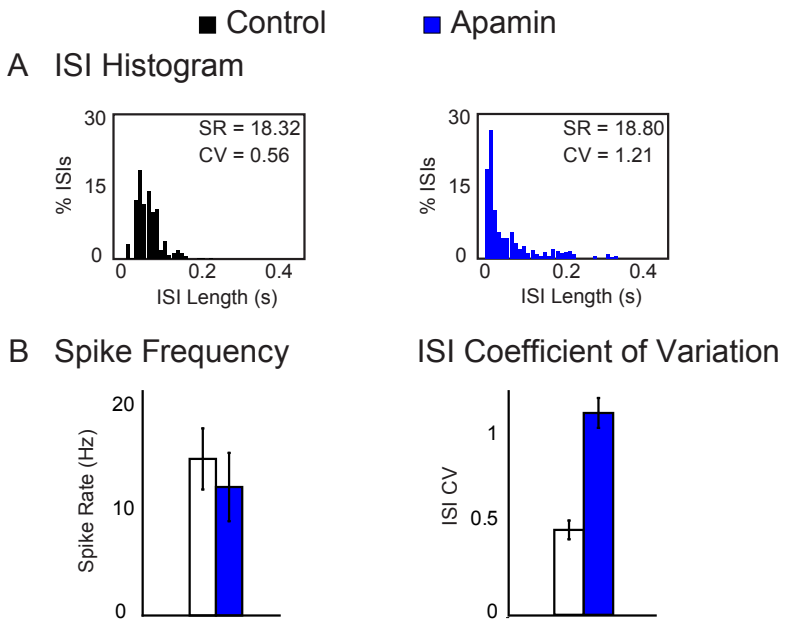

Figure 17: Apamin changes the histogram of interspike intervals and the coefficient of variation (CV) of spiking. A) Histograms of inter-spike intervals (ISIs) in response to dynamic clamp-applied synaptic input. High frequency bursts elicited by larger depolarizing events lead to an increase in the number of shorter ISIs. The loss of some responses to smaller synaptic events leads to an increase in the number of longer ISIs as well. The shift in the ISI distribution leads to a large change in the coefficient of variation (ISI-CV), from 0.54 to 1.21, while the spike frequency (SR) is nearly unchanged after apamin presentation (18.32 Hz vs. 18.8 Hz). B) Spike frequency remains statistically unchanged while ISI-CV increases significantly ($p < 0.001$) after apamin presentation.

NaF conductance with steady-state inactivation to match the experimental data was to ascertain this effect.

The effect of apamin was simulated by setting the SK conductance in the model to a value of zero. This block resulted to a considerable speedup in spiking and the loss of the mAHP (Fig. 18A, bottom). However, a burst pattern of spiking was not observed, presumably because the model does not include important slow dynamic variables such as calcium buffering and ionic pumps. Removing the SK conductance in the model resulted in a two-fold increase in spike rate and a significant increase in the ISI CV. As in the experiments an increased spike response to large input transients and an increase in short ISIs was observed (Fig. 18B(ii)). However, the reduction of spiking for weak input transients was not observed, and NaF inactivation was not sufficiently increased to elevate the spike threshold to make such an effect possible. As an alternative explanation to reduced spiking with weak input transients we posed the hypothesis that a constant negative bias current was present in addition to SK conductance block. Application of just -40 pA (Fig. 18B(iii)) bias current indeed lowered the model's responses to weak input transients, while maintaining an elevated response to strong transient reductions in inhibition. In fact, the results obtained with such additional bias current resulted in a spike rate and CV change that were close to experimentally obtained values (Fig. 17B).

The computer simulations predicted that the observed effects on the synaptic transfer function could be explained with two distinct mechanisms: an increased responsiveness to large input transients due to blocking the mAHP, and a decrease in responsiveness to smaller input transients due to an overall hyperpolarizing shift. One potential cause for such a shift could be given by the pronounced bursting pattern induced by apamin that developed for several minutes before the dynamic clamp stimulus was applied. The extreme spike rates and depolarized potential during the bursts might lead to a compensatory hyperpolarization for example by calcium-induced processes. To test this hypothesis, we performed recordings from another set of cells, in which the DCN neurons were voltage-clamped to -60 mV as soon as irregular spiking was observed in response to apamin (Fig. 19A). This had the effect of suppressing full-blown bursting and this burst suppression (BS) was used at all times

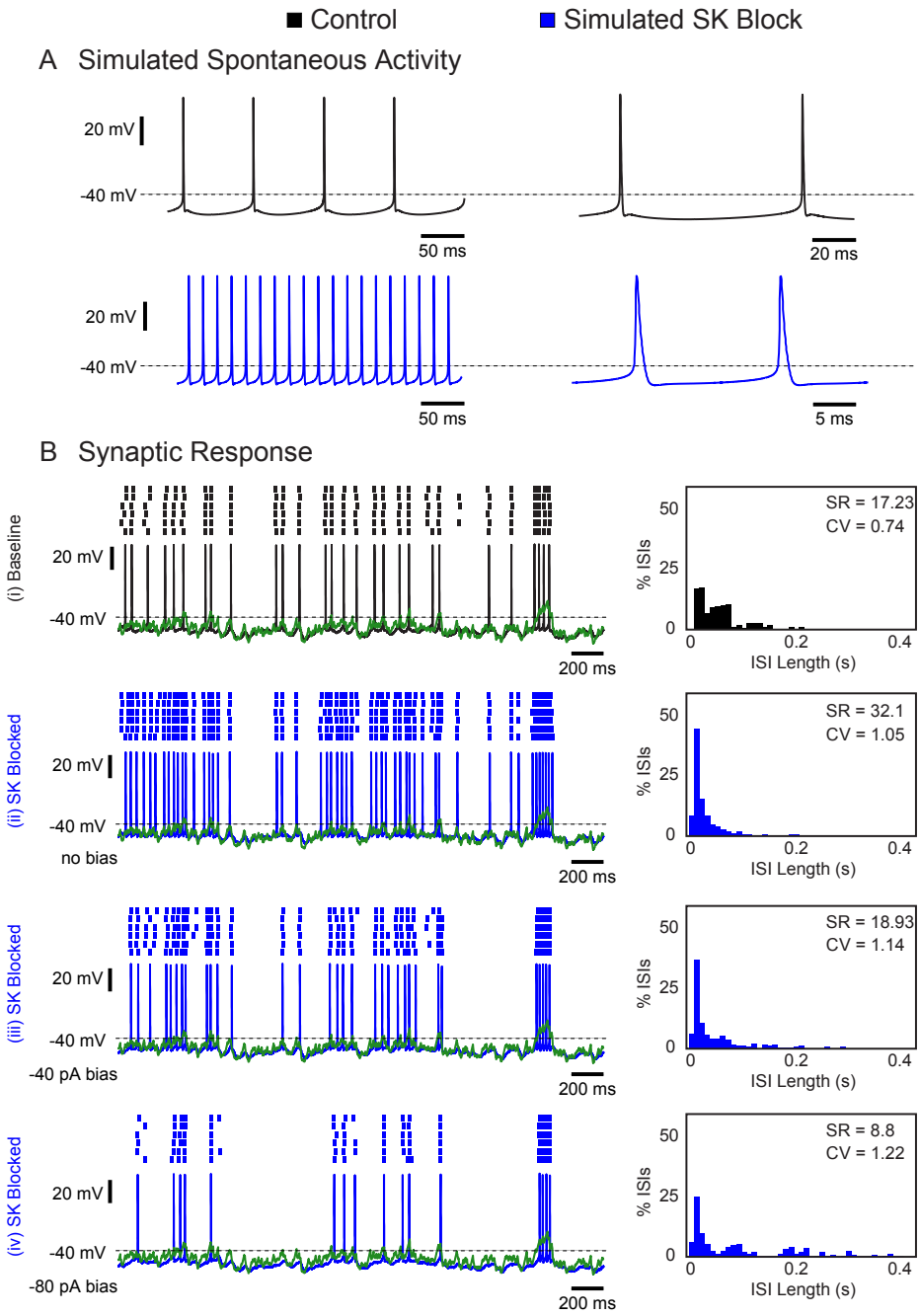

Figure 18: Computer simulations suggest that two distinct mechanisms are required for observed effects of SK block on synaptic spike response function. A) Spontaneous activity of the DCN model neuron before (black) and after (blue) simulated SK block. To simulate apamin application, SK channel density was reduced to zero in the DCN model neuron. B) Stimulus aligned voltage response of the DCN model to simulated dynamic clamp stimuli with and without SK conductance and varying levels of somatic bias current. SK block alone resulted in an increase of spike responses to weak and strong transient reductions in Purkinje cell input. Adding an additional negative bias current of -80 pA (bottom trace) abolished the response to weak transients, while the response to strong transients remained above baseline excitability. The ISI histograms for trials with negative bias show a widening of the ISI distribution and increase in CV similar to that observed in the experiments.

except during dynamic clamp in current clamp mode. This was possible using an Axon Multiclamp 700B, which allows fast software-based switching between voltage clamp and current clamp modes. We observed that when DCN neurons were burst suppressed after apamin presentation, responses to larger depolarizing input transients were still enhanced and often consisted of short high frequency bursts (Fig. 19B).

However, in contrast to the observed reduction in responses to small input transients seen in freely bursting (FB) DCN neurons (Fig. 14B), responses to smaller depolarizing input transients were not reduced after apamin presentation, but were in fact slightly enhanced as well. The spike timing precision remained unchanged (n = 7), but the spike ISI CV was significantly increased as in the freely bursting cells (Fig. 20B). The spike rate also tended to increase, but not significantly. These data are in fact similar to those seen with a pure SK block in the computer simulations. Therefore, apamin-induced bursting is likely responsible for an overall hyperpolarizing shift in the recorded neurons that could be induced by an increased tonic K+ conductance or a decreased tonic non-specific cation current present in DCN neurons [203]. In the absence of such a hyperpolarizing shift, the role of SK current with respect to synaptic integration can be described by a gain control function: an overall decrease in responsiveness to input transients that in particular reduces the maximal spike frequency for strong depolarizing input transients. As the predominant signal stream is expected to originate with inhibitory inputs from Purkinje cells, such transients would be given by synchronous pauses in a population of Purkinje cells. Nevertheless, transient increases in mossy fiber excitation could also result in similar spike responses.

We next asked whether our understanding of the SK conductance could fully account for the observed gain changes in the synaptic transfer function. To address this question we added back a fully controlled artificial SK conductance with dynamic clamping after blocking the intrinsic conductance with apamin. First, the intrinsic SK conductance was fully blocked with apamin. Then the real-time loop of the dynamic clamp algorithm was expanded to include a simulated voltage-dependent source of calcium into a simulated compartment, as well as a mechanism of exponential extrusion from this compartment. An artificial SK conductance was linked to this simulated calcium pool and the resulting

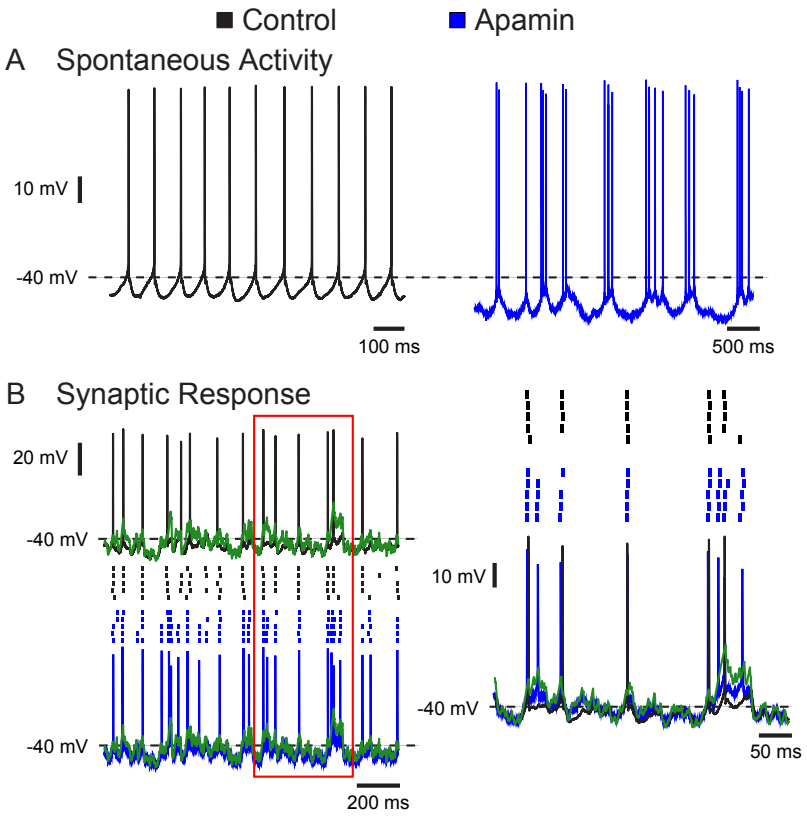

Figure 19: Suppression of spontaneous bursting after SK bslock prevents loss of responses to weak depolarizing input events applied with dynamic clamp. A) Spontaneous activity of a DCN neuron before (black) and after superfusion of 100 nM apamin (blue). This burst suppressed (BS) neuron was voltage-clamped to a holding potential of -60 mV to prevent spontaneous high frequency bursting. The neuron was released from voltage clamp only during the time of dynamic clamp stimulus application. B) Stimulus aligned voltage responses of a BS neuron to a synaptic conductance input pattern applied via dynamic current clamp on the left before (black) and after apamin (blue) presentation. Raster plots are shown in the center and E_{syn} is depicted in green. BS neuron responses to weak depolarizing events were almost never reduced, unlike that seen for FB neurons (Fig. 15B), but fast frequency burst responses were still only associated with large depolarizing events. On the right is an expanded inset of the boxed area.

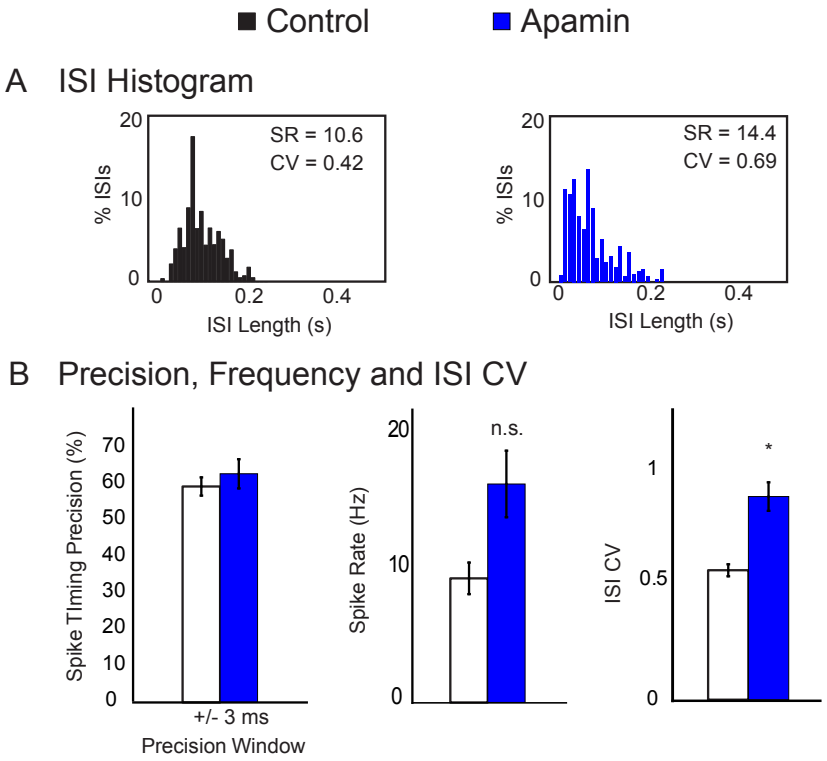

Figure 20: Interspike interval histograms show an increase in shorter ISIs while maintaining spike time precision after apamin application to DCN neurons. A) ISI histograms of the same BS neuron responses to dynamic clamp-applied synaptic input. The increase in responses to both large and small depolarizing events lead only to an increase in the shorter ISIs. Both the SR (10.6 Hz to 14.4 Hz) and ISI CV (0.422 to 0.687) of the BS neuron depicted in (B) increase after apamin presentation. B) The data from all 7 BS neurons show a maintained spike time precision during in responses to dynamic clamp stimuli, but a significant increase in ISI CV (paired t-test, $p < 0.001$) and a non-significant increase in spike rate (paired t-test, $p = 0.1$).

I_{SK-art} was applied back to the recorded neuron [74]. Previous experimental work has indicated that high-voltage-activated calcium current in DCN neurons is the only source of calcium driving SK activation [6]. The same equations used in the DCN model were used for the dynamic clamp feedback algorithm (Appendix A) but the voltage driving the activation function was taken in real-time from our recording.

The artificial SK conductance applied by dynamic clamp was able to restore the mAHP and regular spontaneous pacemaking activity after apamin was applied to block intrinsic I_{SK}. To achieve good matches between the recordings with I_{SK-art} and the pre-apamin spike shape, the time constant for calcium decay as well as the maximal SK conductance had to be adjusted for each recorded cell (n = 5 BS recordings). After G_{SK-art} was tuned to restore the spontaneous spike shape, the same dynamic clamp stimulus was applied to determine whether G_{SK-art} could also replicate the original baseline synaptic response function. The responses to Purkinje cell input patterns began to resemble the original pre-SK block pattern as an increasing amount of G_{SK-art} was applied. For a value of 3.5 nS maximal G_{SK-art}, responses to large depolarizing transients in the synaptic input (indicated by vertical grey dotted lines in Fig. 21) had fully reverted from spike bursts to single spikes (Fig. 21(v)) and were similar to the pre-apamin baseline case (Fig. 21(i)).

Overall, these results indicate that a spike-associated inflow of calcium via HVA calcium channels and the SK conductance triggered by this calcium inflow is fully sufficient to account for an important gain shift in the synaptic transfer function. We made the unexpected observation that apamin-induced burst firing itself in DCN neurons leads to a reduction of general excitability, which our computer simulations suggest could be due to an increased outward bias in the mean intrinsic currents. This additional apamin-induced excitability regulation resulted in an enhanced gain control of the synaptic response function, such that small input transients failed to trigger any spike responses. The combined effect of reduced excitability and increased responsiveness to large input transients is best described as tuning a synaptic response contrast function, in that the contrast between responses to small and large input transients was highly increased after apamin when cells were allowed to burst.

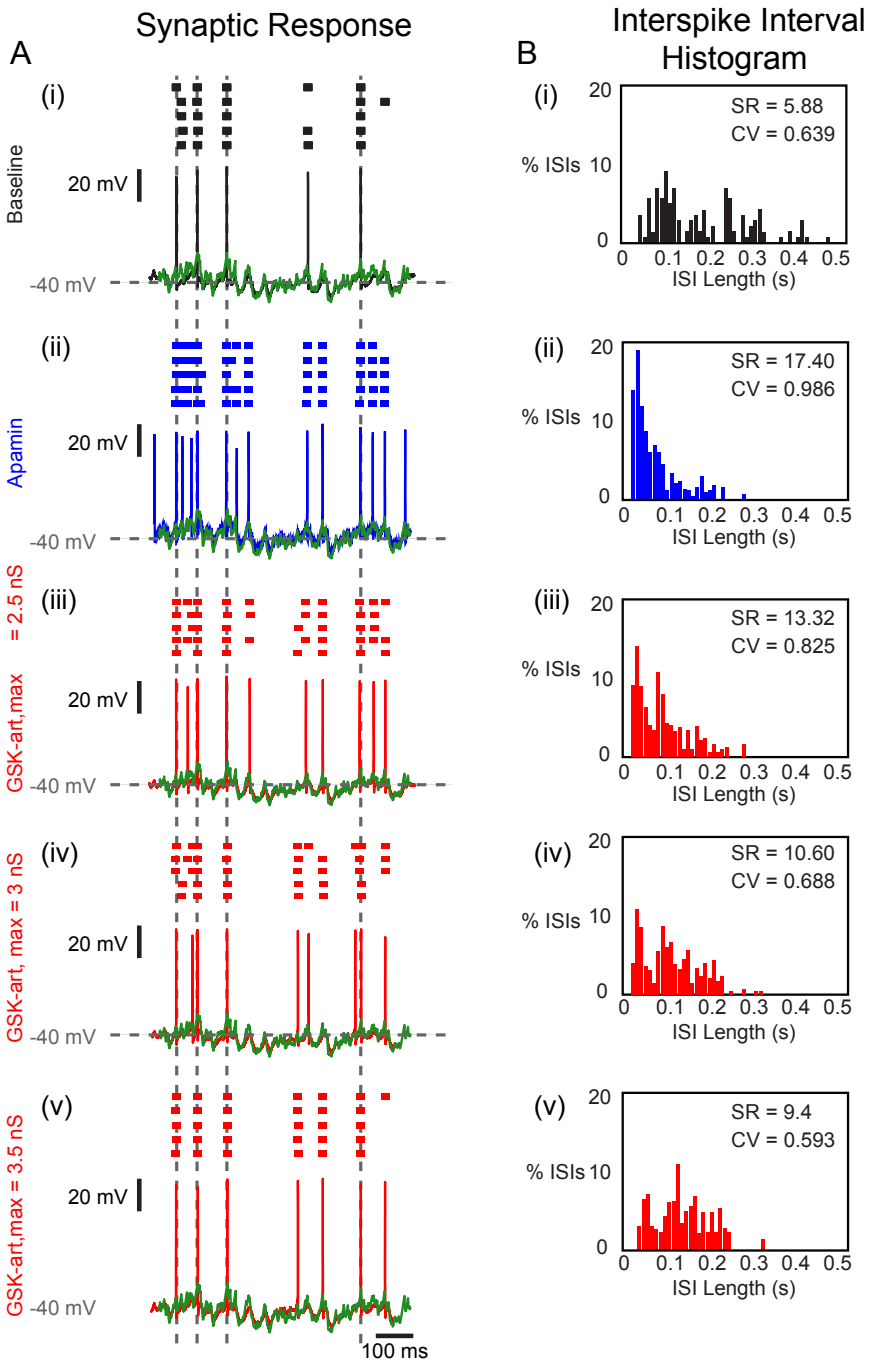

Figure 21: Recovering the synaptic response function with an artificial SK current after SK block. A) Stimulus aligned voltage responses of a BS neuron to the input pattern applied via dynamic current clamp before apamin presentation (black), after apamin presentation (blue), and with G_{SK-art} added (red) after apamin application at multiple levels of maximal conductance ($G_{SK-art,max}$). Raster plots are shown above each voltage trajectory and E_{sun} is shown in green. The SK-blocked response patterns resembled the baseline patterns most closely for the $G_{SK-art,max}$ level of 3.5 nS (iii). This is particularly noticeable at the time points indicated by the dotted grey lines, as apamin-induced bursting responses were greatly reduced by the insertion of G_{SK-art}. B) ISI histograms of the neurons response patterns from (A). After apamin superfusion, the ISI distribution shifted towards the left, as a result of the high frequency burst responses. The percentage of the shortest ISIs decreased with the increasing levels $G_{SK-art,max}$.

The strong involvement of SK current in shaping the synaptic response function is overall another clear example that intrinsic dynamic properties of neurons make an important contribution to network processing [72,164], and should be carefully considered in network simulations of neural function. The direct consequence of SK function for motor control remain to be determined. Our results suggest that a general gain increase in responsiveness of cerebellar circuits could be mediated by cell-specific SK downregulation, which would allow selective activation of learnt behaviors. Recently it is becoming clear that understanding the detailed mechanisms of intrinsic channel properties and their regulation is also important in understanding and treating neural dysfunction [16]. Specifically, the SK current has been implicated as a potential modulator of cerebellar ataxia, and enhancing SK current with a pharmacological activator could reduce disease symptoms [5, 215, 255]. This effect could be in part mediated by a reduction of burst responses in the DCN that are likely induced by the pronounced Purkinje cell synchronization in this disorder. Pathological cerebellar activity also underlies some forms of cerebellar dystonia [37, 132], which may be caused by enhanced Purkinje cell bursting and synchrony leading to enhanced bursting in DCN activity [149, 150]. Therefore, previous work in conjunction with our new results point squarely at the SK current as an important regulator in the synaptic processing of normal and dysfunctional cerebellar output and SK activators as a promising drug target for disorders with abnormally high response gains.

As seen in many other cell types [27,28,176] and in DCN neurons [3,6] before, SK block with apamin resulted in the abolishing of the mAHP waveform and in highly irregular or burst firing. When we applied in-vivo like synaptic Purkinje cell input patterns, the effect of the abolished mAHP waveform was an enhanced spike response to synchronous reductions of Purkinje cell inputs. Such synchronous pauses in Purkinje cell activity have been hypothesized to be a potential code for Purkinje cell to DCN signal transmission [56, 82, 224]. A reduction of SK would therefore increase the gain of this mode of transmission. Less synchronous Purkinje cell activity results in a more steady-state inhibitory synaptic conductance, and in fact weak input transients were not amplified in our data, pointing to a selective enhancement of strong input transients by a reduction in SK current. While we did

not pursue the question of which signaling pathway in DCN neurons results in a reduction of SK current, the presence of such pathways in other cell types by protein phosphatases linked to cholinergic transmission [87, 165], LTP induction [19] or metabotropic receptor activation [229] points to a likely plasticity of SK current in DCN neurons as well. In fact, while recordings from young rodents (< 20 days) show a relatively consistent large mAHP amplitude, the results for adult mice are more variable and often the mAHP is near absent in adult mouse DCN during spontaneous pacemaking. This observation favors the speculation that in young pre-weanling animals a high level of SK current promotes responsiveness to small input transients while preventing burst responses, whereas in adult animals excitability plasticity has stabilized large responses to functionally relevant large input transients originating from behaviorally meaningful synchronized Purkinje cell activity.

3.3.3 Comparison between focalized and distributed synaptic inputs

A major limitation of dynamic clamp is that the artificial conductances are focally applied only at the site of the electrode, in this case the soma, and may not realistically represent the effects of distributed dendritic synapses. Distributed synaptic input was simulated by relocating synapses from the soma of the model neuron to dendritic compartments such that the summed synaptic conductance waveform remained the same. For high input synchronicity and a mean inhibitory input level of 16 nS, the mean subthreshold membrane potential was slightly more depolarized for focalized inputs (-53.3 mV) than for distributed inputs (-53.9 mV). Spike heights were also approximately 3-4 mV shorter for focalized inputs, which is likely due to the increased local shunting of spike conductances when the input is focused at the soma. We found that the spike pattern induced with a simulated dynamic clamp at the soma in this model was very similar to the spike pattern induced with the same synaptic conductance patterns applied through a set of distributed dendritic synapses (Fig. 22A). Although the exact timing of individual spikes was slightly different for these two input conditions when the same pattern of frozen noise was applied to the soma, changes in spike rate due to depolarizing or hyperpolarizing transients in E_{syn} clearly matched.

This similarity in the action of focal and distributed input can be explained by the relatively electrotonically compact structure of DCN neurons. In a passive morphology in which the large majority of dendritic surface is within 0.2 λ of the soma, little attenuation occurs in the dendrites for low-frequency voltage signals caused by synaptic inputs. We found that somatic membrane voltage fluctuated similarly for purely somatic or distributed dendritic inputs (Fig. 22A), and that dendritic voltage-gated currents were evoked in a very similar pattern in both input conditions (Fig. 22C). In the model, action potentials triggered the inward calcium HVA current, increasing the intracellular calcium concentration that drives SK channel activation. For both purely somatic or distributed synaptic input these currents were evoked with similar time courses and amplitudes in the soma (Fig. 22B) and in the dendrites (Fig. 22C). The SK current dominated the intrinsic currents in the middle of inter-spike intervals, and makes a particularly strong contribution to spacing between spikes [74]. Therefore the similarity of the time course of this current both in the soma and the dendrites between focalized and distributed input conditions allows for closely matching spiking responses.

The added noise in the model contributed not only to spike time jitter, but also caused "extra" or "missing" spikes across trials. In our sample of brain slice recordings, although some spike times did occur with high reliability between neurons given the same stimulus, the variability in spike pattern was still quite high (Fig. 23). In fact, the spike patterns found for somatic or dendritic input conditions in the simulated neuron are much more closely aligned with each other than different recorded neurons were. We quantified the similarity in the spike pattern by using the same spike-time precision benchmark described before. The average 1 ms spike-time precision was computed from cross-correlations of all pairwise combinations of trials. Across the set of biological neurons, the proportion of precisely aligned spikes was 23.0 $\pm$ 5.2% compared with 40.1% between simulations using somatic vs. dendritic input (Table 2). Furthermore, the average 1 ms spike-time precision between pairwise combinations of all the experimental trials with the simulations was 22.3 $\pm$ 2.8%, indicating that the spike patterns that emerged from the simulations are within the variability of the set of responses elicited from the biological neurons. Note that the

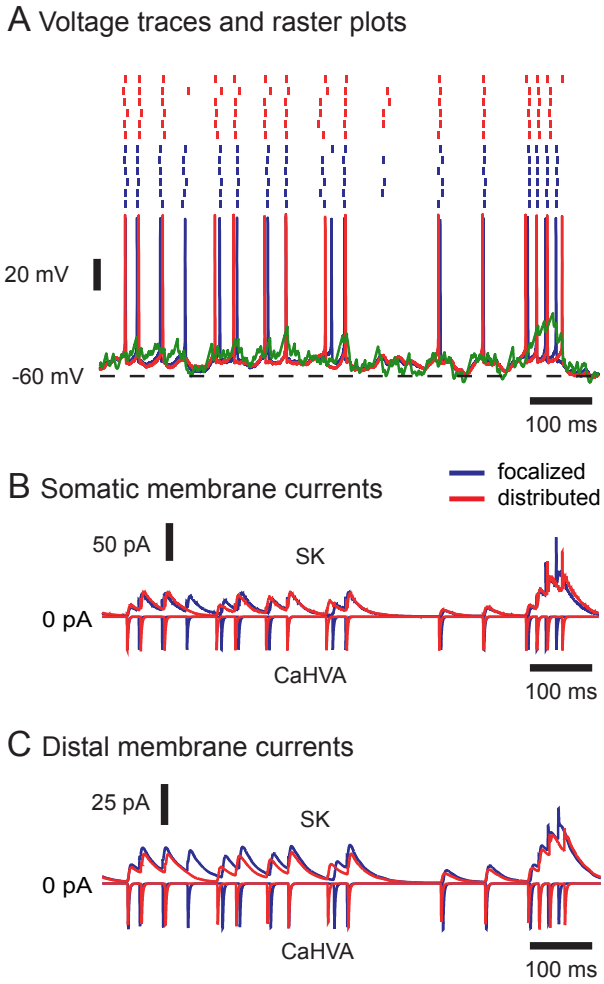

Figure 22: Comparison of responses to focalized or distributed inputs in the model. A) The same set of synaptic inputs was delivered focally at the soma or distributed over the dendrites and resulted in very similar membrane voltage trajectories and spike patterns. The SK and CaHVA currents in the soma B) and distal dendrites C) are activated similarly by focalized or distributed dendritic input, despite the very different localization of inputs.

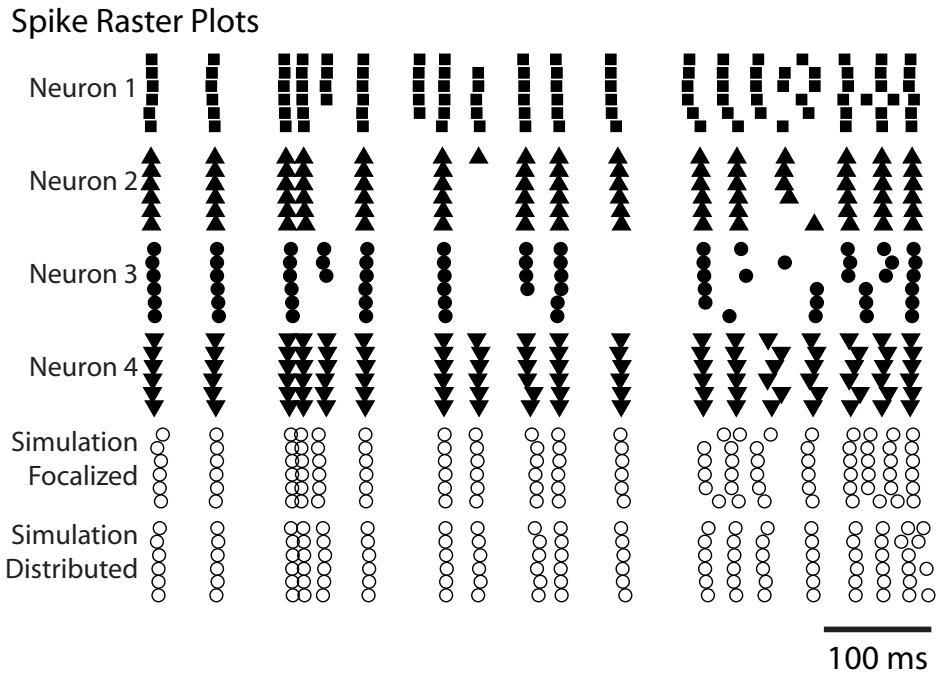

Figure 23: Comparison of output spike pattern for biological neurons and the model with focalized or distributed synaptic input. The model shows a similar spike pattern response to focal somatic synaptic input as recorded neurons under dynamic clamp. Note the variability in output spike patterns between recorded neurons given the same stimulus. Data are shown for a mean inhibitory conductance of 16 nS and high input synchronization.

spike responses of Neuron 4 in the experimental sample in particular very closely match the simulated responses.

In addition to a very similar spike pattern, the focalized and distributed synaptic input simulations also resulted in a similar dependency of spike precision and rate on input conditions (Fig. 24). Overall, spike frequency in response to these stimuli was about 0.2 Hz lower for distributed inputs than focalized inputs. This small difference in spike rate is probably due to the 0.6 mV more depolarized average V_m in the soma for focal input noted above. In addition, with distributed inputs, the model was slightly less sensitive to changes in input amplitude such that spike rates were not increased or decreased as much at different input levels. This is likely due to a decrease in synaptic shunting effects at the soma for distributed inputs. Nevertheless, the spike-triggered average of inhibitory conductance matched closely for both input conditions (Fig. 24C) indicating that spikes were evoked by

Table 2: The 1 ms spike-time precision computed from cross-correlations of all pairwise combinations of trials across the set of biological neurons and the neuron model with focalized or distributed synaptic input.

	Neuron 1	Neuron 2	Neuron 3	Neuron 4	Focalized	Distributed
Neuron 1	28.6%	24.3%	15.9%	19.6%	19.6%	19.7%
Neuron 2	-	34.9%	31.2%	22.7%	19.6%	20.9%
Neuron 3	-	-	30.5%	24.5%	22.3%	24.8%
Neuron 4	-	-	-	35.3%	25.0%	26.6%
Focalized	-	-	-	-	38.7%	40.1%
Distributed	-	-	-	-	-	37.2%

the same time course of disinhibition.

This similarity in the action of focal and distributed input can be explained by the relatively electrotonically compact structure of DCN neurons. In a passive morphology in which the large majority of dendritic surface is within 0.2 λ of the soma, little attenuation occurs in the dendrites for low-frequency voltage signals caused by synaptic inputs. When both inhibition and excitation were described by synaptic conductances, the mean firing rate of the model in response to purely stochastic input was 26.9 Hz for focalized inputs and 23.0 Hz for distributed inputs, which is similar to previously reported in vivo firing rates [6,148]. A simulated inhibitory input burst was sufficient to cause a nearly complete cessation of spiking in the model for both focalized and distributed input. The membrane potential was slightly hyperpolarized during the inhibitory burst but did not go below -60 mV. Thus, a pause in spiking was achieved without deep hyperpolarization, and without an ensuing rebound as is observed in the same model with much stronger inhibitory input bursts that hyperpolarize the membrane below -75 mV [233]. An inhibitory pause or excitatory burst resulted in an increase in firing rate that was more pronounced for the focalized input. This is consistent with the explanation that a purely somatic imbalance in excitation is somewhat more effective than the distributed case.

3.3.4 DCN response to patterned synaptic input

The synaptic background input used in our dynamic clamp study was purely stochastic with a stationary mean rate whereas DCN neurons in vivo are likely subject to strongly patterned

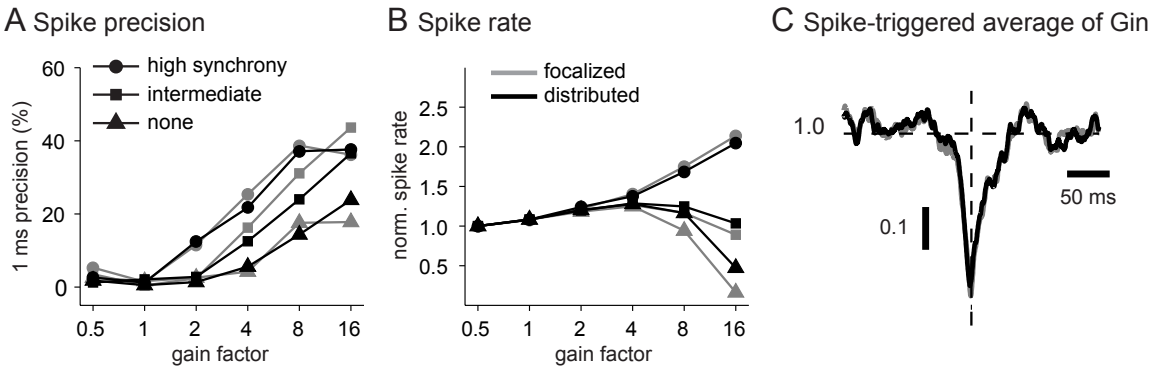

Figure 24: Spike-time precision and spike frequency for focalized or distributed inputs in the model. The relationship between spike precision (A) and spike frequency (B) with input gain and synchronicity was very similar for focalized inputs (gray) and distributed inputs (black). C) The STA of inhibitory conductance (normalized to the mean conductance value) for high input synchronicity and gain 16 showed that the same time course of disinhibition evokes spikes in both cases.

synaptic input due to bursts and pauses in Purkinje cell and mossy fiber activity in vivo. Prolonged increases or decreases in the simple spike firing rate of Purkinje cells have been observed in response to both sensory stimulation [163] and motor behavior [166]. Numerous studies have demonstrated correlations in simple and complex spike activity [145, 266, 267] that can be modulated by behavior [106, 107, 225] as well as correlated pauses in Purkinje cell firing that can mediate DCN activity [56, 224]. This correlated activity produces sharp fluctuations in input to DCN neurons that can then be encoded with high reliability. Mossy fiber input to the DCN is less well understood but their firing rate is known to be strongly modulated by movement with complex biphasic or triphasic activity patterns and high frequency bursts that can last up to several hundreds of milliseconds [204, 247].

To determine how strongly patterned synaptic input can shape the response of DCN neurons and whether the distributed input condition still resembles the focalized one, we added burst and pause features in addition to the background synaptic input in the model. We replaced the tonic level of excitation with mixed AMPA and NMDA synapses as in Gauck et al. (2003) and generated ten different stimuli of random background synaptic activity. Inhibitory input was modeled with an input level of 16 nS and intermediate synchronicity, which resulted in moderate fluctuations of input conductance so that the additional bursts and pauses could stand out against the background activity. Excitatory input was also

modeled with intermediate synchronicity with a gain such that mean excitatory conductance was 75% that of inhibitory conductance. For a 200 ms window of time, we imposed a burst or pause in inhibition or a burst in excitation. The mean firing rate of the model without an additional input burst or pause was 26.9 Hz for focalized inputs and 23.0 Hz for distributed inputs, which is similar to previously reported in vivo firing rates [6, 148]. The mean subthreshold membrane potential was again slightly more depolarized for focalized inputs (-52.5 mV) than for distributed inputs (-53.3 mV). A summary of the firing rates resulting from inhibitory and excitatory bursts and pauses is presented in (Table 3).

Table 3: Average firing rates for patterned synaptic input applied to the DCN model. Values are average spike rate during a burst or pause for patterned synaptic input.

	Focalized	Distributed
Base model		
Control (stochastic)	26.9	23.0
Inhibitory burst	1.0	1.5
Inhibitory pause	51.2	41.3
Excitatory burst (2X)	52.4	40.5
Excitatory burst (3X)	88.3	64.7
Model with stronger rebound currents		
Control (stochastic)	29.7	25.3
Inhibitory burst	4.7	3.0
Inhibitory pause	55.4	44.3
Excitatory burst (2X)	56.1	43.7
Excitatory burst (3X)	90.9	68.1

An inhibitory burst was modeled as a 200 ms long doubling of the 35 Hz firing rate in one half of the inhibitory synapses to 70 Hz, which was equivalent to an overall increase of 50% in the frequency of inhibitory inputs. An inhibitory input rate of 70 Hz is well within the range of reported Purkinje cell firing rates, which can reach rates of up to 100 Hz in vivo [11, 238]. This simulated inhibitory burst was sufficient to cause a nearly complete cessation of spiking in the model for both focalized and distributed input (Fig. 25A). The membrane potential was slightly hyperpolarized during the inhibitory burst but did not go below -60 mV. Thus, a pause in spiking was achieved without deep hyperpolarization, and

without an ensuing rebound as is observed in the same model with much stronger inhibitory input bursts that hyperpolarize the membrane below -75 mV [233]. For distributed but not focalized inputs, a few spikes still occurred shortly after the start of the burst (Fig. 25A, arrowhead), indicating that the model was a little slower to hyperpolarize following the increase in inhibition. These spikes all occurred within the first 20 ms of the burst. The similarity in spiking between focalized and distributed inhibitory burst input was paralleled by a similar change in intrinsic currents during the burst. Regardless of input location, the inhibitory input burst resulted in a near complete cessation of SK current both in the soma (Fig. 25B, left) and in the dendrites (Fig. 25B, right). It took an additional 50 ms after the end of the input burst before the SK current re-approached the control traces, again regardless of input location.

An inhibitory pause was modeled as a complete block of input from one half of the inhibitory synapses, which reduced the overall firing rate of the population of inhibitory inputs by 50%. This resulted in an increase in firing rate in the model to 58.7 Hz for the focalized input and to 46.1 Hz for distributed input (Fig. 26A), indicating that disinhibition is a highly effective condition to increase DCN spiking. The spike rate increase in the focalized input condition was noticeably higher, suggesting that the somatic location of the excitatory input when not compensated by inhibition was more effective in driving spiking than an identical pattern of distributed excitation. This difference was paralleled by a slightly higher increase in SK current activation for the focalized disinhibition over the distributed case in both the soma (Fig. 26B, left) and the dendrites (Fig. 26B, right). Nevertheless, the difference was relatively minor, and does not invalidate the use of dynamic clamping in the exploration of stronger disinhibitory input events.

The overall similarity in mechanism is also shown by spike-triggered averages of the conductances (Fig. 27). For both focalized (Fig. 27A), and distributed (Fig. 27B) input conditions, a pause in 50% of inhibitory inputs resulted in about a twofold decrease in the drop of inhibitory conductance before spike initiation. Note that the plotted conductance was normalized, so that the drop in conductance before a spike depicts the relative decrease in spike triggered conductance regardless of overall input rate. Therefore, the observed

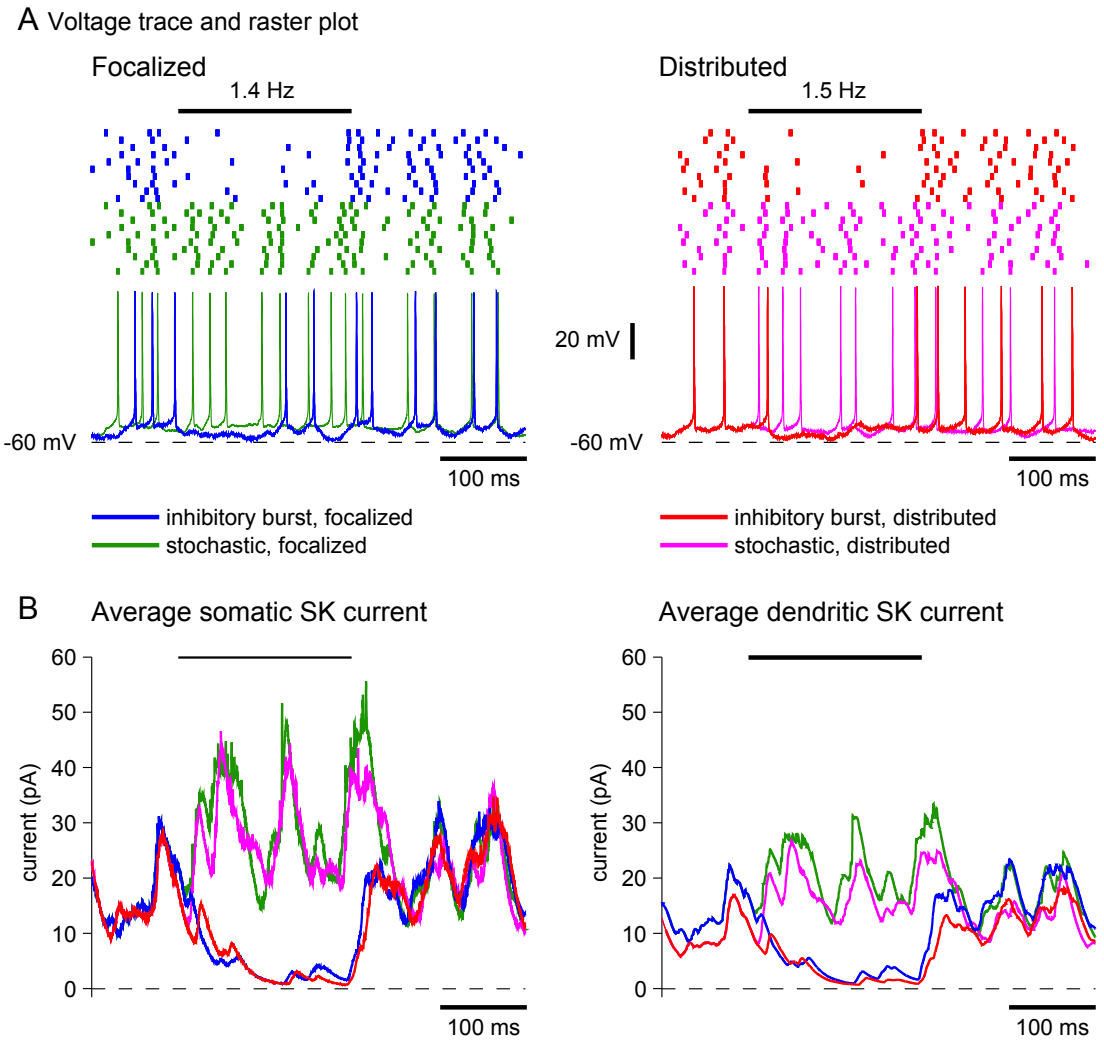

Figure 25: Response to an inhibitory input burst for focalized or distributed input in the model. The horizontal bar above the raster plots indicates the duration of the input burst. The mean firing rate in the control trials was 26.9 Hz for focalized inputs and 23.0 Hz for distributed input. Before the start of the input burst, spike times in the control and patterned trials were exactly the same. (A) A 50% increase in the inhibitory input rate caused a nearly complete suppression of spiking to a 1.4 Hz spike rate for focalized (left) and to a 1.5 Hz spike rate for distributed (right) input. For distributed dendritic input, the onset of spike suppression was not as complete during the first 25 ms, and in some trials spikes early during the inhibitory period were still present (black arrow). (B) During the inhibitory burst, the magnitude of the SK current strongly decreased due to the absence of spikes but returned to the control trajectory when the burst ended. The pattern of SK activation was similar for both the focalized and distributed input conditions. The average SK current across different noise conditions is shown.

decrease in the STA drop indicates that under the condition of reduced inhibition the timing of spiking is less precisely controlled by inhibitory inputs. In addition, the average increase in AMPA excitation prior to spike triggering was also reduced (Fig. 27, middle panel), indicating that it was an overall decrease in the precise relationship between input conductance and spike timing rather than a shift of spike control to excitation that was caused by disinhibition.

Though inhibitory Purkinje cell input is likely a dominant mechanism in controlling DCN activity, spike rate increases could also be caused by increased mossy fiber input. We simulated excitatory input bursts as a doubling of the original 20 Hz firing rate in one half of the excitatory synapses, yielding an overall increases of 50% in the frequency of excitatory input. This input condition had a similar effect to the case of an inhibitory pause, though the amount of firing rate increase was somewhat larger. The increase to 81.5 Hz spiking for focalized input was again higher than the increase to 61.2 Hz seen with distributed input (Fig. 26A). This is consistent with the explanation that a purely somatic imbalance in excitation is somewhat more effective than the distributed case. The STAs of synaptic conductances for increased excitation also showed similarities to the case of decreased inhibition (Fig. 27). The drop in inhibition prior to a spike was decreased about 50% compared to control, suggesting less inhibition-locked spiking. In contrast, the absolute size of AMPA conductance increase before a spike was about 50% larger during excitatory bursts, though there was no increase in the relative increase in excitation normalized to the increased total excitatory conductance during an excitatory burst. The similarity between GABA and AMPA transients related to spike initiation between focalized somatic and distributed dendritic input suggests that synaptic control of spiking is virtually unchanged between these conditions.

3.4 Discussion

3.4.1 Computer modeling in conjunction with dynamic clamping presents a powerful combined approach to study synaptic integration

We developed a computer simulation approach to examine differences between focalized somatic or distributed dendritic synaptic input in a morphologically realistic compartmental

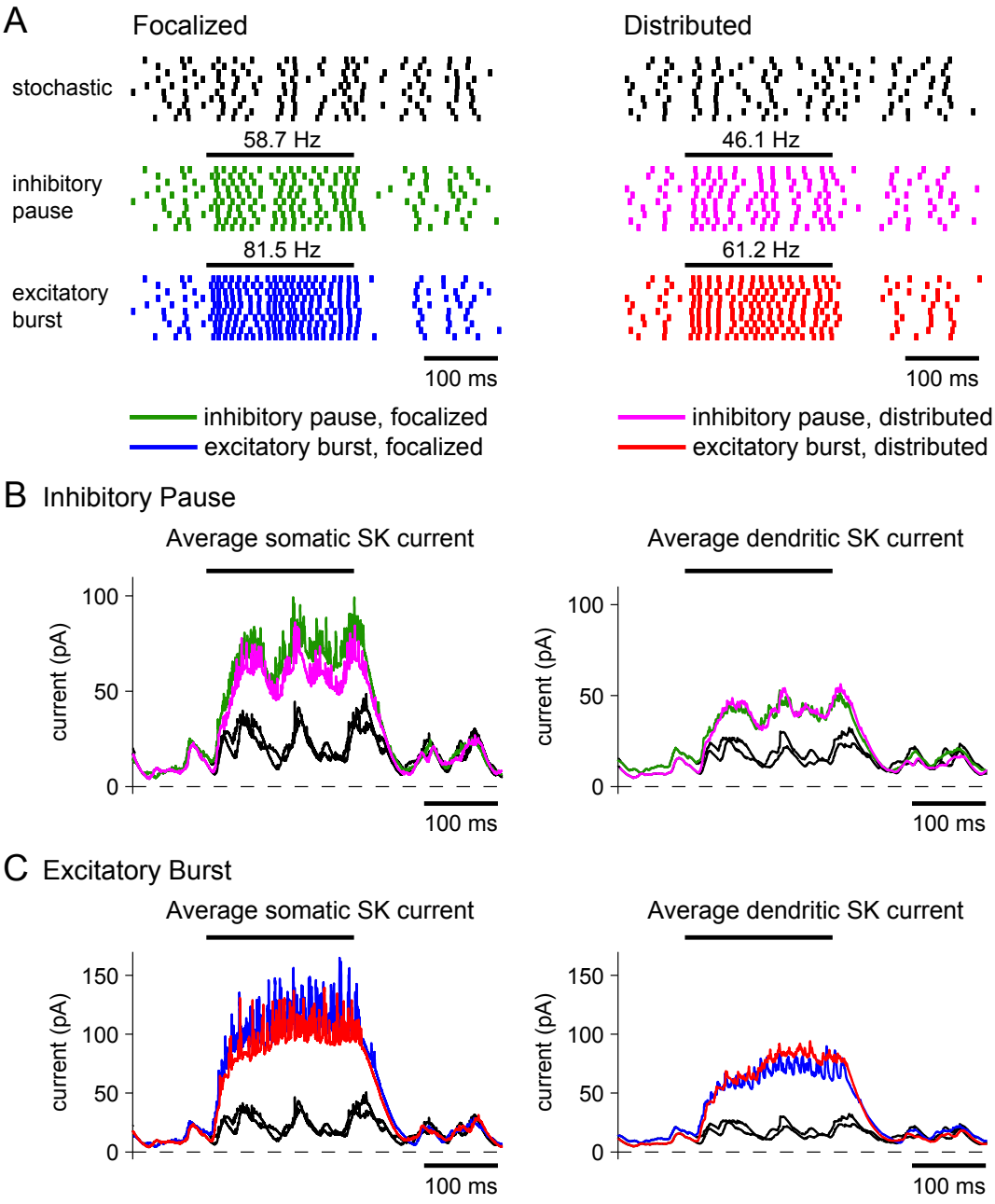

Figure 26: Response to an inhibitory input pause or excitatory input burst for focalized or distributed input in the model. A) A 50% decrease in the inhibitory input rate approximately doubled the output spike rate of the model. This increase was slightly higher for focalized inputs, which is likely due to greater excitation on the soma in the focalized case. A 100% increase in the excitatory input rate had an effect similar to that of an inhibitory pause but drove the model to spike at even higher frequencies. B) During the inhibitory pause, the magnitude of the SK was larger due to increased spiking. C) The effect of an excitatory burst was similar to that of an inhibitory pause with the magnitude of the SK current driven even higher by the higher spike rate. The effect for both input conditions was somewhat stronger for focalized than for distributed inputs due to the higher achieved spike rate. In all cased, the SK current took about 60 ms to relax back to the control trajectory after the end of the input burst.

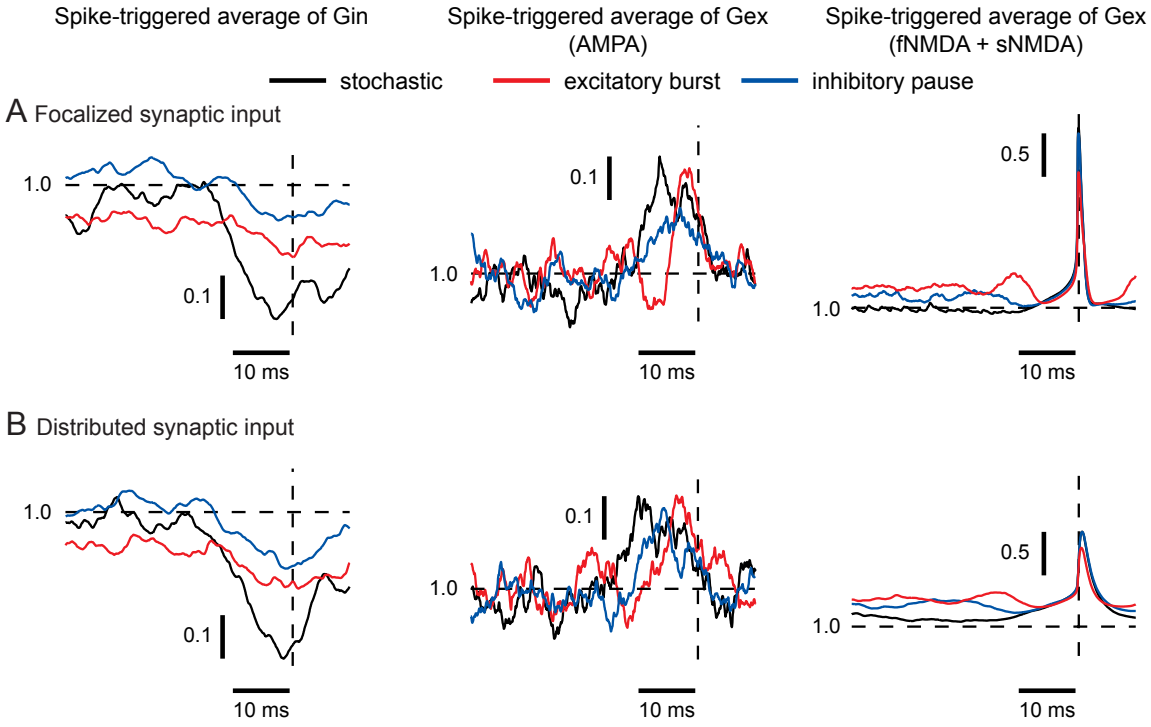

Figure 27: Spiked-triggered averages of inhibitory and excitatory conductance (normalized to the mean conductance value) when purely stochastic synaptic input or patterned input was applied. The vertical dashed line indicates the time of the spike. The STA was computed over all spikes for all trials during the 200 ms excitatory burst (focalized: 188 spikes, distributed: 145 spikes) or inhibitory pause (focalized: 129 spikes, distributed: 100 spikes). In the case of stochastic input, the spike rate was much lower so the STA was computed over all spikes (focalized: 149 spikes, distributed: 123 spikes) in the 5 s long control trial without input transient. All STAs were normalized to the average conductance for each trial (horizontal dashed line). A) In the focalized input condition, the STAs show that both excitation and inhibition could control spike timing when both synaptic excitation and inhibition were applied. There was a transient decrease in inhibition (G_{in}) and transient increase in AMPA conductance preceding each spike. The NMDA conductance also increased preceding a spike, but its voltage-dependence resulted in a steep conductance increase during action potentials. When an excitatory burst (red) or inhibitory pause (blue) was applied, the signal in the STA for G_{in} decreased. The STA for AMPA conductance showed diminished amplitude during inhibitory pauses but a sharper increase during an excitatory burst. The STA for NMDA predominantly reflected the NMDA voltage dependence such that it was much increased during a spike. B) Very similar spike-triggered averages were observed when synaptic input was distributed over the dendritic tree. However, the voltage-dependent increase in NMDA conductance during a spike was decreased, because spike backpropagation into the dendrite was incomplete due to its fast time course, and as a result dendritic NMDA conductance did not show as strong an increase during spikes.

model of a DCN neuron. Our approach allowed us to apply the exact same synaptic conductance patterns used previously in dynamic clamp studies to the computer model either only at the soma to simulate dynamic clamping, or distributed throughout the dendritic tree to simulate natural synaptic input in vivo. While the model was originally tuned to replicated only spontaneous and rebound firing activity under current clamp [233], it could also replicate the neuron's response to complex fluctuating inhibitory and excitatory conductances previously recorded with dynamic clamping [82]. With additive white current noise applied to the soma, the model could also reproduce the millisecond precision in spike times between repeated trials of stimulation.

Our simulations support the premise that dynamic clamping presents a valid approach to probe DCN neurons for their function of synaptic integration with complex input patterns. The observed close match between somatic focalized and distributed synaptic input processing is likely due to the relatively electrotonically compact size of DCN neurons. Because the electrotonic distance for any dendritic input to the soma rarely exceeds 0.2 λ, there is little voltage attenuation between the site of synaptic input and the soma. Attenuation becomes more severe for strong dendritic input transients while the neuron is in a high conductance state [153, 202], and consequently the largest departure between distributed dendritic and somatic input was observed in the case of intense AMPA excitatory input bursts.

We also developed a set of benchmark measurements that can be used to assess differences in synaptic responses to focalized or distributed synaptic input. These measurements include important variables such as spike rate, spike time precision, and spike triggering conductances that are frequently used in analyzing dynamic clamp data [42, 70, 83, 236]. In our DCN neuron model, there were only minor differences in spike pattern generation between focalized or distributed input in the model, even when strong inhibitory bursts and pauses or excitatory bursts were applied. The relationships between spike-time precision and spike frequency with different input levels and input synchronicity were also very similar. The lack of differences in responses to focalized or distributed synaptic inputs suggests that deep cerebellar nucleus neurons essentially do not rely on their morphology for input processing. In fact, a six compartment and a one compartment model also showed the same

results. Different cell types, and in particular larger types of neurons, will likely show more pronounced local dendritic processing and hence less similar results for focal somatic and distributed dendritic synaptic input.

The stimulus designs and benchmark analysis methods developed in this study provide a general toolkit that will allow a detailed comparison between focal and distributed conductance distributions in all cell types for which detailed compartmental models are available. The model can then be used to generate experimentally testable predictions about how a neuron's response is mediated by the interaction between external synaptic conductances and intrinsic membrane conductances. We addressed for the first time the question of how a calcium-activated potassium (SK) current may interact with GABAergic synaptic inhibition to control DCN output spiking. Our computer simulations predicted that the observed effects on the synaptic transfer function could be explained with two distinct mechanisms: an increased responsiveness to large input transients due to blocking the mAHP, and a decrease in responsiveness to smaller input transients due to an overall hyperpolarizing shift. The question of whether intrinsic downregulation of SK conductance would also result in an overall reduction in excitability by a tonic increase in outward bias remains to be addressed. However, many if not all cell types show homeostatic plasticity of spike rates such that regulatory processes counteract a tonic increase in spike rate [198, 242] and can be mediated by the adaptive regulation of a voltage-insensitive K+ current [30]. In fact, the rapid onset of reduced excitability with apamin-induced bursting may present just a exaggerated form of such an otherwise more gradual process.

In this study, we showed the systematic substitution of an intrinsic current with dynamic clamp after pharmacological block. The dynamic clamp can also be used to subtract the electrical effect of an intrinsic current simply by reversing the sign of the conductance so that a current of the opposite sign is applied. Note, that the parameters of the model describing the SK current in this study had to be adjusted for each cell. This step provides some additional insight to the intrinsic biological variability between cells. As dynamic clamping is becoming more widely used in many cell types, the modeling approach developed here will likely result in valuable insights regarding the specific limitations of this technique for

different cell types and morphologies.

3.4.2 Additive somatic current noise can simulate variability in a neuron's response to repeated presentations of the same stimulus

Variability in neuronal responses to repeated identical stimuli is partly due to subthreshold membrane voltage fluctuations, which underlie the phenomena of "spontaneous spikes" for subthreshold inputs and "missing" spikes for suprathreshold inputs [219]. In fact, many dendritic computations occur within the subthreshold regime. In real neurons, these fluctuations are mediated through changes in the probability of stochastic transitions between conducting and non-conducting states of ion channels in the cell membrane [111]. In our neuron model, deterministic Hodgkin-Huxley type equations were used to simulate homogeneous populations of channel types in each compartment rather than single channels so subthreshold fluctuations due to channel noise were not observed. In our simulations as well as our published dynamic clamp experiments [82, 83], there is also no synaptic noise due to variability in the number of transmitter molecules, availability of receptors, or spontaneous release of vesicles since we used deterministic input conductance waveforms. To reproduce subthreshold fluctuations in the membrane potential, we added a white current noise, $\xi(t)$, to the soma of the model as follows:

$$C_m \frac{dV_m}{dt} = -\sum \left\{ g_i(t)(V_m - E_i) \right\} + \xi_V(t) \tag{13}$$

$$\tag{14}$$

We matched the amplitude of the voltage fluctuations observed in slice recordings by setting the standard deviation of the noise to a specific value. The good match we observed between spike variability in slice recordings and in the model using identical synaptic conductance patterns indicates that for DCN neurons a voltage-independent somatic current noise adequately reflects the influence of channel noise on synaptic responses.

3.4.3 Applying this approach to other neuronal cell types

While our results show that a membrane conductance of electrotonically compact neurons may be applied equally well at the soma or in a distributed fashion, this similarity will likely break down for large cell types with extended dendrites such as cortical pyramidal neurons. In such cells, local dendritic processing such as amplification through dendritic voltage-gated sodium and calcium channels or regenerative events [81,101] can not be adequately recreated with dynamic clamp inputs to the soma. To replicate this study for other cell types, a model must be developed for a typical morphology of that cell type, the channels known to exist in that cell type, as well as the distribution of those channels throughout the cell. Since some, or even all, of these data may not be available from the literature, replicating this approach for other cell types may not be a trivial undertaking. The simulation scripts we used here are downloadable from the ModelDB (http://senselab.med.yale.edu/modeldb/) database, and can be adapted to other neural morphologies that are also freely downloadable from the same database.

In reality, fluctuations in membrane voltage are both activity and voltage-dependent since they depend on both the kinetics as well as the open probability of ion channels. In a model of neurons in the entorhinal cortex, voltage-independent noise was unable to reproduce spike-clustering that arises in a stochastic model due to enhanced responses to weak period stimuli [261]. Channel noise has important effects on neural dynamics by altering the spike threshold, interspike interval statistics, and the amount of stochastic resonance. Furthermore, for other neuron types and morphologies, our approach of adding noise at the whole cell level rather than at the level of ion channels may not be accurate. In a modeling study comparing five morphologically distinct neuronal cell types containing identical densities of stochastic ion channels, the amplitude of V_m fluctuations differed between cell types and depended on the subcellular location of the ion channels. This suggests that in dendritic neurons, spike output may be a probabilistic function of patterns of synaptic input to dendrites due to consequences of stochastic channel gating [40].

The standard method for simulating stochastic ion channels are Markov chain models that assume that the state of an ion channel is described by a discrete-state, continuous-time

Markov chain. Each state in the Markov chain represents a conducting or non-conducting configuration of the ion channel. While these models are widely used, they are also computationally intensive and unsuited to real-time protocols. There are a number of other options for introducing stochasticity into Hodgkin-Huxley type channel kinetics to simulate this behavior. In a study comparing single-compartment neuron models based on linearized approximations to the Hodgkin-Huxley equations with an additive white current noise, the magnitude of computed voltage noise was within 0.1 mV for all voltage ranges tested when compared to Monte Carlo simulations of Markov channels. The error was less than 8% for subthreshold voltages [230]. In another study, the interspike interval distribution generated by a Markov chain model showed remarkable agreement with the distribution generated by Hodgkin-Huxley equations with current noise [209] .

Fox and Lu were the first to attempt simpler models that used stochastic differential equations (SDE) based on Hodgkin-Huxley equations [77, 78]. Since an ion channel's configuration is determined by the states of its subunits, they proposed a method by which noise is added to the equations that describe the fraction of open subunits:

$$\frac{dx}{dt} = \alpha_x(1-x) - \beta_x x + \xi_x(t) \tag{15}$$

However, the quantity that actually influences the membrane potential is the fraction of open channels and the stochastic transitions of individual channels occurs with different statistics than the transitions of the aggregated subunits.

Fox and Lu also proposed a channel-based approach, which adds noise to the proportion of channels in a particular state, x_i, which is not a measure of probability when dealing with a finite number of channels. The conductance is determined from the proportion of open channels, where A is the deterministic transition matrix describing how the probability of a channel having i open subunits changes and S is the square root of a diffusion matrix that depends on the state variable and voltage-dependent transition rates.

$$\frac{dx}{dt} = Ax + S\xi \tag{16}$$

This approach is computationally expensive, taking about 25 times as much time as a subunit model, because matrix square roots must be calculated. However, the computation time does not scale with the number of channels and is still faster than the Monte Carlo method. Another option is to add noise directly to the fraction of open channels, given by m^3h and n^4 in the Hodgkin-Huxley model. The most direct approach is to add zero-mean noise to these values:

$$C_m \frac{dV_m}{dt} = -\bar{g}_{NaF}(m^3h + \xi_{Na}(t))(V_m - E_{Na}) + ... \tag{17}$$

It has been found that $\xi(t)$ in this case is best represented as a sum of independent Ornstein-Uhlenbeck processes (Gaussian colored noise) in order to approximate the Markov chain description of channel kinetics. For other neuronal cell types, a different approach than that used here may be more appropriate. The choice of how to add channel noise can affect the intensity of voltage fluctuations, resulting firing rates, and the variability in spike times [91, 92].

3.5 Acknowledgments

The work in this Aim was performed in the lab of Dieter Jaeger at Emory University. The original dynamic clamp experiments were conducted by Volker Gauck [82, 83]. The multicompartment DCN model was developed by Dieter Jaeger and Volker Steuber [233]. Later dynamic clamp experiments repeating the original work and investigating the role of the SK channel were performed by Steven Feng with preliminary results published in 2008 [74]. I conducted all the simulations and corresponding data analysis presented in this section.

CHAPTER IV

REAL-TIME EXPERIMENT INTERFACE FOR CLOSED-LOOP BIOLOGICAL EXPERIMENTS

The Real-time Experiment Interface (RTXI) is an open source software platform for hard real-time data acquisition and closed-loop control protocols in biological experiments. It is the result of combining three previous efforts in creating such a system:

1. RTLab: Real-Time Linux Lab is a general-purpose control system used primarily for tissue-level excitable system experiments (NSF grant DBI-0096596; PI: David J. Christini).

2. RTLDC: Realtime Linux Dynamic Controller is an open-source implementation of the dynamic clamp, which is a methodology that integrates the real-time simulation of ion-channel kinetics (or entire models of excitable cells, such as neurons) with intracellular electrophysiological experiments (NSF grant BES-0085177; PI: John A. White).

3. MRCI: Model Reference Current Injection system is also an open-source dynamic-clamp system (NSF grant DBI-9987074; PI: Robert Butera).

RTXI is currently used extensively for two experimental techniques: dynamic clamp and closed-loop stimulation pattern control in neural and cardiac single cell electrophysiology. The power and flexibility of RTXI has made it possible for users to implement complex custom protocols in a variety of experiment types. Examples include the investigation of the contribution of specific ion channels or synaptic receptors to spiking and bursting activity in a variety of neuronal cell types, factors affecting the synchronization of connected neurons, and the effect of network topology and intrinsic neuronal properties on population activity in a hybrid network.

Currently, it is difficult to compare the differences between currently available dynamic clamp systems and the results of dynamic clamp experiments implemented using different platforms. Metrics for real-time performance are not always reported in the literature, in part because there are few standard benchmarks. Previous work has shown that the speed and real-time performance of dynamic clamp systems can have a significant effect on experimental results by affecting how accurately the numerical models can be integrated [24]. In fact, the convergence of spike shapes using different integration methods in real-time only occurred at sampling rates of at least 50 kHz. For the Euler method, which is commonly used, accurate spike shapes were only produced at sampling rates of at least 30 kHz [167]. Intensive graphics that must be updated in real-time as well as disk and network usage can significantly affect these measures [36].

Furthermore, most existing dynamic clamp systems contain a limited set of template models for specifying artificial ion channel and synapses, have limited mechanisms by which users can create new custom models or experimental protocols, and require expensive specialized hardware. Users usually must accept a trade-off between ease-of-use and flexibility. I developed improvements to the original RTXI architecture and new userspace features to support typical analyses that are performed during model development or on experimental data obtained under dynamic clamp as well as reporting of important real-time performance benchmarks. These modules can be shared between RTXI users so that experiments can be replicated exactly and compared.

4.1 RTXI architecture

RTXI was originally designed to operate with two threads: a real-time (RT) thread that runs at the highest priority allowed by the Linux operating system and a user interface (UI) thread that is responsible for handling user input and graphics (Figure 28). The real-time thread "wakes" on each clock cycle and executes any operational overhead associated with the DAQ card, system functions, and handling real-time events. It then executes real-time code associated with any user-loaded modules. The RT thread and UI thread run in the same process address space and can share data in order to process user-triggered

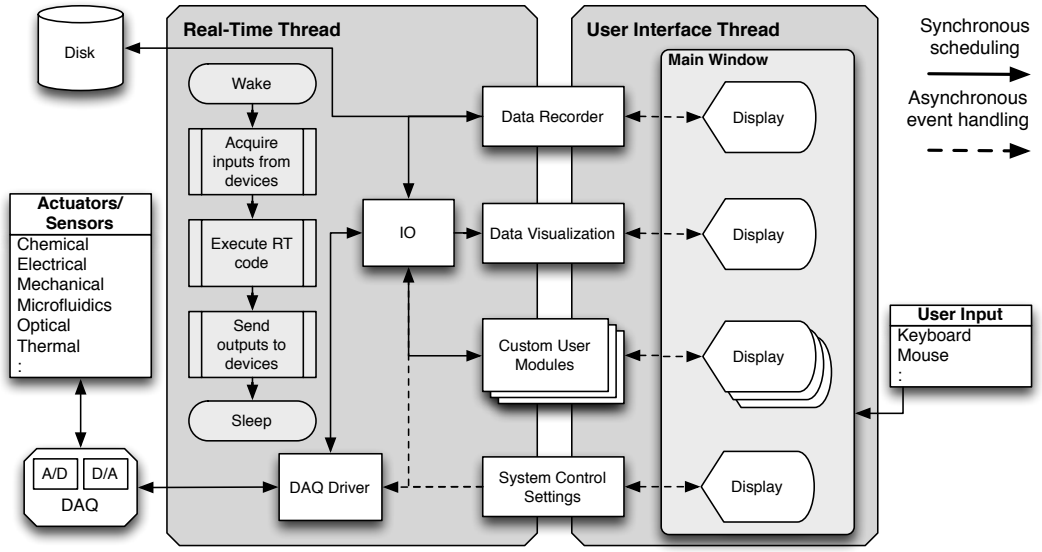

Figure 28: RTXI uses a two-thread approach in which a real-time thread executes all real-time tasks while a separate non-real-time thread handles asynchronous events related to user input and the GUI. The RT thread wakes on every cycle to execute core real-time instructions, such as DAQ operations, as well as any real-time instructions that are part of user-loaded modules. System and custom user modules span the RT and UI threads to provide GUI-based access to DAQ signals and module-specific internal states and variables.

events and update the graphics. All RTXI system features and custom user functionality are implemented as modules. Modules contain function-specific code that can be used in combinations to build custom workflows, experimental protocols, and interfaces, thereby eliminating the need to code all aspects of each experiment protocol from scratch. Often, users will have multiple modules working in parallel during a single RTXI session.

RTXI modules communicate with each other within the RTXI workspace by a system of *signals and slots* and event handling. For example, all data acquired through individual channels on a data acquisition (DAQ) card are preserved as distinct signal streams that can be passed to other modules that implement real-time analyses such as event detection, digital filters, etc. Similarly, all user modules can accept input signals and generate output signals that can be connected to other modules or to a DAQ card to produce external analog or digital signals. An important advantage of this modular architecture is the ease and flexibility the user has in changing modules and modifying module parameters. Each module is implemented as a separate C++ class that is compiled as a shared object library

(*.so) outside of the RTXI source code. Only a minimal set of modules is initially loaded to give users access to basic system features. This minimizes the overhead of running RTXI and maximizes the real-time performance. Additional modules may be loaded, connected to each other, and activated with immediate real-time response. Other popular platforms for real-time closed-loop data acquisition may require the user to recompile the program or re-download it onto a dedicated real-time processor.

The original design of RTXI provided a basic userspace skeleton C++ class, DefaultGUIModel, that created a minimal GUI containing text boxes for editing parameter values and buttons for activating/deactivating a module. The DefaultGUIModel class is derived from other RTXI base classes and handles all the details of real-time execution, event-handling, and implementation of RTXI's signals-and-slots system for sharing data between modules (Fig. 29). Users may safely write custom modules derived from the DefaultGUIModel class without violating hard real-time constraints. However, to create custom GUIs and more advanced protocols integrated with RTXI system features, such as the Data Recorder for streaming data to disk, users had to write modules that spanned both the RT and UI threads and extended multiple complex classes. Without programming experience, users could easily break real-time without knowing it. I reimplemented the DefaultGUIModel and Workspace::Instance classes to make it easier for users to write modules containing custom user interfaces and experimental protocols. DefaultGUIModel is now a more powerful class that directly supports custom UIs and contains additional thread-safe APIs for accessing and setting system parameters from the user space.

I also updated RTXI with additional features to make installation and module development easier for new users. RTXI is now available as a Live CD based on long-term support versions of Ubuntu. These CD's can be used to boot any computer into a working real-time Linux OS with RTXI already installed with DAQ support. Users can run experiments using the live session without actually installing Linux or can install a complete system directly from the CD without compiling a Linux kernel from scratch. If the live CD image is loaded on to a USB flash drive with persistent memory, users can also develop modules and save them on the flash drive, making their experiments portable across machines. RTXI also

now supports additional open-source libraries out of the box: 1) Qwt, a Qt-based widget library for scientific plotting (http://qwt.sourceforge.net/), 2) GNU GSL, a numeric library for scientific computing (http://www.gnu.org/software/gsl/), and 3) NLopt, a library for nonlinear optimization (http://ab-initio.mit.edu/wiki/index.php/NLopt). Finally, I added an additional workflow to RTXI for implementing user modules. Instead of writing custom C++ classes or using the original MRCI SML-based scripting language, users can also compile ChannelML descriptions of ion channel models directly into RTXI modules. ChannelML is part of the NeuroML (http://www.neuroml.org/) project and uses an XML based syntax and is quickly becoming a standardized syntax for describing the dynamics of model components in a simulator independent, machine readable way. In collaboration with the neuroConstruct project, this format is also used as an intermediate for porting models across simulation platforms and is seeing increased adoption as a standard for publishing ion channel models. Both the MRCI and ChannelML workflows generate modules based on the DefaultGUIModel class, allowing parameter changes on-the-fly and integration with other RTXI features.

RTXI was initially designed to enable hard real-time feedback control of experiments involving continuous (gap-free) protocols. This architecture resulted in very fast first-in-first-out processing of multiple signal streams involving conversion between digital and analog signals, data visualization in the digital oscilloscope, and saving the data to disk. I extended RTXI's architecture to accommodate episodic protocols that allow application of the same stimulus in repeated trials and will display the data and statistics in user-defined ways. This feature is implemented as a wrapper module around any other RTXI user module and has the ability to control the target module's real-time execution and modify parameter settings. Users can now construct protocols around any target RTXI module and avoid explicitly embedding this layer into each module.

This more flexible architecture segregates core RTXI features, written at the level of DefaultGUIModel, from optional features and custom user modules, which are derived from DefaultGUIModel. The new DefaultGUIModel forms the basis for new tools that make RTXI a more fully-featured data acquisition system similar to PClamp and other

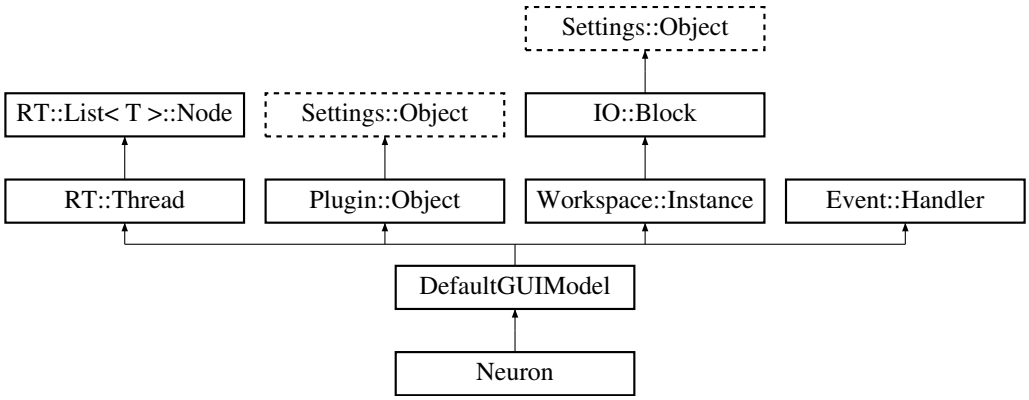

Figure 29: RTXI user modules, such as Neuron, are derived from a skeleton class, DefaultGUIModel, that automatically handles all real-time execution, event-handling, and implementation of RTXI's signals-and-slots system for sharing data between modules.

commercial products. For example, RTXI now includes standard FIR and analog filters, function (signal) generators, and modules that can "play back" previously recorded data from different formats as if it was acquired in real-time. This last feature is useful for testing an debugging online algorithms using actual real-time execution without committing the resources and time required for setting up an actual experiment. Additional features in development include suites for various electrophysiology experiments: measurement and monitoring of electrode resistance, graphical editors for common user protocols (such as voltage clamp), and a desktop display of recordings alongside images acquired from CCD cameras.

4.2 Real-time performance benchmarks

I developed a module for RTXI to track the actual real-time period and its jitter and the actual computational time required for all loaded modules. It also tracks the worst case time step, which was previously shown to define the upper error bound for dynamic clamp accuracy [24]. RTXI is based on the Real-Time Application Interface (RTAI). A feature of RTAI is that it anticipates the next cycle so that the real-time period is generally less than the nominal period. However, it guarantees that no cycles are longer than the nominal period. If the computation time required for all real-time execution does approach the nominal period, RTXI suspends the thread responsible for the graphical user interface until

more resources are available again. This is an important indicator to the user of when they are approaching the technical limits of their system.

Histograms of the actual real-time periods used in RTXI for different sampling rates is shown in Fig. 30. A normal level of usage consisted of two Hodgkin-Huxley model neurons that were reciprocally coupled with spike-triggered synapses, four traces plotted in the digital oscilloscope, one active input and output analog channel on the data acquisition board, and 6 channels streamed to the disk in real-time. A heavy level of usage was simulated as twice as many modules as the normal level along with additional modules generating white noise and computing conductance waveforms in real-time. At 1 kHz, a "heavy" level of usage resulted in essentially the same histogram but this is a much lower sampling rate than what it is typically used in dynamic clamp. At 10 kHz (a commonly recommended rate) and 50 kHz the system does show a broader spread of real-time periods around the mean. These data show that RTXI can operate reliably at 50 kHz with 1 μs of jitter. In a simulation study of different integration methods (CVODE, Euler, Markov matrix method) for dynamic clamp, it was found that at 50 kHz all the methods resulted in virtually identical spike shapes [167].

Other intuitive metrics can be based on the performance of the dynamic clamp system in integrating the Hodgkin-Huxley neuron, eg. the maximum sampling rate that the system can integrate a single Hodgkin-Huxley neuron and the number of model neurons that can be solved in real-time at different sampling rates. Modules were developed to determine each of these limits by adding neuron models or increasing the sampling rate until the computational time required approached the nominal period. For a computer containing a 2.53 GHz Intel Core 2 Duo processor, a single Hodgkin-Huxley model with the real-time digital oscilloscope could be integrated at 110 kHz. At 10 kHz, 115 Hodgkin-Huxley neurons, or equivalently 460 differential equations can be solved This decreases to 40 model neurons at 40 kHz and 15 model neurons at 50 kHz.

Since the number of RTXI users is expected to see steady growth, these standard performance benchmarks will complement the software's open source transparency to make it easier to evaluate dynamic clamp data obtained from systems that may use different

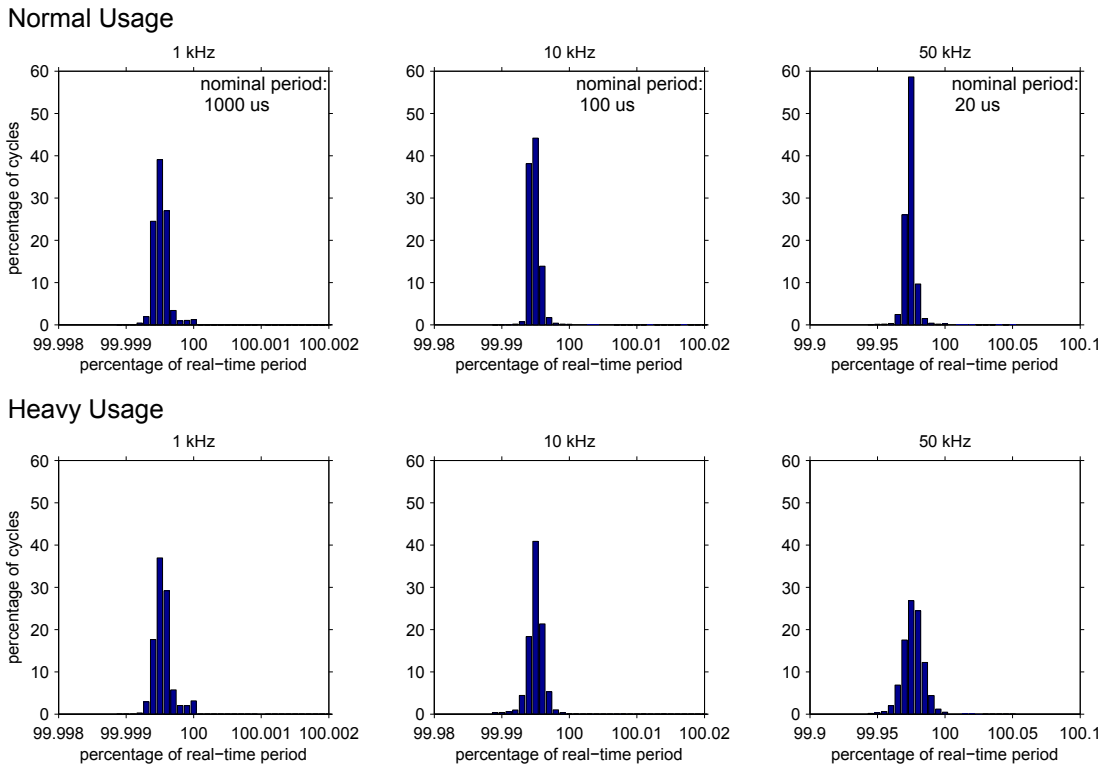

Figure 30: RTXI: Histograms of actual real-time periods show a wider range of real-time periods at high sampling rates. The hard real-time architecture guarantees a worst case time step that is less than or equal to the nominal system period.

hardware and numerical techniques. In particular, users will be able to evaluate whether their real-time performance is sufficient to accurately model the temporal dynamics of the processes they are interested in.

4.3 Online experimental data analysis and visualization

There are several types of data visualization that are commonly used to analyze dynamic clamp results. These include raster plots, which capture events, such as spike times, over a set of repeated stimulation trials. The trials are stimulus-aligned and when visualized in real-time can provide useful feedback about the typical response pattern of a neuron to an input, which can not be easily seen on a standard oscilloscope or chart recorder.

An example of raster plot generated in real-time in RTXI is shown in Fig. 31. In this module, a fixed conductance waveform was loaded from an external ASCII file. This waveform was applied to a model neuron simulated within RTXI and the timing of each

spike was determined by detecting a positive threshold crossing at -20 mV. In the raster plot, the first ten trials are open loop (the dynamic clamp is not active) and the neuron spikes regularly. The reversal potential for this example is set to -80 mV so that the conductance has an inhibitory effect. When the dynamic clamp is turned on starting at trial 11, the neuron spikes irregularly with reliable timing for each repeated application of the artificial conductance waveform.

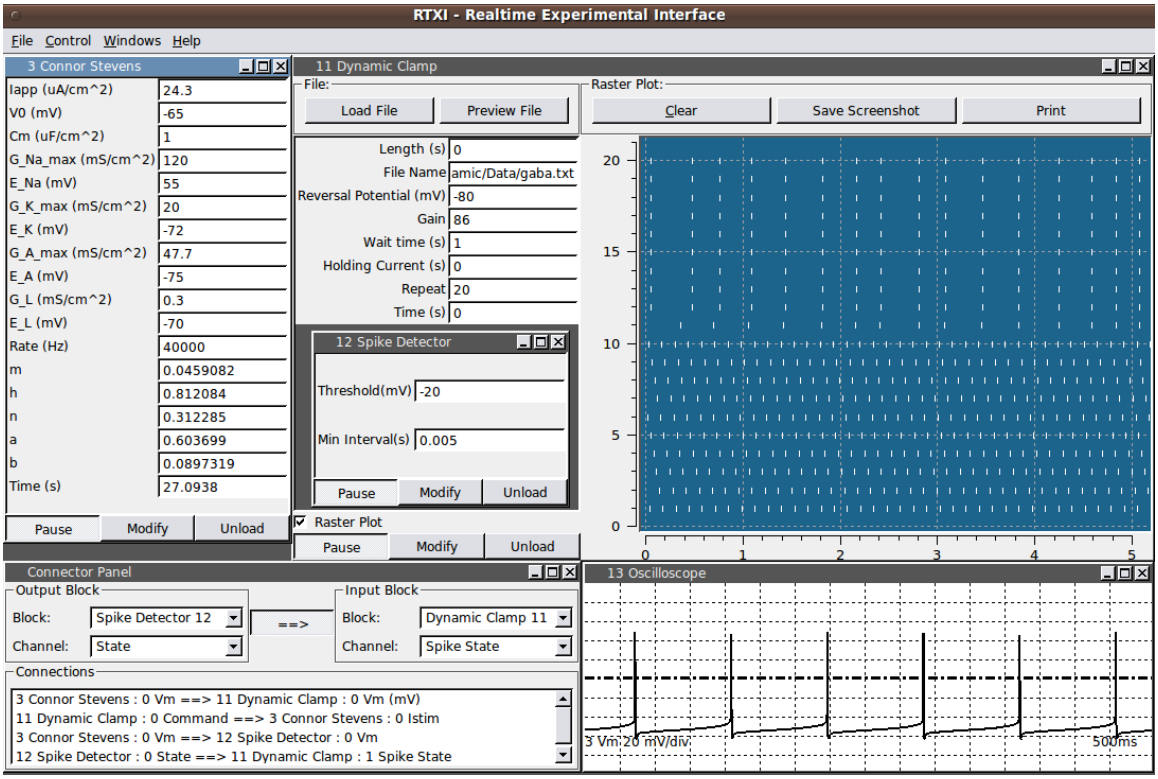

Figure 31: RTXI: Online raster plot of neuron's response to repeated dynamic clamp stimuli. The dynamic clamp is turned on at trial 11 and the neuron's spiking activity changes from spontaneous regular spiking to irregular spiking controlled by artificial conductance.

In dynamic clamp experiments, the spike-triggered conductance shows what feature in the input actually triggers spikes and can be used to determine the optimal timing and kinetics of such input as well as determine the balance between excitation and inhibition. This metric was described in Chapter 3 to explain the characteristics of synaptic integration in deep cerebellar neurons and was used as a metric to validate a biophysical model of that cell type. In this module, a circular buffer is used to continuously collect data. When a spike or other event is detected, a running average of the spike-triggered input is computed

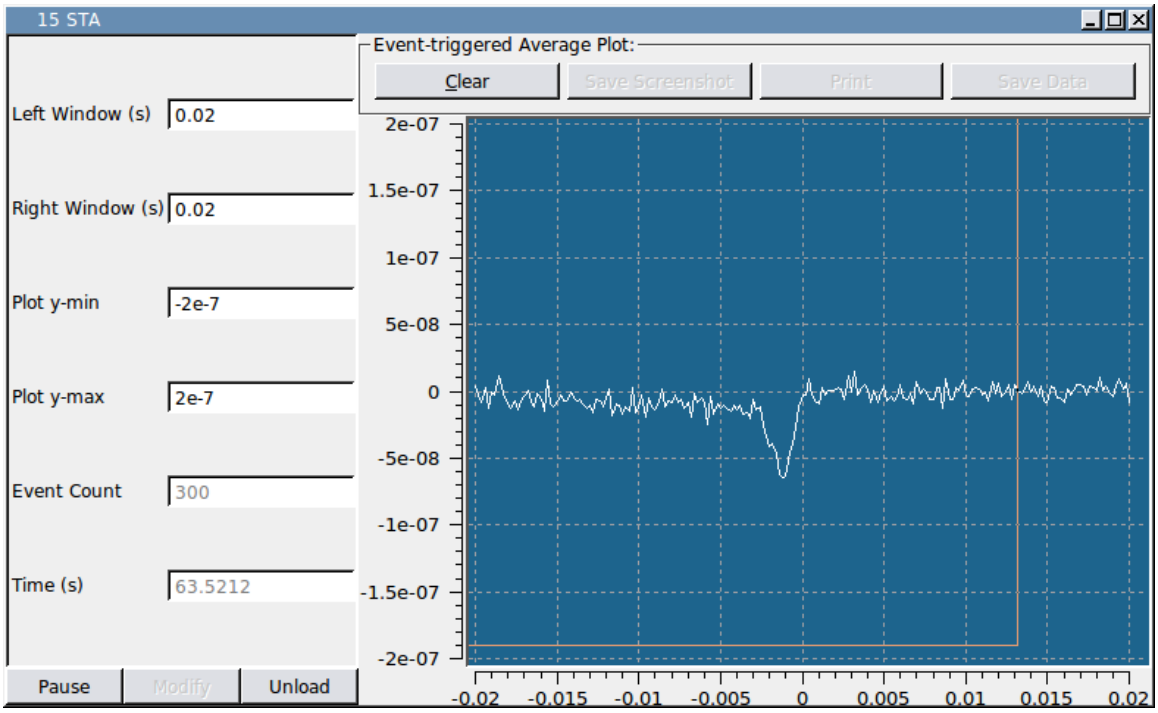

Figure 32: RTXI: Online spike-triggered average of input conductance for dynamic clamp experiments in Fig. 31.

and updated in real-time. For the example shown in Fig. 31, we expect that a decrease in the inhibitory input should trigger spikes (Fig. 32). The average of the spike-triggered conductance over 300 spikes shows a transient just before the spike occurs at zero. All other information has been averaged out leaving only the specific feature in the input that is related to spike generation.

4.4 Online optimization of model parameters during dynamic clamp

A common scientific application of the dynamic clamp is one of pharmacological elimination of an ion channel's functional effects, followed by reconstitution of the ion channel via a dynamic clamp. This approach is scientifically powerful, as it allows one to go beyond mere voltage-clamp characterizations to actual functional evaluation of the role of an ion channel. If the model of ion channel is truly valid, then metrics like action potential shape should be comparable before pharmacological block and after dynamic clamp. In general, there are many caveats associated with obtaining gating parameters from voltage-clamp data (e.g., specificity of pharmacological blockers), and in practice using these parameters

directly in a membrane-level model is often imperfect. Furthermore, in some systems direct voltage clamp measurements may not be possible. The net result is that voltage-clamp measurements (or literature-based estimates) are followed by further tweaking of the model parameters to obtain an action potential that is sufficiently similar to the control action potential. A rigorous online method for tuning model parameters can supplement previously described offline model-fitting techniques.

I developed an RTXI module to implement the following procedure:

1. Collect a reference waveform (eg. an action potential captured by the spike-triggered average module previously described).
2. The user specifies an ion channel model and indicates which parameters are "free" and subject to modification.
3. The user switches from a control solution to a test solution, where the ion channel is putatively blocked.
4. Activate the dynamic clamp running the ion channel model with a given initial set of parameters.
5. Measure each action potential, and using an optimization method, modify the free parameters to minimize the error between the recorded waveform and the reference waveforms from step 1.

This module used the Simplex optimization algorithm since it does not require computing the derivatives of the system. This method works by first identifying a region in parameter space that has one dimension more than the number of free parameters. For example, if two parameters are to be determined, the simplex is a triangle in a 3-D space. This region is then geometrically transformed by reflection, expansion, or contraction to converge onto the final solution. The goal of this problem is to minimize a cost function that is the sum of the squared error between the target waveform and the result of applying a particular parameter set.

The module was tested using a Connor-Stevens model neuron simulated within RTXI. This model contains a fast sodium and potassium conductance to generate the spike as well

as a slower A-type potassium current. The A-type current is active during the interspike interval and serves to lower the spike rate. To simulate an experiment in which this ion channel is blocked, its conductance density was set to zero in the model. The optimization module contained a model of the A-type potassium conductance and produced a current that was connected back to the neuron model. Two parameters were left free for the optimization module: the maximal conductance density and the reversal potential. These were initialized at 55 mS/cm^2 and -80 mV and the initial spike waveform can be seen in the top panel of Fig. 33. The parameter values and spike shape after fifty iterations are shown in the bottom panel (the difference between the "Event Count" fields minus three evaluations for initializing the simplex). The true values for these parameters are 47.7 mS/cm^2 and -75 mV.

While the simplex method seems to converge very quickly in this example, there were a number of complications in the procedure. The geometric transforms applied by the algorithm often generated parameter sets that did not produce spiking or were out of the physiological range. The only solution was to manually advance the protocol to compute a flat spike-triggered average and the corresponding mean-squared error. In many cases, we also had to restart the model neuron. This performance could be improved by adding inequality constrains to restrict the parameter sets that were generated by the algorithm. In experiments with real neurons, these constraints would prevent the user from accidentally injecting arbitrarily large currents that could damage the cell.

The simplex method has the disadvantage of being very inefficient near the optimum solution and is generally slower than conjugate gradient methods which are popular for this application. However, a cost function consisting of the mean squared error between the spikes does not necessarily have a smooth gradient in this parameter space. The simplex method is more robust to random cost functions. This module is also easily modified to include other features in the cost function. By widening the window, this module could be used to fit two consecutive action potentials, a method that has been shown to successfully fit spike rate as well as spike shape. Other events besides the occurrence of a spike could also be used. For example, the latency to the first spike after a stimulus is sometimes used

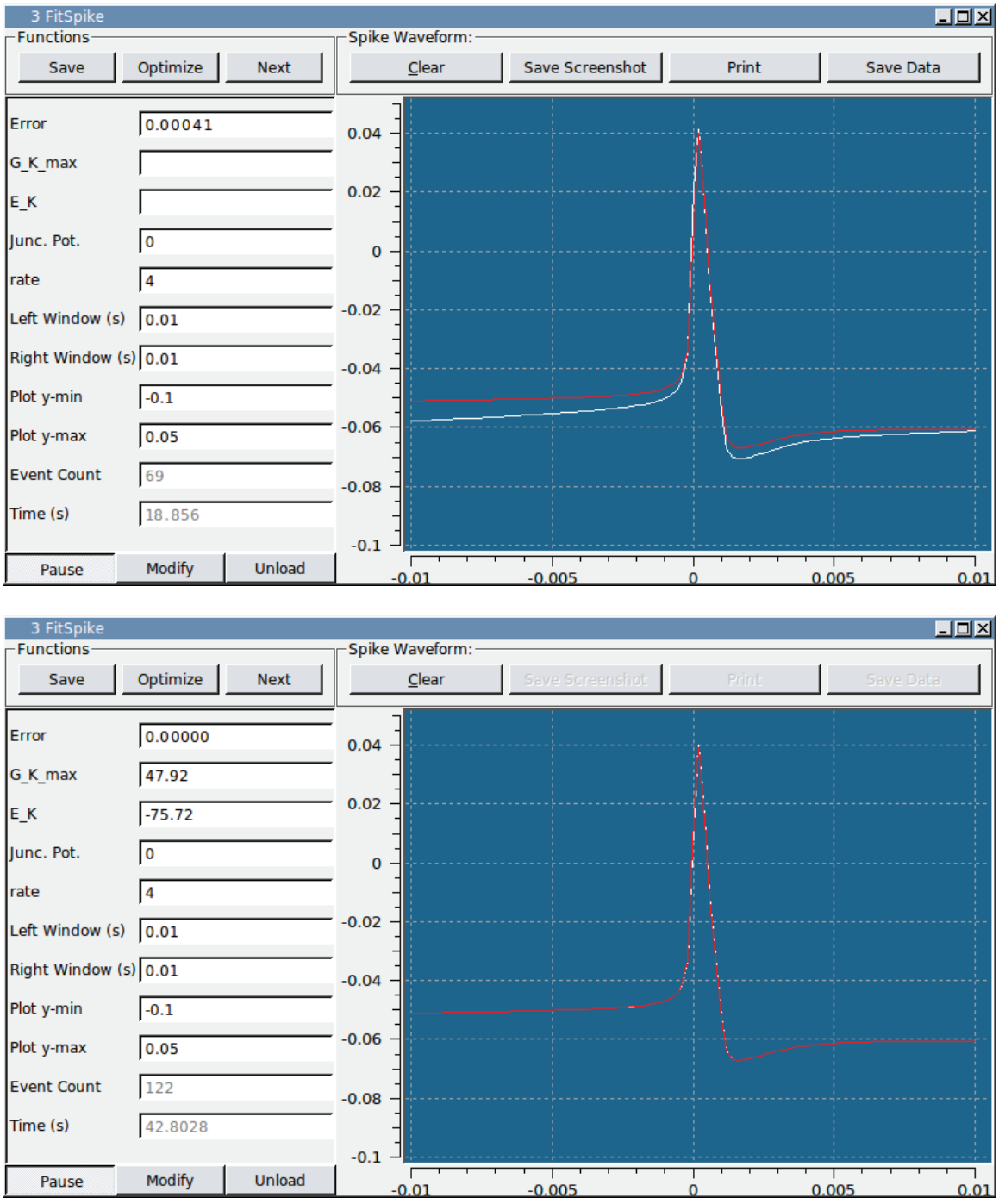

Figure 33: RTXI: Online optimization module to reproduce spike shape, before and after optimization. The target spike waveform is shown in red after the user has saved it. The spike based on the initial parameters is shown in white and is continuously updated as new parameter values are tried.

as a target feature. In this case, the window of time to capture would include the stimulus and some time after the spike. The cost function can be any arbitrary equation based on the voltage trace.

The advantage of an online optimization approach is that parameter values may be found that explain not only the biophysical properties of the channel, but also the functional behavior of a specific cell, without requiring any knowledge about the nonlinear interactions with other currents. Modeling kinetics from voltage-clamp protocols has the potential of being very precise, but does not guarantee that the estimated parameters do, in fact, explain the observed dynamics for that very same cell. Furthermore, performing this procedure across a population of cells would result in a distribution of parameter values that capture physiological variability. This online optimization approach could be used for not just action potentials, but other biological waveforms (such as Ca^{2+} fluorescence), as well, where the time-varying dynamics can be measured and modeled.

4.5 Acknowledgments

RTXI was originally designed by Jonathan Bettencourt in John White's lab at Boston University and details about the design decisions are available in his Master's thesis. MRCI was developed by Ivan Raikov in Robert Butera's lab. I integrated MRCI into RTXI where it is now known as the DYNAMO scripting language and also serves as the intermediary for translating ChannelML models into RTXI objects. I developed all the new RTXI features described in this section as well as the Live CD disk image and user manual available on the project's website (http://www.rtxi.org). RTXI has one other contributor, Francis Ortega in David Christini's lab who is developing modules for patch clamp experiments and cardiac electrophysiology. Other labs that use RTXI have developed their own custom modules and their publications and corresponding source code are available on the website as well.

CHAPTER V

THE UNSCENTED KALMAN FILTER FOR REAL-TIME STATE AND PARAMETER ESTIMATION IN NEURONS

The dynamic clamp technique utilizes mathematical models that have contributed much to our quantitative understanding of single neuron dynamics. The development of these models face technical challenges that are common to the simulation of most natural phenomena, which are typically very nonlinear and allow limited experimental measurements. Furthermore, measurements that can be made are usually contaminated by noise that can arise from sources within the system or from the equipment. When developing a conductance-based neuron model as described before, the only experimentally observable quantity is the membrane voltage while there are multiple underlying states and parameters that have to be determined. Ideally, the values of all parameters would be determined from experimental data but this presents several problems. Not all parameters can be estimated with good accuracy especially for small perturbations and high levels of noise. Furthermore, these parameters are often estimated from data collected from a set of different neurons of a single type. Often, a single representative spike shape is selected from this diverse data set or the average of quantified features across the dataset is used. Different neurons of the same type can differ widely in their composition of ion channels and response to input.

Traditional voltage-based model-fitting methods seek to minimize a cost or distance function that corresponds to error measures (usually computed in a global least squares sense) between the model's behavior and real neuron's behavior. The terms of the cost function may include features such as spike shape [235, 249, 258], features such as spike amplitude and after-hyperpolarization depth [68, 96], burst and firing pattern properties [198,239,241], and even the rate of change of V_m along the system's trajectory (phase plane trajectories) [1, 246]. However, neuron models are highly nonlinear dynamical systems and a major challenge in these approaches is that the cost function may become so complex that

standard numerical optimization methods fail [69, 249]. In light of these issues, the general problem of parameter estimation and system identification in computational neuroscience has been primarily focused on automated parameter search methods such as evolutionary algorithms [1, 85], brute force systematic searches [25, 198], and simulated annealing. These methods may be highly dependent on initialization parameters and can often converge onto local minima without exploring a broad range of parameters. Furthermore, there are additional inputs to the automated algorithms that still require user input. For example, the weights of each term in the error function must be chosen and there are not always rigorous methods for making these decisions.

All these methods apply a global minimization constraint on the parameter estimation process in order to capture the time-varying dynamics of the system. An alternative approach that guarantees continuity in time is a recursive technique that uses the model's current state to extrapolate its state at the next time step. If measurements or observations can be made from the system, this estimate can be corrected to produce a new, more accurate estimate for that time step. Recently, there has been some work in recasting parameter estimation as a statistical inference problem in hidden dynamical systems and adopting standard Kalman filter, sequential Monte Carlo, or expectation maximization (EM) frameworks [124, 125, 183, 218, 243, 253]. The Kalman filter is focused on here as a computationally simple algorithm for deterministic nonlinear dynamical systems, such as those used in conductance-based neuron models. It has been demonstrated that the Kalman filter can successfully reconstruct the states and parameters of a neuron model and has been suggested as a possible way to implement dynamic clamp [218, 243, 253]. In contrast to Monte Carlo or EM methods, it is more amenable to real-time implementation. Furthermore, the interpretation of the filter's results are a more natural extension of the way we think in computational neuroscience. While the original Kalman filter is a direct extension of optimal Wiener filtering for linear systems, here we use a modification for handling nonlinear systems known as the *unscented* Kalman filter.

The following simulations demonstrate the quality of estimation that can be expected from simple Kalman filter approaches to this problem and approaches for tuning the filters

for better performance. First, the Kalman filter is tested against surrogate data generated from neuron models, a technique commonly used for offline model-fitting [69]. We follow an approach taken by previously published papers in which the model for the neuron is a single compartment conductance-based model described by differential equations as in Eqn. 1. In this case, the model structure and the values of the fixed parameters are known exactly and the Kalman filter is used to reconstruct the model at different sampling rates and levels of noise. Next, we modify the filter according to commonly encountered challenges in state and parameter estimation: increasing the number of parameters to be estimated and hardcoding incorrect fixed parameter values. Finally, since any computational model will certainly be less complex than a real neuron, the filter is modified to contain a simpler neuron model than that used to generate the surrogate data to test the consequences of model order mismatch. The objective is to develop specific recommendations for real-time implementation of the Kalman filter in electrophysiology experiments in terms of familiar experimental or simulation parameters. For example, it is not clear what sampling rate for the filter is necessary in order to track the fast spiking dynamics or how the filter reacts when the models for the surrogate data and the filter do not match.

Given an accurate model of how a system behaves due to its intrinsic properties, we can then use it to track external inputs to the system, eg. excitatory and inhibitory presynaptic input to a neuron. Methods for measuring these quantities have been the focus of numerous studies in the context of cortical sensory processing [64,88,89,94,95,99,188,210,263,270]. Accurate estimates of these conductances can provide insights about the wiring architecture of the cortex, such as the significance of recurrent excitation and inhibition, and the existence and functional effect of shunting inhibition. Shunting inhibition has been shown to cause nonlinear effects by causing large increases in membrane conductance and can go undetected since it has a reversal potential that is close to that of the cell [29, 79, 171, 196]. Traditional methods for experimentally measuring conductance include using current pulse injections to periodically construct I-V plots throughout an experiment [9, 99, 172, 259], voltage-clamping the cell at multiple holding potentials to determine the average time course of synaptic inputs for a repeated stimulus [17, 104], classical filtering techniques to estimate the combined

synaptic reversal potential from the subthreshold membrane potential averaged over many trials [95, 188]. In the first two cases, dynamic changes in conductance are not observable. In the third case, estimates are very inaccurate when the neuron is spiking because the intrinsic membrane processes dominate over the synaptic input. More recently, a method has been developed based on particle filtering, a sequential Monte Carlo method, to infer the time course of synaptic input in the presence of rapidly-varying stimuli on a single trial basis [182]. This method was demonstrated in simulations and it too computationally expensive to implement in real-time. There are currently no techniques for estimating conductance that can be implemented in real-time during an experiment. Such a technique could also be used to dynamically track the balance between excitation and inhibition and the balance between intrinsic dynamics and synaptic input while delivering behaviorally relevant stimuli.

5.1 Methods

5.1.1 Generation of surrogate data

Three different models were used to generate surrogate data for evaluating the Kalman Filter: the Hodgkin-Huxley model [114–118], the Connor-Stevens model [49, 50], and the Wang-Buzsaki model [256]. These are all single-compartment conductance-based neuron models that follow the form:

$$C_m \frac{dV_m}{dt} = -\sum \left\{ g_i(t)(V_m - E_i) \right\} + I_{app} \tag{18}$$

The models vary in the number of membrane mechanisms that are included and the number of differential equations that must be solved (Table 4). The Hodgkin-Huxley model was developed to reproduce the action potential based on data from the squid giant axon. It contains a fast sodium channel, a delayed rectifier potassium channel, and a leak channel. In addition to the differential membrane equation, the ion channels have three differential equations associated with them. The Connor-Stevens model contains an additional A-type transient potassium channel compared to the Hodgkin-Huxley model and the parameter values for the sodium and delayed rectifier potassium channel are different. The

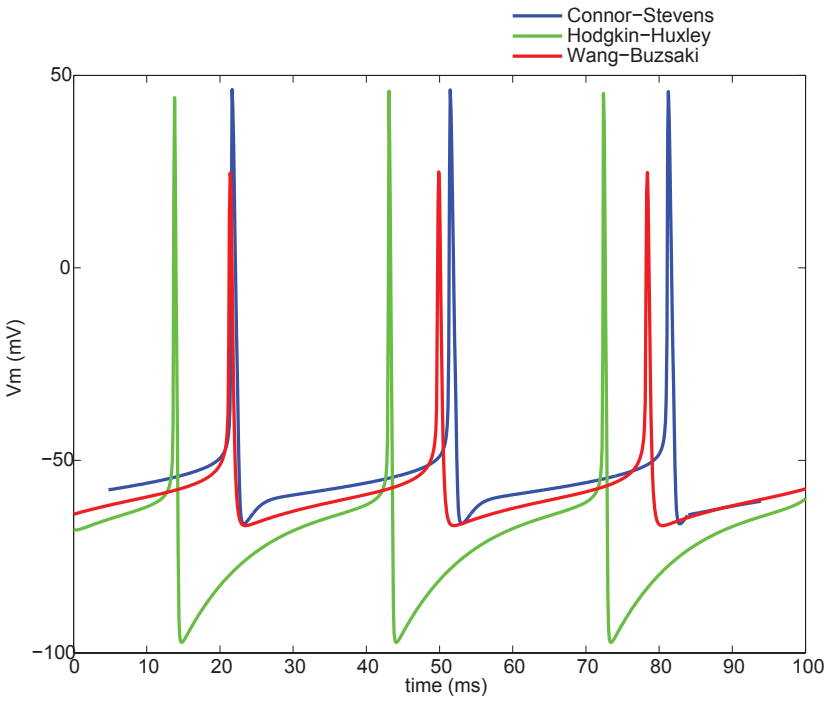

Figure 34: Comparison of spike shapes for neuron models used to evaluate the unscented Kalman filter.

Wang-Buzsaki model was developed for a study of fast oscillations in the neocortex and hippocampus. This model also only features a single sodium and potassium channel. However, the kinetics of the m activation variable for the sodium channel are approximated using its steady-state activation value, which eliminates a differential equation from the system. The full equations and parameter values used are available in Appendix B.3.

The three neuron models used in this study have very different spike shapes (Fig. 34). Compared with the Hodgkin-Huxley model, the Connor-Stevens model has shorter action potentials and a more depolarized average membrane potential. While the membrane potential at the peak of the spike is similar for both models, the Hodgkin-Huxley model spans a far greater range of voltages. The Connor-Stevens and Wang-Buzsaki models share a more similar voltage range but the Wang-Buzsaki model has shorter spikes by $\sim$20 mV. The Connor-Stevens model also has a sharper afterhyperpolarization after the spike than either the Hodgkin-Huxley or Wang-Buzsaki models.

The surrogate data was generated with high accuracy using an adaptive time-step

Table 4: Summary of the different model neuron systems used to evaluate the unscented Kalman filter.

Model	**No. Membrane Mechanisms**	**No. Diff. Eqns.**	**Notes**
Hodgkin-Huxley	2	4	
Connor-Stevens	3	6	Additional potassium current
Wang-Buzsaki	2	3	Steady-state approximation for Na

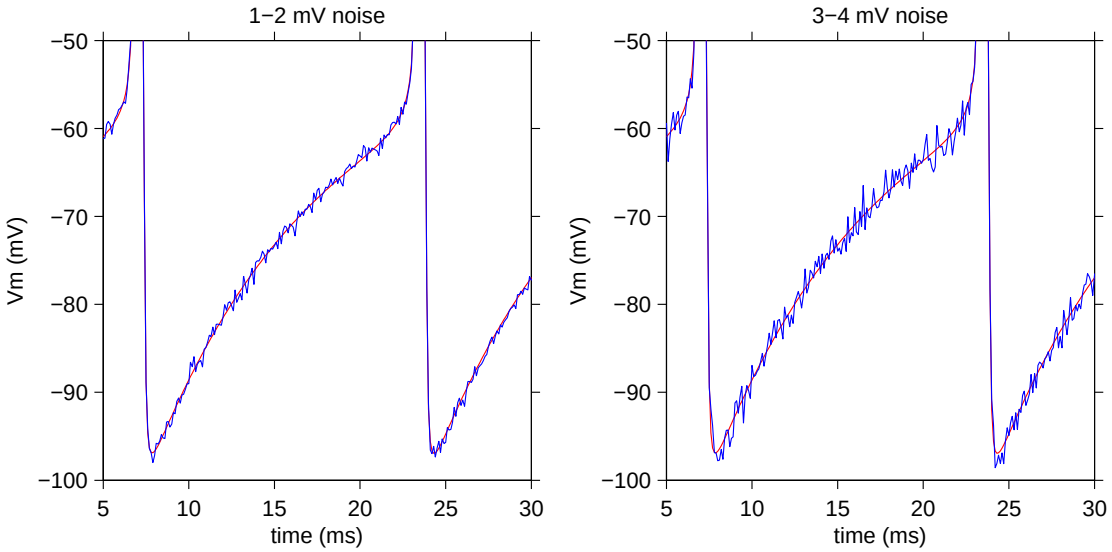

Figure 35: Two different magnitudes of Gaussian white noise were added to the surrogate data generated for the unscented Kalman filter. Left, fluctuations of 1-2 mV simulate the noise typical of invertebrate experiments. Right, fluctuations of 3-4 mV simulate the noise typical of vertebrate experiments.

Dormand-Prince integration method in PyDSTool [44]. The resulting trajectory of the model neuron's behavior was interpolated using fixed time steps at different sampling rates to create the input to the Kalman filter. The error in the "measured" membrane potential was approximated as additive Gaussian white noise applied to each sample point. The variance of this noise was chosen to reproduce typical voltage fluctuations with a magnitude of 1-2 mV or 3-4 mV as commonly seen in invertebrate and vertebrate experiments (Fig. 35).

5.1.2 Implementation of the Unscented Kalman Filter

Since the neuron models are highly nonlinear dynamical systems, we used the unscented Kalman filter (UKF) [134, 136] that was briefly described in the Introduction. The simulations in this study were performed using MATLAB. The states of the Kalman filter correspond to the states of the neuron model, eg. for the Hodgkin-Huxley model, the states are $\mathbf{x} = \begin{bmatrix} V, m, h, n \end{bmatrix}^T$. For parameter estimation, this vector is augmented to include the unknown parameters, such as the conductance density for each ion channel. For the simulations used in this study, a constant external applied current was used to drive the model to spike. While this is a known input during experiments, it is included as a free parameter in some of the following simulations so that the full state vector for the Hodgkin-Huxley model was $\mathbf{x} = \begin{bmatrix} V_m, m, h, n, \bar{g}_{NaF}, \bar{g}_K, I_{app} \end{bmatrix}^T$. The only measurable quantity in an experiment is the membrane potential so the measurement vector is simply $\mathbf{y} = \begin{bmatrix} V_m \end{bmatrix}$. The state and measurement equations that describe the system are given by:

$$\mathbf{x}_{i+1} = F(\mathbf{x}_i) + \mathbf{w}_i \tag{19}$$

$$\mathbf{y}_{i+1} = G(\mathbf{x}_i) + \mathbf{v}_i \tag{20}$$

$$\mathbf{w} \sim (0, Q_w) \tag{21}$$

$$\mathbf{v} \sim (0, Q_v) \tag{22}$$

where $\mathbf{w}$ and $\mathbf{v}$ are random numbers sampled from a Gaussian distribution with zero mean and standard deviations of Q_w and Q_v. In these simulations, the same value of Q_w was used for all the system states though this is not a requirement of the algorithm. Choosing different values for each state may actually improve the performance of the filter.

Since the goal of this work is to evaluate the performance of the UKF in real-time with neurons, we chose numerical methods and sampling rates guided by current heuristics for dynamic clamp experiments. The state variables in the system were evolved according to a single Euler integration step:

$$F(\mathbf{x}_i) = \mathbf{x}_i + \mathbf{dx}_i * dt \tag{23}$$

$G(\mathbf{y})$ is simply the direct observation of V_m. These choices have been shown to be sufficiently

accurate to reproduce ion channel dynamics. While the canonical Kalman filter uses only the current time step, it can be formulated to use multiple measurement and estimation data points to produce a filter matching the order of the desired numerical integrator. The estimated error for the state values is stored in an error covariance matrix, $\mathbf{P}$, a diagonal matrix with the same number of dimensions as the state vector. The diagonal values of $\mathbf{P}$ are related to Q_w, the variance of noise assumed to be in the system according to the state equations in Eqns. 19-22.

The UKF uses the "unscented transform" to propagate mean and covariance information through nonlinear transformations [134, 136]. The unscented transform works by constructing a set of points, referred to as sigma points, χ_i, that as a population capture the same known statistics, mean and covariance, as a given measurement or state estimate. A specified nonlinear transformation can be applied to each sigma point, and the unscented estimate can be obtained by computing the statistics of the transformed set. For example, the mean and covariance of the transformed set approximates the nonlinear transformation of the original mean and covariance estimate. The sigma points are determined by computing the square root of the error covariance matrix and adding the resulting plus or minus standard deviation to the state estimates:

$$\tilde{\chi}_i = \bar{\mathbf{x}} \pm (\sqrt{n\mathbf{P}})_i \text{ with i=1,...,n} \tag{24}$$

Unlike Monte Carlo techniques, this is a deterministic rather than random sampling method so only a small number of points is needed. There are $2n$ sigma points, twice as many points as states in the filter. Each sigma point is propagated through the complete nonlinear equations of the neuron model to produce a set of state estimates. This set is then averaged back into a single new state estimate with an updated mean and covariance and constitute the *a priori* estimate before any measurements are made from the system:

$$\tilde{\mathbf{x}} = \frac{1}{2n}\sum_{i=1}^{2n}\tilde{\chi}_i \tag{25}$$

$$\tilde{\mathbf{P}}_{xx} = \frac{1}{2n}\sum_{i=1}^{2n}(\tilde{\chi}_i - \tilde{\mathbf{x}})(\tilde{\chi}_i - \tilde{\mathbf{x}})' + \mathbf{Q_w} \tag{26}$$

In comparison, the extended Kalman filter linearizes the system using series approximations, a process that becomes increasingly difficult for complex dynamical systems since the derivatives of the system equations must be determined analytically or approximated. The UKF transformation method preserves the second order accuracy in mean and covariance and guarantees the same performance as a truncated second order filter with the same order of calculations as the extended Kalman filter.

Similarly, a set of measurement vectors, $\mathcal{Y}_i$, is determined from the sigma points and they are also averaged to a single measurement, where $\tilde{\mathbf{P}}_{yy}$ represents the error in the model's predicted measurements:

$$\tilde{\mathbf{y}} = \frac{1}{2n}\sum_{i=1}^{2n}\mathcal{Y}_i \tag{27}$$

$$\tilde{\mathbf{P}}_{yy} = \frac{1}{2n}\sum_{i=1}^{2n}(\tilde{\mathcal{Y}}_i - \tilde{\mathbf{y}})(\tilde{\mathcal{Y}}_i - \tilde{\mathbf{y}})' + \mathbf{Q_v} \tag{28}$$

We also compute the cross-covariance between the model's state predictions and the measurement predictions:

$$\tilde{\mathbf{P}}_{xy} = \frac{1}{2n}\sum_{i=1}^{2n}(\tilde{\chi}_i - \tilde{\mathbf{x}})(\tilde{\mathcal{Y}}_i - \tilde{\mathbf{y}})' \tag{29}$$

The ratio between this cross covariance and the error in the model's measurement prediction gives the Kalman gain:

$$K = \tilde{\mathbf{P}}_{xy}\tilde{\mathbf{P}}_{yy}^{-1} \tag{30}$$

Rather than compute the matrix inverse, the matrix division operator in MATLAB is used. The Kalman gain is used to scale the correction added to the *a priori* state estimate. When the variance in the model's measurement prediction is low, the Kalman gain is high and more weight is given to the measured information. When the variance in the model's predicted state values is low, the Kalman gain is low and the corrective term is smaller. The final state estimate is:

$$\hat{\mathbf{x}} = \tilde{\mathbf{x}} + K(\mathbf{y} - \tilde{\mathbf{y}}) \tag{31}$$

The last step is to update the *a posteriori* error covariance matrix:

$$\hat{\mathbf{P}}_{xx} = \tilde{\mathbf{P}}_{xx} - K\tilde{\mathbf{P}}'_{xy} \tag{32}$$

Eqns. 24 to 32 represent the full UKF algorithm. The matrix square root for Eqn. 24 was computed using MATLAB's built-in Cholesky decomposition algorithm. Since the filter is a statistical technique, our approach was to begin with as few assumptions as possible about the system and implemented the canonical UKF. For example, the values of the conductance density for each ion channel must be non-negative and the gating variables are restricted to values between 0 and 1. Both of these constraints could be implemented by remapping incorrect values into the correct range on each time step. In general, this did not improve the estimates produced by the filter.

5.1.3 Initialization of the Unscented Kalman Filter

To implement the Kalman filter, the user must also have knowledge of the statistics of the system and measurement noise processes, an initial estimate for the state values, and an initial error covariance matrix. Based on these assumptions and the inputs to Kalman filter, the filter may fail to converge or converge onto incorrect estimates. For example, a Kalman filter for linear systems may not be very sensitive to the initial conditions of the filter. Nonlinear systems can be sensitive to initial conditions though it may be enough to initialize the filter using a set of states during a stationary region in the system's trajectory. This is similar to the classical situation with conventional neuron models in which the initial conditions affect the steady-state behavior of the model. The UKF assumes that each state is modeled by a normal distribution and they must be initialized with a starting value and variance. The states were initialized using the first measured value of the membrane potential. The activation variables were initialized to their steady-state values dependent on the initial voltage, a technique commonly used in computational neuroscience.

In Eqns. 26 and 28, Q_w and Q_v are added directly to the terms in the covariance matrices. This is an option when executing the Kalman filter known as covariance inflation [122]. These terms could be left out, or alternatively, the terms of the covariance matrices could simply be set equal to Q_w or Q_v. These values play an important role in determining

which term is weighted more in Eqn. 31: the *a priori* state estimate based on the model predictions alone or the actual measurements from the system. For example, a larger Q_w corresponds to less confidence in the model and initial parameter values, and more confidence in system measurements. The result is that the Kalman filter outputs larger changes in state and parameter estimates with each time step, and consequently converges more quickly. Theoretically, the variance of membrane potential noise can be estimated from experimental data and the variance of noise in the gating variables can be inferred from their distribution in simulated data. A $Q_w = 16$ mV^2 for the measured membrane potential means that it has a standard deviation of 4 mV. In practice, the initial error for each state in a Kalman filter is generally set to an arbitrarily "large" value since often the true error cannot be directly measured. Since the error is minimized over time by the filter, initializing it at too large a value is generally not a problem. However, underestimating the error can prevent the filter from converging or cause it to not run at all.

Conventional techniques for fitting the parameters of a neuron model typically use a global error over a complete spike cycle. Complex nonlinear spike dynamics may be fit well in certain phases of a spike cycle with a low order model and these compensate for other phases in which the error is large. A recursive technique like the Kalman filter is designed to produce continuous output that tracks an observed state variable as closely as possible. While for linear systems it ultimately minimizes the same global error, it operates based on a local error only and can fail to operate at all. Nonconvergence typically means that the estimates are useless because error terms have grown without bound. A failure of the filter to even operate usually indicates a numerical issue with the error covariance matrices, such as being unable to compute a matrix inverse due to singularity. Covariance inflation can stabilize the filter and encourage convergence, especially for systems with nonstationary behavior. In this work, the covariance matrices were reset to Q_w on each time step and was generally kept the same for all the state variables. In some cases, the value of Q_w is different for each state, so that the estimates of certain states are allowed to vary more aggressively than others.

It is more common that Kalman filter does not converge because the model does not

correctly describe the system or that the initial assumptions become invalid over time as the system evolves. In particular, we model a branched morphology with a single compartment and the model certainly simplifies complex ion channel dynamics. Model errors can cause the filter to underestimate the uncertainty in the state estimates such that the observable quantities become irrelevant. This leads to accumulating errors in the state estimate and is more likely for systems whose high order nonlinearities are not preserved by the filter.

5.2 Results

5.2.1 Reconstructing states and parameters for a known neuron model

It has already been shown for both the Fitzhugh-Nagumo and Hodgkin-Huxley models that the UKF can reconstruct a known model, including the gating variables and the conductance densities of the ion channels [243, 253]. Here, we replicate and expand on previous work to explore how the filter performs in the face of commonly encountered challenges in computational neuroscience. Results from a typical UKF simulation operating at 10 kHz for a Hodgkin-Huxley model neuron are shown in Figs. 36-37. The model neuron was driven with a constant external current that caused it to spike at ∼60 Hz. Within 2 seconds of simulation, or ∼120 spikes, the filter is able to accurately track the membrane potential as well as the gating variables of the sodium and potassium conductances. These estimates are a combination of a predicted value for each state variable based on the current parameter values as well as a correction that is based on measuring the true membrane potential at that point in time. These estimates improve over time as the filter approaches the true parameters and dynamics of the model system (Fig. 37).

The estimates for the parameter values increase in a step-wise fashion and each adjustment is associated with a spike (Fig. 38). This makes sense since the sodium conductance is primarily active during the spike and it is only during this period that useful information can be obtained about its dynamics. The magnitude of each adjustment decreases as the estimate approaches the true value. At a sampling rate of 10 kHz, the values for the ion conductance densities do not converge for ∼10 s and retain a residual error. At 10 kHz, the final parameter values after 10 s of simulation for these filter parameters were $g_{NaF} = 98.5$

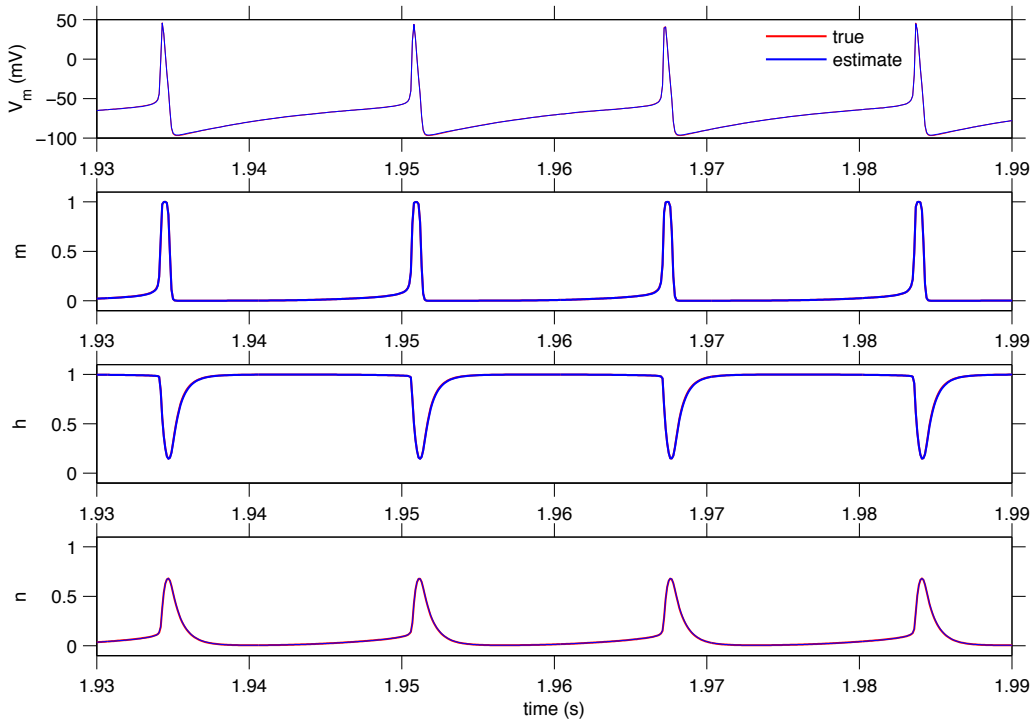

Figure 36: A typical UKF simulation for the Hodgkin-Huxley model. The filter continuously tracked the membrane potential and underlying gating variables of the ion channels.
Simulation parameters: sampling rate = 10 kHz, $Q_w = 0.016$

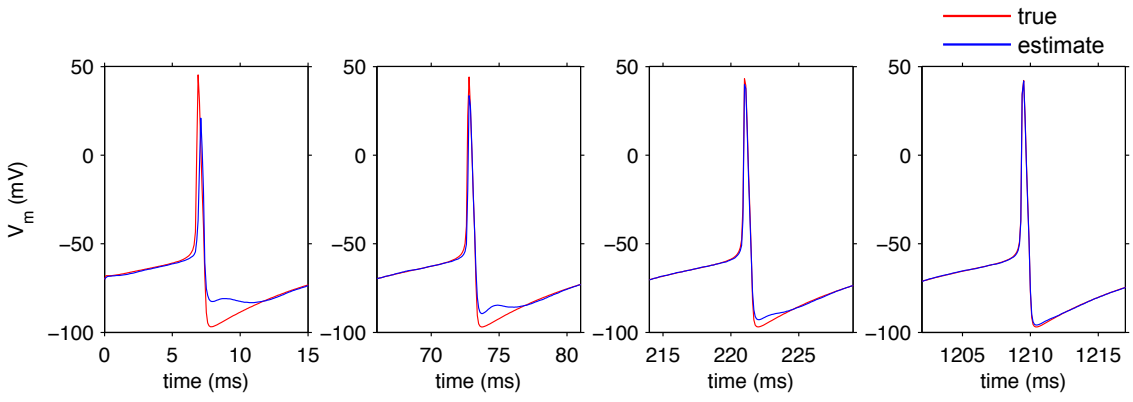

Figure 37: Over time, the UKF is able to track the membrane potential more closely, even before it has converged onto the correct parameter values for the maximal conductances compare time scale with Fig. 38).
Simulation parameters: sampling rate = 10 kHz, $Q_w = 0.016$

mS/cm^2 and $g_K = 78.2$ mS/cm^2. Interestingly, as the estimate for g_{NaF} nears its true value, the estimate for the applied current changes as well. While it initially features large transients that correspond to each spike, they eventually recede until the estimate of I_{app} varies noisily around its true value. The amplitude of these fluctuations is related to the value of Q_w, which controls the level of intrinsic noise that is expected in the system. A smaller Q_w results in smaller amplitude fluctuations in I_{app} but affects the convergence properties of the filter. It is possible to modify the Kalman filter model such that parameters are explicitly restricted from varying so widely on each time step.

Including I_{app} as an estimated parameter in the filter improved its performance. When estimating only the conductance densities, the filter often failed to operate unless Q_w was carefully tuned and the initial conditions were close to the true parameter values. When the initial conductance densities are intialized naively at 0 mV, they play no role in generating spikes at the beginning of the filter's operation. The filter accounts for each spike with a large inward current and this alternative explanation gives the filter enough flexibility to continue operating until the other parameters come into play. These results could be interpreted as the Kalman filter learning to distinguish between two completely different mechanisms for replicating the observed voltage transients: 1) a voltage-dependent conductance with fast deterministic kinetics, or 2) a noisy constant current.

The UKF can also distinguish between two membrane mechanisms that differ in more subtle ways. For example, the Connor-Stevens model has two potassium conductances. The delayed rectifier potassium channel (K_{dr}) is responsible for repolarizing the membrane after a spike. The transient A-type potassium channel (K_A) is activated at subthreshold voltages and also show pronounced inactivation with sustained depolarization at these voltages. It is primarily active within the interspike interval and has been shown to play a functional role in regularizing spiking in pacemaker neurons. The UKF can reconstruct the states and parameters of the Connor-Stevens model as well but only when the error covariance was increased to $Q_w = 0.14$ (Fig. 39). Below this value, the filter fails to converge. As before, the largest adjustments to the conductance estimates for the spike-generating currents occur with each spike. The estimate for g_{KA} varies continuously throughout the simulation until

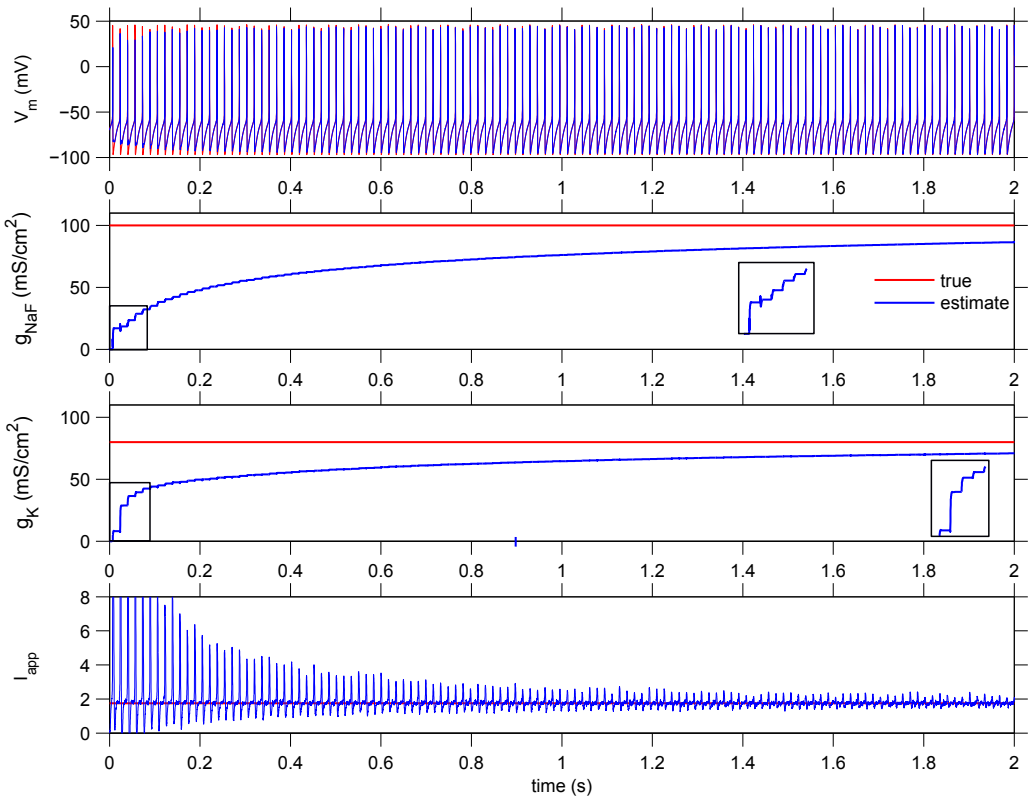

Figure 38: A typical UKF simulation for the Hodgkin-Huxley model. The UKF estimated the conductance densities of the ion channels and the constant externally applied current. The true values of the conductance densities and the applied current are shown in red. The final parameter values after 10s of simulation for these filter parameters were $g_{NaF} = 98.5$ mS/cm^2 and $g_K = 78.2$ mS/cm^2.
Simulation parameters: sampling rate = 10 kHz, $Q_w = 0.016$

all the conductance densities reach their true values. Since both channels have similar reversal potentials, an initial overestimate of g_K corresponds with an underestimate of g_{KA}. This is ultimately resolved because the channels are active within two different voltage ranges with very different kinetics (Fig. 40). Issues would arise if we attempted to determine the conductance densities of channels with very similar kinetics even if they had different reversal potentials. The filter would simply compensate an error in one conductance with the opposite error in the other conductance. In these cases, additional information could be used to constrain the filter, such as data about typical relative conductance densities in that neuron.

There are numerous methods for fitting parameters to a neuron model when only the

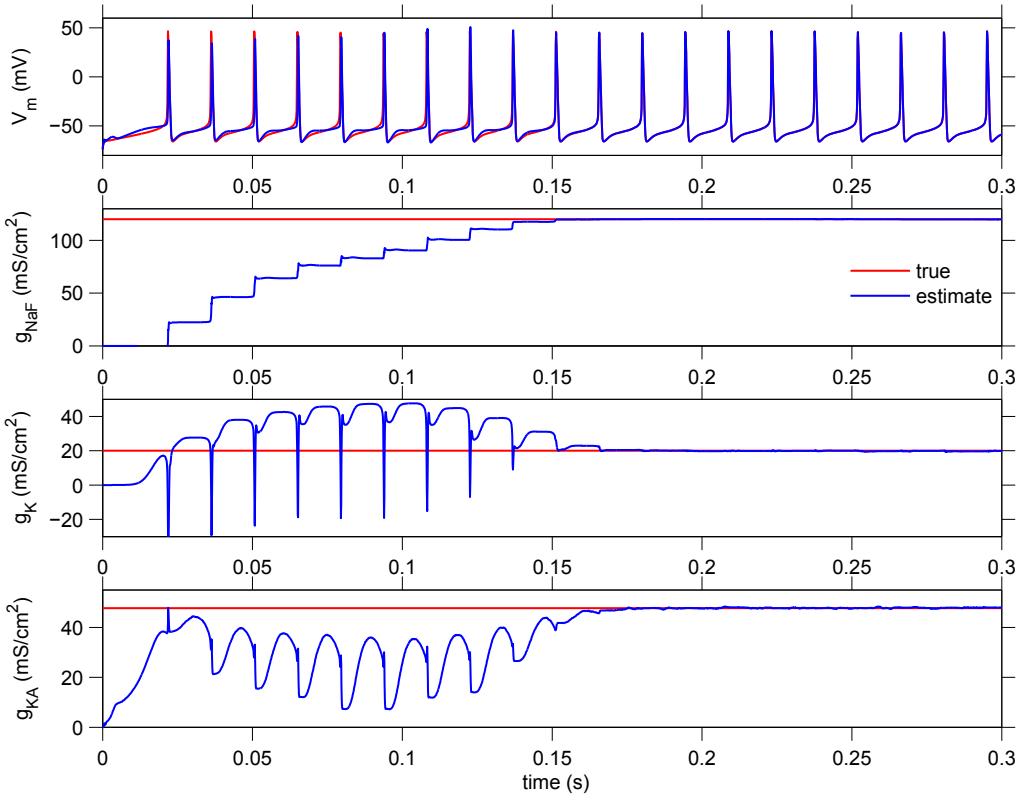

Figure 39: A typical UKF simulation for the Connor-Stevens model. The filter continuously tracked the membrane potential and underlying gating variables of the ion channels as well as the ion channel conductance densities. The true values are shown in red.
Simulation parameters: sampling rate = 10 kHz, $Q_w = 0.14$

conductance densities of the ion channels are left free. It is much more difficult to develop a model to fit target data when the reversal potentials and underlying kinetics parameters in the nonlinear equations are also left free. To date, the only successful techniques for fitting complete sets of kinetic parameters in a brute force manner involve evolutionary algorithms and systematic database approaches that explore a large parameter space, often combined with local gradient search methods. The difficulty of the UKF's task increases with the size of the system, in large part to the matrix operations involved. In comparison with the Hodgkin-Huxley model, the Connor-Stevens model adds two differential equations, one parameter, and two state variables to the system. This increases the number of state dimensions by 3 and the value of Q_w must increase nearly ten-fold for the filter to converge on the true values for the estimated parameters. The UKF was able to handle a situation in which only the sodium reversal potential in addition to the conductance densities were left

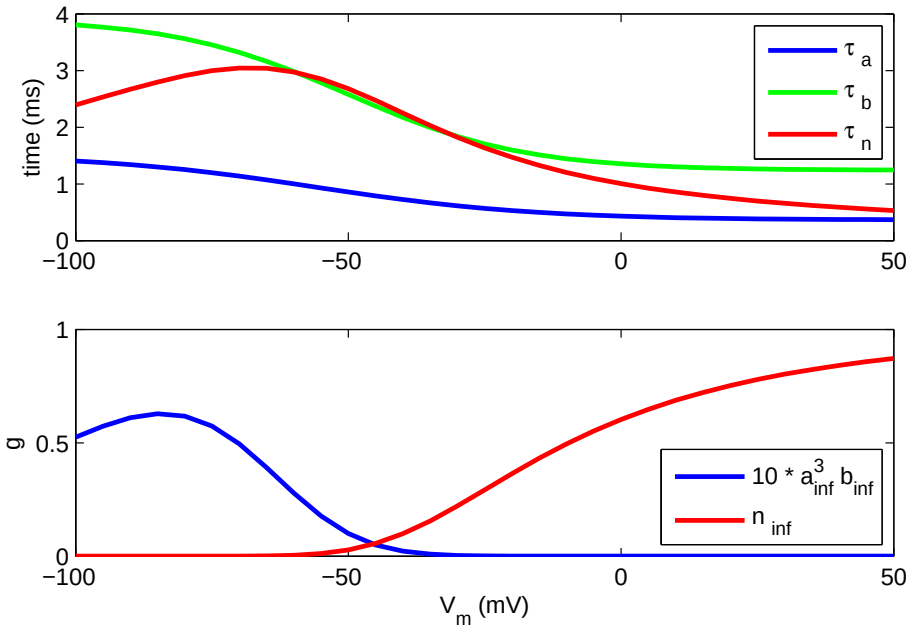

Figure 40: Voltage-dependence of the potassium conductances in the Connor-Stevens model.

free and initialized naively at 0 mV. It was unable to operate when both the sodium and potassium conductances were left free unless the estimates were initialized closer to their true values (Fig. 41). Here, initial conditions were chosen at least 25% away from each reversal potential's true value and the filter was able to converge from either side in ∼5 s. Traditional voltage clamp experiments can generally determine reversal potentials within this range so that the UKF algorithm could estimate the correct reversal potentials as well as maximal conductances.

5.2.2 Effects of sampling rate and measurement noise

The filter is able to converge on the correct parameter values and more accurately track the state variables as more measurements are made from the system. The sampling rate at which the filter operates and the amount of noise in the measurements directly affect the filter's performance. The data shown so far were generated at a sampling rate of 10 kHz, which is a typical dynamic clamp sampling rate. Due to the computational overhead of the matrix operations, it is important to determine whether the Kalman can still produce meaningful results at lower sampling rates. In general, the filter converges more quickly as the sampling

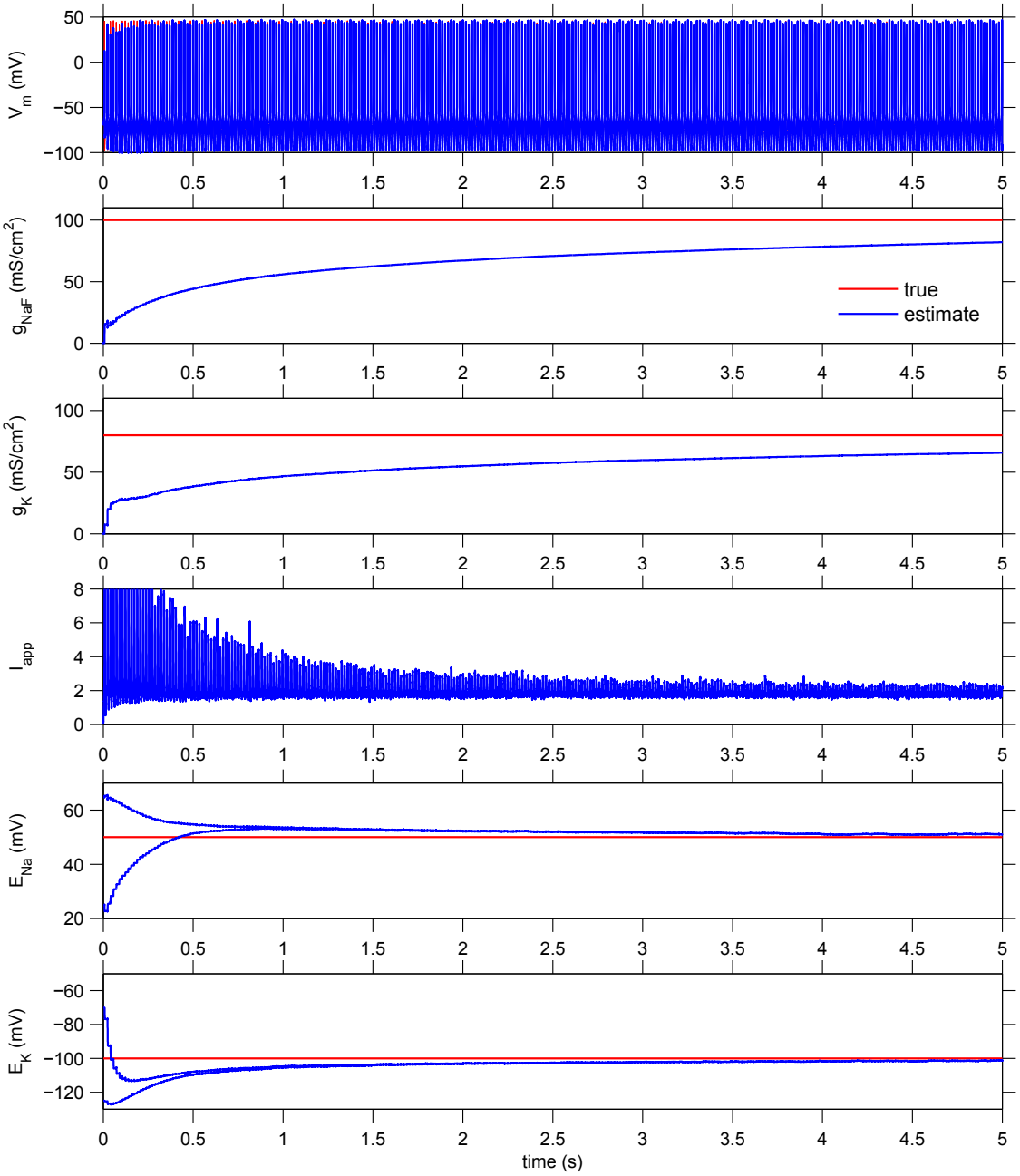

Figure 41: The UKF can simultaneously estimate the conductance densities of the sodium and potassium conductances as well as the reversal potential of the sodium channel. However, it is unable to estimate both reversal potentials at the same time when they are initialized naively at 0 mV. The reversal potentials were initialized at $[E_{Na}, E_K]$ = [25, -70] or [65, -125] mV. The maximal conductances converge to the true values at ∼15 s. Results in the top four panels are shown for the initial conditions $[E_{Na},E_K]$ = [25, -70] mV. The conductance density estimates for both simulations converged at ∼15 s.
Simulation parameters: sampling rate = 10 kHz, $Q_w = 0.025$

rate is increased (Fig. 42). While these gains are large at lower sampling rates, there are diminishing benefits above 20 kHz. At the lowest sampling rates, the estimates produced by the filter may increase non-monotonically towards the true parameter value and the filter may fail to operate at all. The UKF used here is reasonably robust to subsampling, producing accurate results even at 6 kHz. Increasing the sampling rate, however, only results in slightly more accurate values for the final estimates of each conductance density (Table 5). When plotted versus the sample number, the envelope of the convergence curves are closely aligned (Fig. 42, bottom). Convergence time is clearly a function of the number of cycles the filter has to sample. Consequently, when the Kalman filter samples at a higher rate, convergence happens more quickly.

The rate of convergence of the filter's results also decreases as the amount of measurement noise increases. We simulated two levels of measurement noise to reproduce the magnitude of membrane potential fluctuations that are commonly seen in invertebrate and vertebrate experiments (Fig. 42A). Since this level of noise can be estimated by observing voltage traces, it is assumed that the value of this variance is a fairly accurate input parameter to the Kalman filter. For the simulations performed using the Hodgkin-Huxley model, the filter converged on accurate estimates even at the higher level of measurement noise. The noise inherent in actual biological experiments would likely not be problematic. Importantly, there will be a minimum sampling rate below which the filter will not converge and this rate will depend both on the noise in the system as well as the dynamics of spiking. The actual spike rate is not as important as the width of the spike since the interspike interval is typically much longer. The UKF produces good results provided that the spike itself is well-sampled.

5.2.3 Consequences of model parameter mismatch

So far, we have reproduced previously published results that showed that the UKF can successfully reconstruct the underlying states and conductance densities in a single compartment neuron model when all other parameters are known. In reality, there is a great

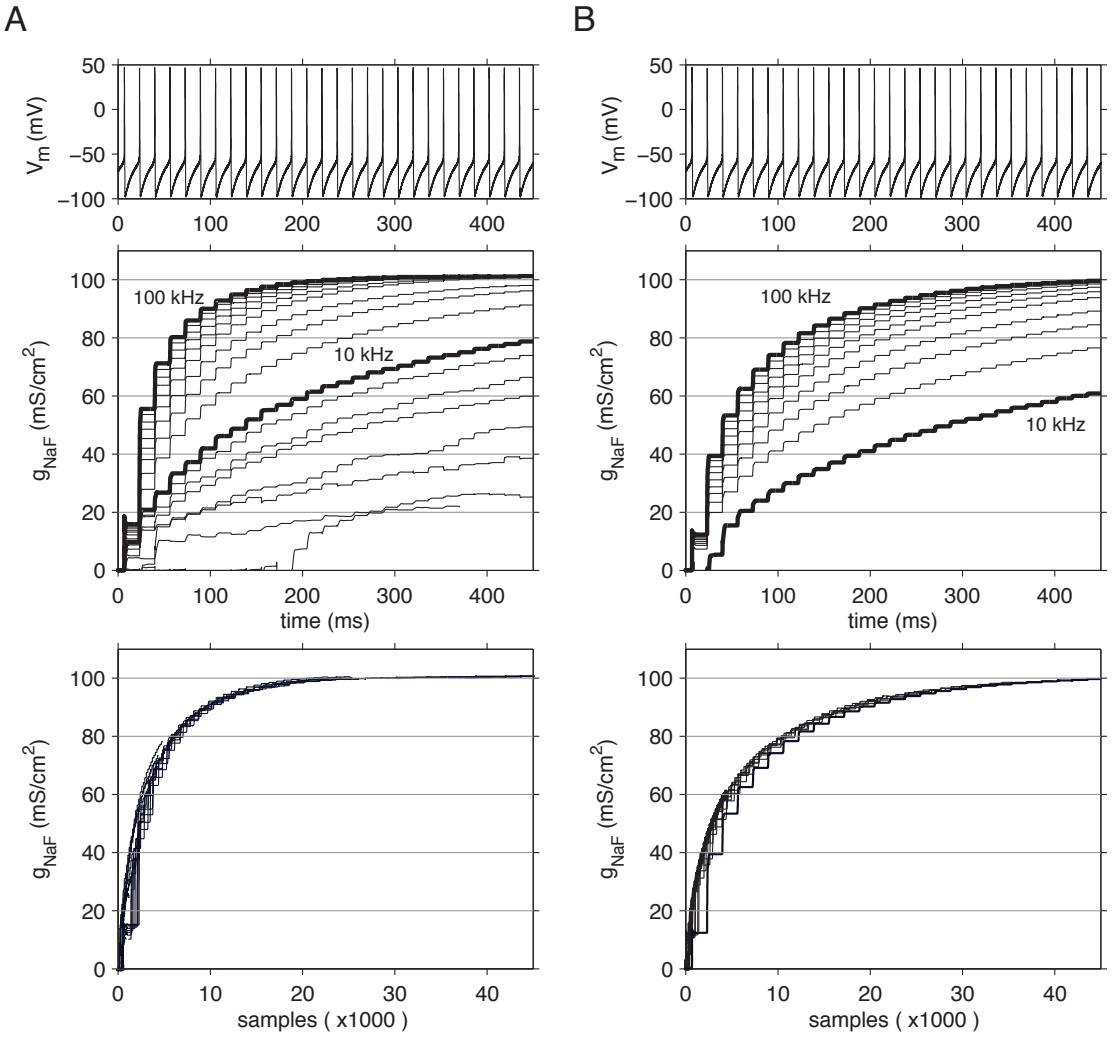

Figure 42: The UKF converges on the true value of the model parameters more quickly at higher sampling rates and when the amount of measurement noise is lower. A) Convergence for 1-2 mV voltage fluctuations as shown in Fig. 35A. The estimate for g_{NaF} increases nonmontonically at low sampling rates and eventually may not converge at all. B) Convergence for 3-4 mV voltage fluctuations as shown in Fig. 35B. Simulations performed at 10 and 100 kHz are shown in thicker lines.

Table 5: Final conductance density estimates for the Hodgkin-Huxley model estimated by the UKF at different sampling rates after 10 s of simulation time. The true values are $g_{NaF} = 100$ mS/cm^2 and $g_K = 80$ mS/cm^2.

Sampling Rate (kHz)	g_{NaF} (mS/cm^2)	g_K (mS/cm^2)
6	96.1	76.3
7	97.1	77.0
8	97.7	77.5
9	98.0	77.6
10	98.5	78.2
20	99.1	78.8
30	99.2	79.2
40	99.2	79.3

deal of biological variability between neurons of the same type and these "hard-coded" parameter values may be incorrect. In some cases, the output of the filter is as expected. For example, when the leak conductance density, g_L, is changed from 0.10 to 0.15 mS/cm^2, this lowers the overall excitability of the neuron since the leak reversal potential is -67 mV. When the UKF is asked to estimate the sodium and potassium conductances as well as the applied current, it estimates a higher external current than was actually used in order to compensate for a larger leak conductance (Fig. 43).

When the leak reversal potential, E_L, is changed from -67 mV to -75 mV, the UKF can still converge onto to the correct ion channel conductance densities (Fig. 44). Instead, the estimate from the applied current retains an oscillation around its true value that does not completely diminish over time. This is because changing the reversal potential is not equivalent to a constant change in excitability. Rather it changes the driving force for the leak current and each oscillation is associated with a spike, where the leak driving force is at a maximum.

When both of these parameters are fixed at the incorrect values, the filter is still able to converge onto the correct ion channel conductance densities (Fig. 45). Interestingly, there is no loss in the rate of convergence. Furthermore, the filter's estimate of the applied current is a combination of those already described. I_{app} retains an oscillation but at a value offset from the true value. However, the filter failed to converge at a sampling rate of 10 kHz. To get these results, the simulation was run at 20 kHz.

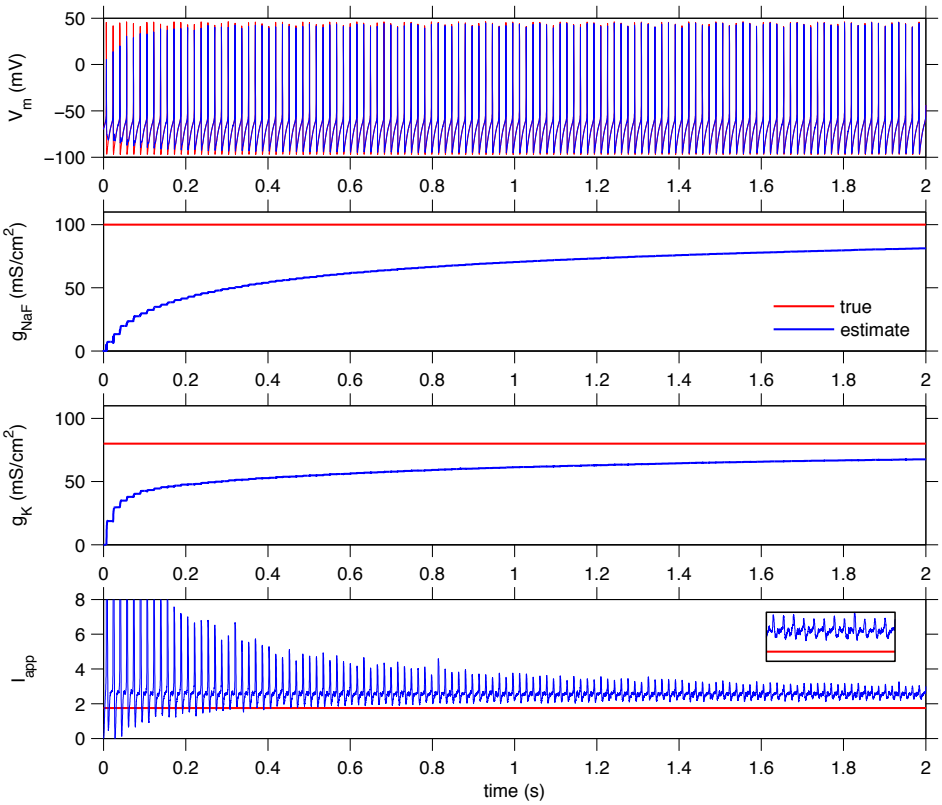

Figure 43: The UKF can simultaneously estimate the conductance densities of the sodium and potassium conductances when the leak conductance density is fixed at an incorrect value ($g_L = 0.15$ instead of 0.10 mS/cm^2). The filter accounts for the decrease in the overall excitability of the model by estimating an external applied current that is larger than the true value.
Simulation parameters: sampling rate = 10 kHz, $Q_w = 0.016$

All the simulations in this section ultimately did converge onto the correct values for the conductance densities at ∼10 s. In large part, this may be because the only other membrane mechanisms present in this system are specifically associated with generating the spike. It is much easier to account for an overall change in excitability by manipulating the magnitude of a time-varying applied current rather than conductances governed by these fast kinetics.

5.2.4 Consequences of model order mismatch

We previously considered the situation in which the values of fixed parameters in the neuron were incorrect. An equally common problem in computational neuroscience is when the chosen model structure is incorrect. Often, an ion channel model developed for a different neuron type, or even a different animal, is borrowed and the parameters are tuned to

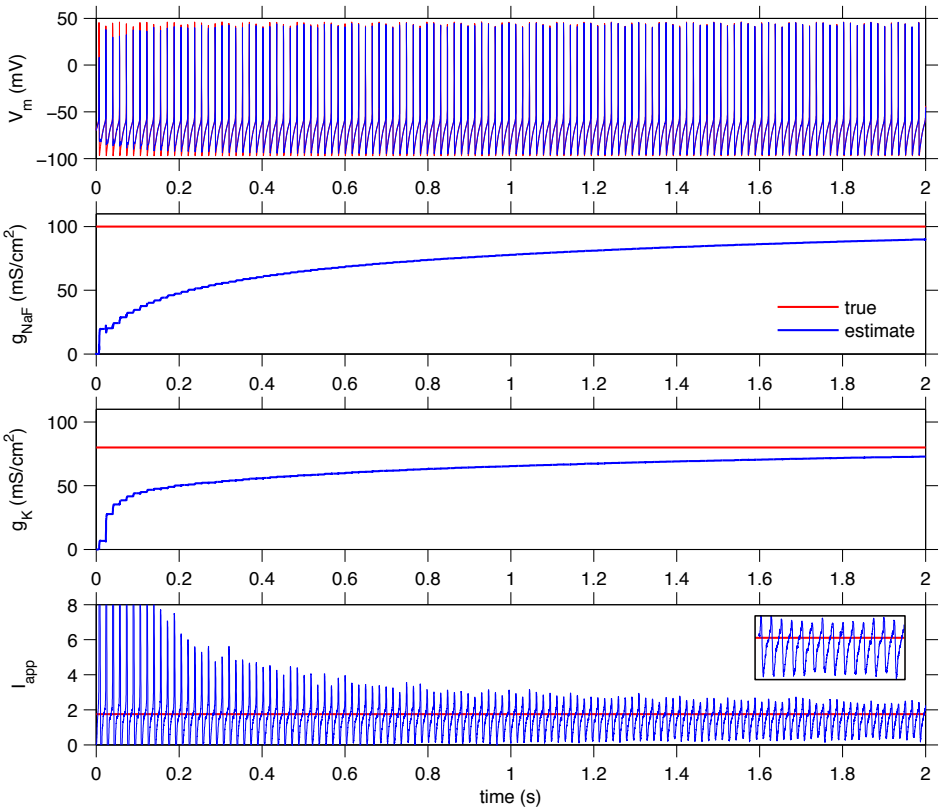

Figure 44: The UKF can simultaneously estimate the conductance densities of the sodium and potassium conductances when the leak conductance reversal potential is fixed at an incorrect value (E_L = -75 mV instead of -67 mV). The filter's estimate of I_{app} features large oscillations around the true value to account for differences in the leak driving force.
Simulation parameters: sampling rate = 10 kHz, $Q_w = 0.016$

produce the desired results. There are numerous challenges to applying the UKF technique in experiments with actual neurons for model-fitting purposes. In particular, we know that the model simplifies the complex dynamics of ion channel processes, may not account for all the membrane processes that are actually present in the biological neuron, and does not account for a branched morphology. Furthermore, the goal of the filter is to match a target trajectory by adjusting the underlying parameters or unobservable states. Thus, it is possible for the filter to track the membrane potential "accurately" and still produce meaningless estimates for other state variables and parameters. As shown before, leaving I_{app} as a free parameter gives the filter a great deal of flexibility since its magnitude is easily adjusted to track V_m. To approximate this situation of "model order mismatch," we mixed the models used to generate the surrogate data and the models used in the Kalman filter.

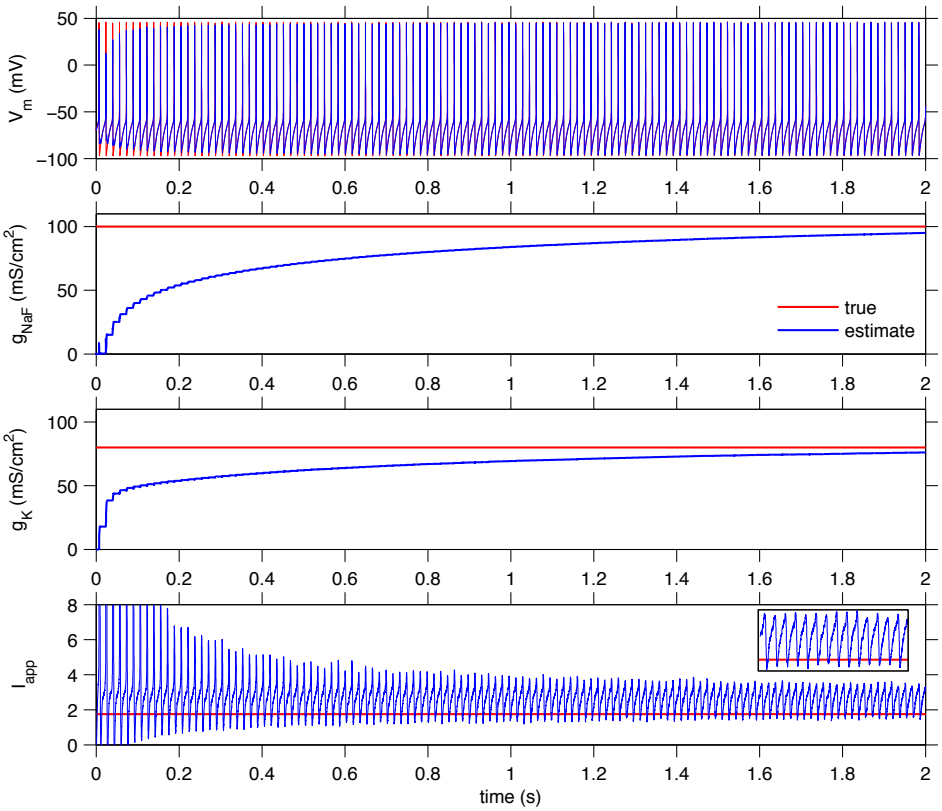

Figure 45: The UKF can simultaneously estimate the conductance densities of the sodium and potassium conductances when the leak conductance density and reversal potential are both fixed at incorrect values. The filter's estimate of I_{app} is a combination of the two separate effects seen previously. It retains an oscillation around a value that is offset from the true value.
Simulation parameters: sampling rate = 20 kHz, $Q_w = 0.016$

We initially attempted to feed data generated by the Hodgkin-Huxley model into a Kalman filter with an embedded Wang-Buzsaki model to estimate the ion conductance densities and applied current. In these simulations, the value of Q_w was increased to express lower confidence in the accuracy of the Kalman filter model. Numerically, this allows the parameter and state estimates to vary more so that the estimated trajectory for the membrane potential matches the observed value more closely. In many cases the filter failed to operate at all and adjusting the value of Q_w and the initial conditions of the filter did not improve its performance. While an important difference between the two models is the steady-state approximation for the sodium channel in the Wang-Buzsaki, this filter was unsuccessful primarily because the the voltage ranges of the models are very different (Fig. 34). The Wang-Buzsaki model was unable to generate the extremely hyperpolarized

potentials present in the Hodgkin-Huxley model and the large differences in the driving force for each conductance.

The filter was then modified to also include the reversal potentials as free parameters to allow the algorithm to adjust the driving forces for each conductance (UKF1 in Table 6). This approach allowed the filter to operate and determine new values for g_K as well as the reversal potentials. However, g_{NaF} grew far out of the reasonable range when compared to g_K and for the length of the simulation (15 s) did not truly converge. The estimate for the applied current also displayed large transients above the true value that corresponded with each spike (Fig. 46).

Next, we linearly scaled the voltage range of the Hodgkin-Huxley model output to match the range of the Wang-Buzsaki model and used these values as the input to the filter while retaining the reversal potentials as free parameters (UKF2 in Table 6). This prevented the estimate for g_{NaF} from growing without bound and constrained the estimate for I_{app} to much smaller oscillations round the true value. Effectively, the filter was restricted mostly to conductance-based mechanisms to generate the specific spike shape rather than resorting to manipulating the applied current. However, the sodium reversal potential grew without bound in this case (Fig. 47).

In the previous simulations, the reversal potentials were allowed to vary in order to adjust the driving forces for each conductance. However, the underlying kinetic parameters were still fixed at the values for the canonical Wang-Buzsaki model such that the activation ranges for the conductances were not shifted as well. We modified the filter to also include the voltage shift for the forward reaction rate for the sodium activation variable, α_m (UKF3 in Table 6). It was initialized at the canonical value and allowed to vary from there. The kinetic parameters for the potassium conductance were left fixed because the two previous simulations resulted in parameter estimates that converged to values that were very similar and close to the canonical Wang-Buzsaki parameters (Table 6). This final filter had the following 9-dimensional state vector: $\mathbf{x} = \left[V, h, n, \bar{g}_{NaF}, \bar{g}_K, I_{app}, E_{Na}, E_K, \alpha_{m_{shift}}\right]^T$. For all the free parameters, this filter produced estimates that converged within 5 s to values comparable to those typically used in single compartment neuron models. The estimate for

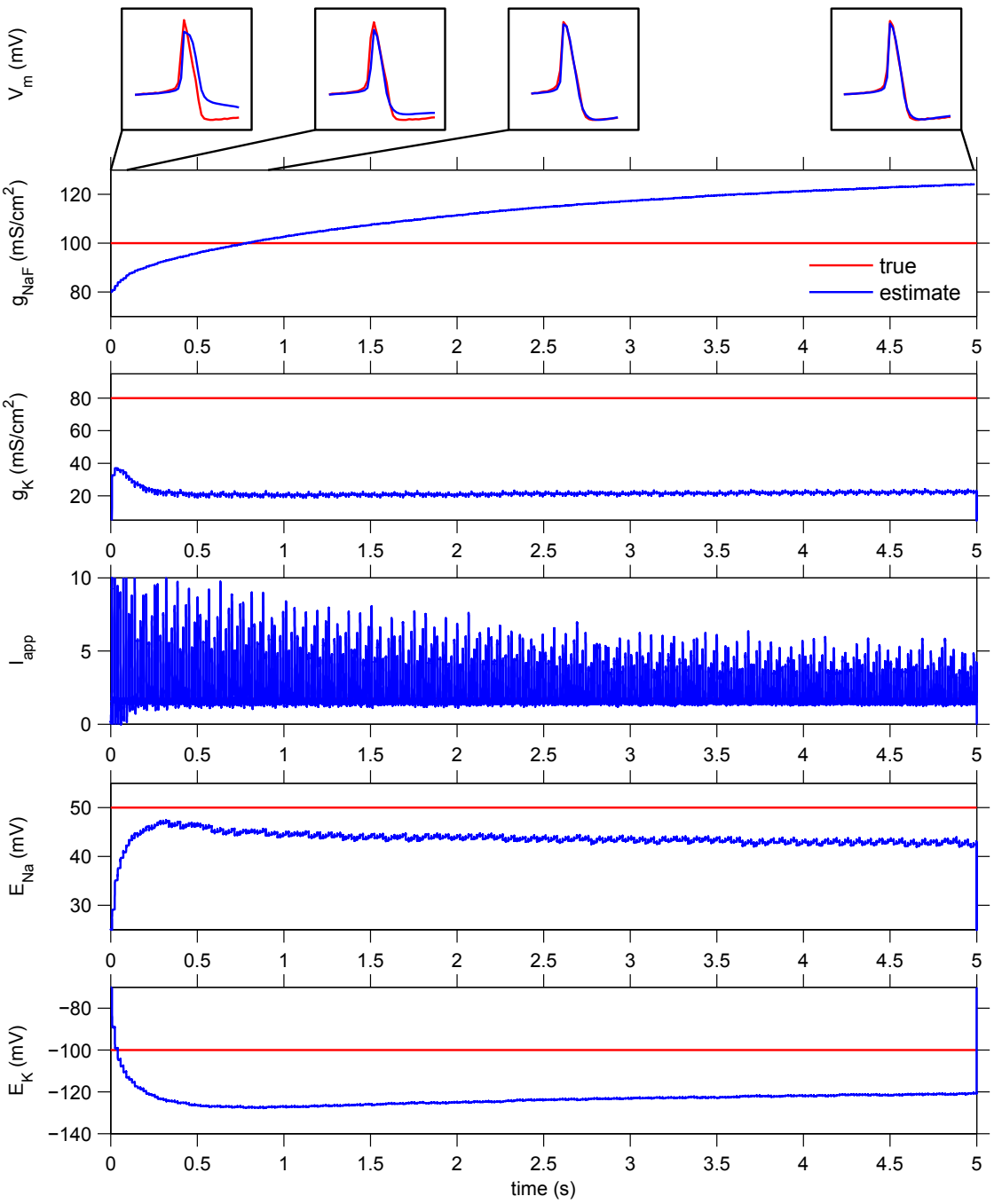

Figure 46: Surrogate data generated using the Hodgkin-Huxley model was fit with a UKF containing a Wang-Buzsaki model. In addition to the ion conductance densities, the reversal potentials were also left as free parameters, which helped the filter operate (UKF1 in Table 6). The estimate for g_{NaF} grows without bound and I_{app} retains large transients needed to reproduce the characteristic Hodgkin-Huxley spike. Sample spike waveforms are shown throughout the simulation.
Simulation parameters: sampling rate = 10 kHz, $Q_w = 0.016$

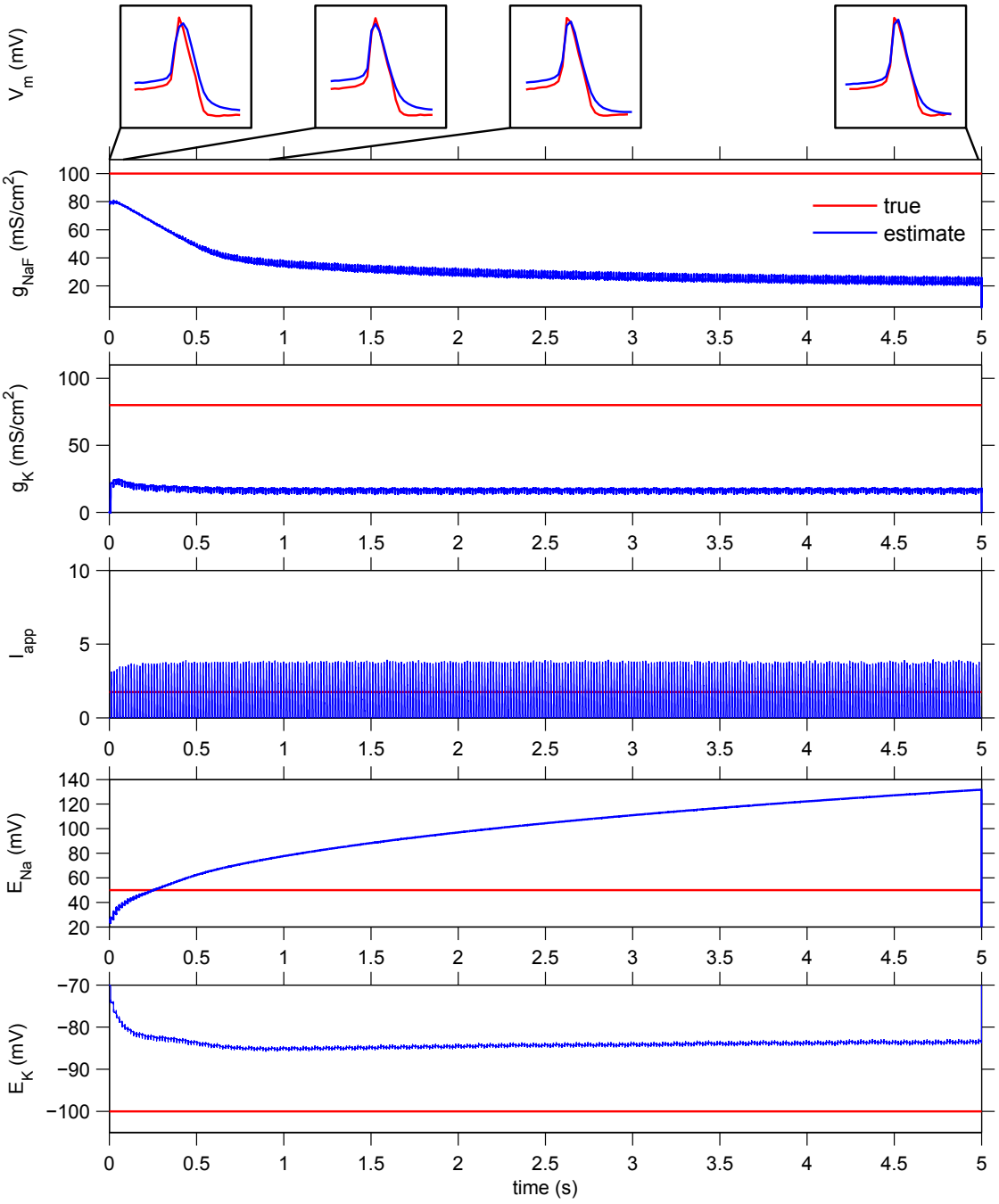

Figure 47: Surrogate data generated using the Hodgkin-Huxley model was fit with a UKF containing a Wang-Buzsaki model. The membrane potential of the Hodgkin-Huxley model was linearly scaled to match the voltage range of the Wang-Buzsaki model. In addition to the ion conductance densities, the reversal potentials were also left as free parameters, which helped the filter operate (UKF2 in Table 6). The estimate for E_{Na} grows without bound. Sample spike waveforms are shown throughout the simulation.
Simulation parameters: sampling rate = 10 kHz, $Q_w = 0.016$

Table 6: Final conductance density estimates when fitting the Hodgkin-Huxley model with a UKF containing a Wang-Buzsaki model after 10 s of simulation time. Parameters that continued to grow without bound are indicated by a "+".

Model	g_{NaF} (mS/cm^2)	g_K (mS/cm^2)	E_{Na} (mV)	E_K (mV)
UKF1, with reversal potentials free	124.1+	22.4	42.4	-120.9
UKF2, also with V_m scaling	22.3	17.0	131.7+	-83.5
UKF3, also with NaF $\alpha_{m_{shift}}$ free	128.5	17.2	47.3	-82.7
Canonical Wang-Buzsaki	35	9	55	-90
Canonical Hodgkin-Huxley	100	80	50	-100

I_{app} retained the oscillations previously seen around the true value though its magnitude was slightly smaller.

A comparison of the parameter values resulting from all these filters with the canonical values for each model is given in Table 6. The final filter produced reversal potentials that were close to typical values. Compared with the canonical Wang-Buzsaki parameter values, the conductance densities were much larger in order to generate the larger peak-to-peak voltages characteristic of the Hodgkin-Huxley spike. The filter also adjusted the kinetic parameter $\alpha_{m_{shift}}$ from 35 to 22.4 mV. This has the effect of shifting the voltage dependence of the sodium channel m-gate to more depolarized values, and in turn, increases the spike threshold. To determine the validity of the parameter estimation, we substituted the final parameter estimates of the last filter (UKF3) back into the Wang-Buzsaki model, using the mean value of the oscillations in I_{app}. The model with these new parameters produced a spike with a higher peak voltage and a deeper afterhyperpolarization (Fig. 48). The increased spike threshold helps shape the voltage trajectory during the interspike interval. When it is scaled in return to match the voltage range of the Hodgkin-Huxley spike, it produces a much closer match to the Hodgkin-Huxley model than the original Wang-Buzsaki model.

While the Wang-Buzsaki and Hodgkin-Huxley model produce different dynamics, they contain only the minimum number of conductance terms required to generate an action potential. In the second example of model order mismatch when using the Kalman filter,

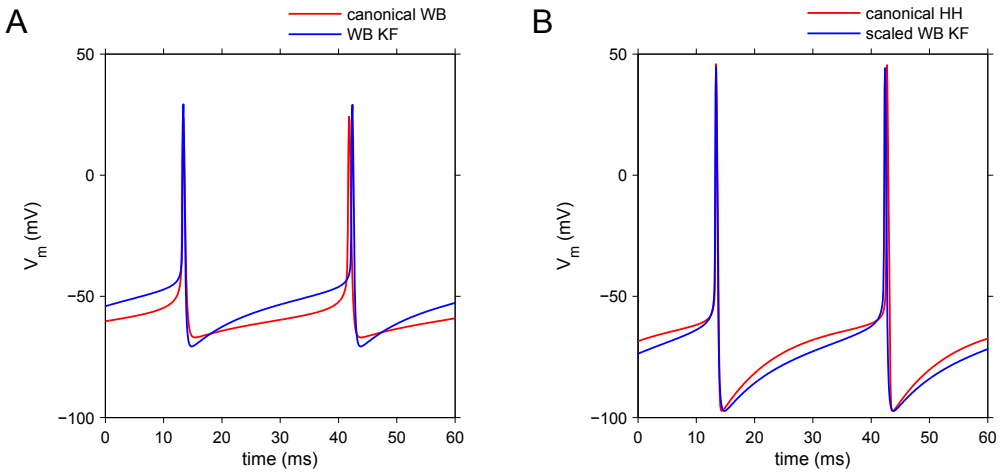

Figure 48: Model reconstruction when using the UKF to fit Hodgkin-Huxley spike with a Wang-Buzsaki model. The input to the filter (UKF3 in Table 6) was the membrane potential output of the Hodgkin-Huxley model scaled to the voltage range of the Wang-Buzsaki model. A) Comparison of original WB spike with spike produced using new parameters. B) Comparison of canonical Hodgkin-Huxley spike with a scaled version of the new WB spike.
Simulation parameters: sampling rate = 10 kHz, $Q_w = 0.016$

we fit the Wang-Buzsaki model parameters to surrogate data generated using the Connor-Stevens model, which has an additional A-type potassium current that is primarily active during the interspike interval. The voltage ranges of a typical Wang-Busaki and Connor-Stevens spike are very similar and no voltage scaling was used. From Fig. 34 we see that the Connor-Stevens model has a sharper afterhyperpolarization, a taller spike, and a more pronounced inflection point in the interspike interval than the Wang-Buzsaki model. By forcing the UKF to follow the membrane potential closely, we cause it to account for these differences by varying the free parameters in the model. The state vector for this filter contains 10 dimensions: $\mathbf{x} = \left[V, m, h, n, a, b, \bar{g}_{NaF}, \bar{g}_K, \bar{g}_{KA}, I_{app}\right]^T$.

Initially, the UKF has difficulty tracking the observed membrane potential accurately (Fig. 49). The first spike is even shorter than the canonical Wang-Buzsaki spike and it is not able to follow the trajectory of the afterhyperpolarization. In fact, to achieve the first spike, the UKF sharply increases g_{NaF} and decreases g_K such that the estimates of g_K actually extend into negative values (Fig. 50). After a few spike cycles have been collected, however, the UKF recovers and does a fairly good job of reproducing the Connor-Stevens spike shape.

The estimates of the conductance densities for the sodium and potassiusm channels do not converge on a single value as shown previously. g_{NaF} appears to approach a value of $\sim$44 mS/cm^2 but there is a transient that is associated with the depolarization leading up to the spike and with the spike itself. This result is a combination of the steady-state approximation for the m-gate for the sodium channel as well as the consequences of the different spike height. When the time-dependence of activation for the sodium channel is removed, the filter may compensate by reducing the amount of sodium conductance slightly just before the spike. However, to match the taller spikes, the filter may need to quickly increase g_{NaF} and decrease g_K simultaneously at the time of the spike. The UKF also sharply increases g_K after the spike to create the afterhyperpolarization.

The estimate for the potassium conductance in the Wang-Buzsaki model shows further interesting dynamics within the interspike interval. In addition to a sharp transient associated with each spike, there also seems to be a slower component within the interspike interval. The transients in g_K indicate that a single potassium channel with fast kinetics is not sufficient to capture the dynamics of the two separate potassium channels that exist in the Connor-Stevens model. From Fig. 40, we see that the A-type potassium channel is primarily active at hyperpolarized potentials with slower time constants than the fast-delayed rectifier. The UKF tries to create the inflection point observed in the Connor-Stevens ISI by continuing to modulate g_K. While the general shapes of the fast and slow components in the transients in g_K exist for a range of Q_w, the magnitudes of each component depend on its specific value. Increasing the value of Q_w further results in an estimated trajectory for V_m that matches the observed values even more closely. However, this also increases the fluctuations in the estimates for g_{NaF} and g_K more. Carefully tuning the value of Q_w reveals that while the model for the sodium channel may be approximately correct (in that g_{NaF} may be treated as a constant parameter), the model for the potassium channel is not.

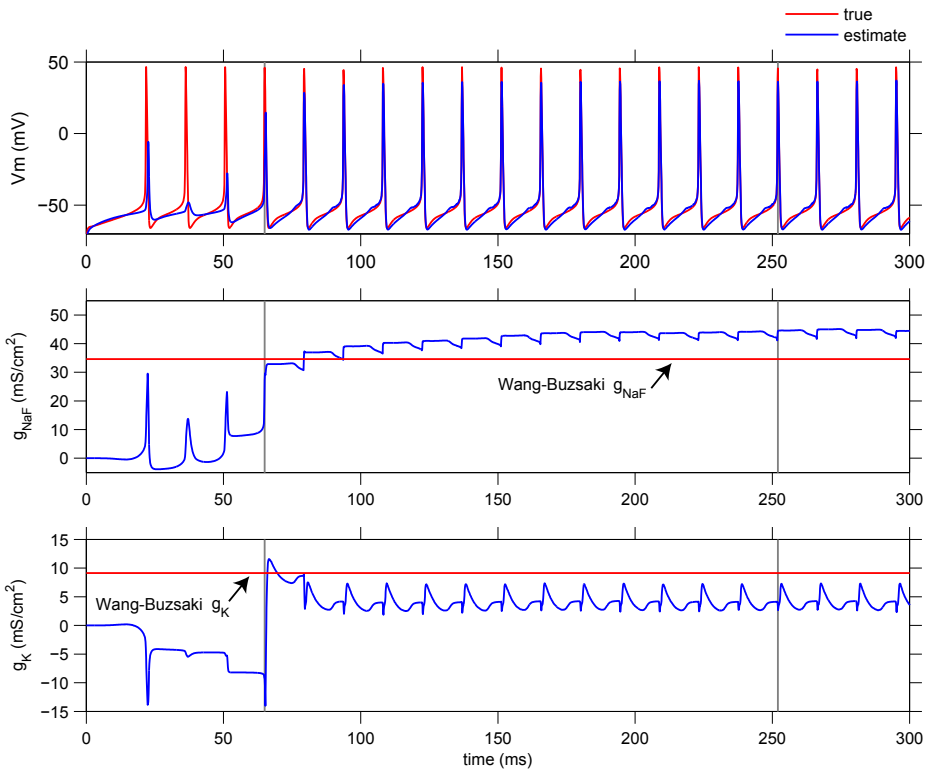

Figure 49: Surrogate data generated using the Connor-Stevens model was fit with a UKF containing a Wang-Buzsaki model (vertical line indicates the spike time for reference to Fig. 50). The mismatch between the models results in estimates for the maximal ionic conductances that do not converge on a single value. Simulation parameters: sampling rate = 10 kHz, $Q_w = 0.020$

5.2.5 Estimation of time-varying external conductances

We previously showed that the UFK can distinguish between conductance-based mechanisms of spike generation and an applied current as well as distinguish between two membrane conductances with different kinetics. In this section, we modify the Kalman filter to include the external conductance input to the neuron model. The conductance-based membrane equation can be written in terms of the intrinsic ion channels and synaptic input:

$$C_m \frac{dV_m}{dt} = -\sum \left\{ g_i(t)(V_m - E_i) \right\} + g_{ex}(t)(V_m - E_{ex}) + g_{in}(t)(V_m - E_{in}) \qquad (33)$$

Given a known model, the UKF could be used to estimate changes in $g_{ex}(t)$ and $g_{in}(t)$, the time-varying excitatory and inhibitory synaptic inputs. Similar to the problem of estimating the model parameters, there is no model describing how the conductances change in time.

Surrogate data for this simulation was generated by applying fixed external excitatory

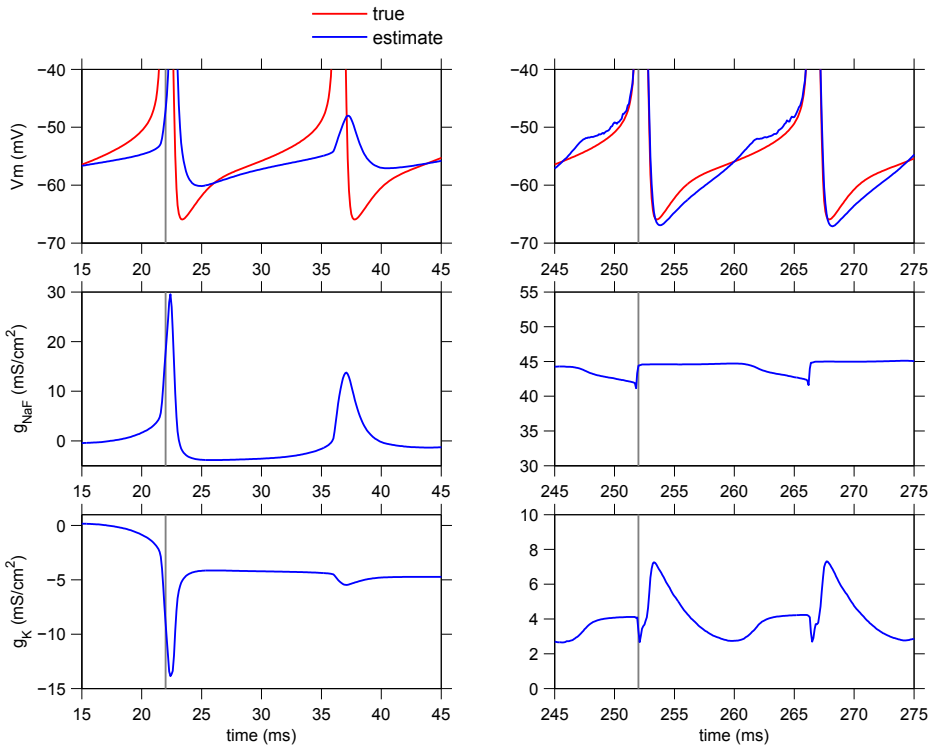

Figure 50: Surrogate data generated using the Connor-Stevens model was fit with a UKF containing a Wang-Buzsaki model (vertical line indicates the spike time for reference to Fig. 49). The first spike is shown on the left, and a later spike is shown on the right.
Simulation parameters: sampling rate = 10 kHz, $Q_w = 0.020$

and inhibitory conductance waveforms to the Hodgkin-Huxley model neuron. The reversal potentials were set to 0 mV and -90 mV for excitation and inhibition, respectively. The conductance waveforms were constructed by modeling 150 inhibitory GABA-type synapses and 90 excitatory AMPA-type synapses. The synapses were activated randomly according to independent Poisson processes with mean rates of 2.4 Hz for the inhibition and 2.16 Hz for excitation [213]. The inhibitory synapses were modeled with a rise time constant of 0.93 ms and a decay time constant of 13.6 ms. The excitatory synapses were modeled with a rise time constant of 0.5 ms and a decay time constant of 1.2 ms.

These synaptic parameters resulted in a balanced level of inhibition and excitation that led the model to spike irregularly at an average spike rate of 100 Hz (Fig. 51). The state vector for this filter contained 8 dimensions: $\mathbf{x} = \left[V, m, h, n, \bar{g}_{NaF}, \bar{g}_K, g_{inh}(t), g_{exc}(t)\right]^T$. The UKF is able to accurately track the membrane potential and ion channel activation

variables after ∼1.2 seconds of collecting information (Fig. 51). During this initial period, the synaptic conductances are overestimated in an attempt to reproduce the spike waveform. The estimates of the ion channel conductance densities do not converge until ∼30 s. When the values of g_{NaF} and g_K are sufficiently close to their true values (within 5 mS/cm^2), the UKF is able to track the external excitatory and inhibitory conductance (Fig. 52). Until this point, however, the magnitudes of the external conductances estimates are incorrect, although their qualitative dynamics are similar to the true conductance waveforms. In these simulations, the UKF did produce negative values for its estimates of the external conductances. Constraining the filter to remap these estimates to positive values, or simply to replace them with a value of zero, only slightly improved its performance and the rate at which it converged to the true parameter values. In these simulations, while I_{app} was not included as a free parameter, the filter could have easily manipulated the external conductances to produce the spikes. Not only does it distinguish between intrinsic and synaptic conductances, it distinguishes between excitation and inhibition based only on their different reversal potentials.

The UKF is able to track the excitatory conductance more accurately than the inhibitory conductances. While the estimate inhibitory conductance looks like a low-pass filtered version of the true waveform, the Kalman filter can extract the time courses of individual synaptic activations. These are visible in Fig. 52 because the excitatory input rate is slower than the inhibitory input rate and individual excitatory events can be distinguished. In contrast, the UKF is only able to qualitatively follow the inhibitory conductance waveform and misses some large fluctuations (eg. around t = 29.3 s). The accuracy of the UKF for each input stream was quantified by computing the cross-covariances between the true conductance waveforms and the estimates produced by the filter (Fig. 53). The cross-correlogram for the excitatory conductance shows a much more prominent central peak with a maximum value of 0.94 compared to 0.64 for the inhibitory conductance. Even the rough estimate of inhibitory conductance is useful here because it can be used to construct continuous estimates of the mean levels of inhibition and excitation without perturbing the cell with other stimuli.

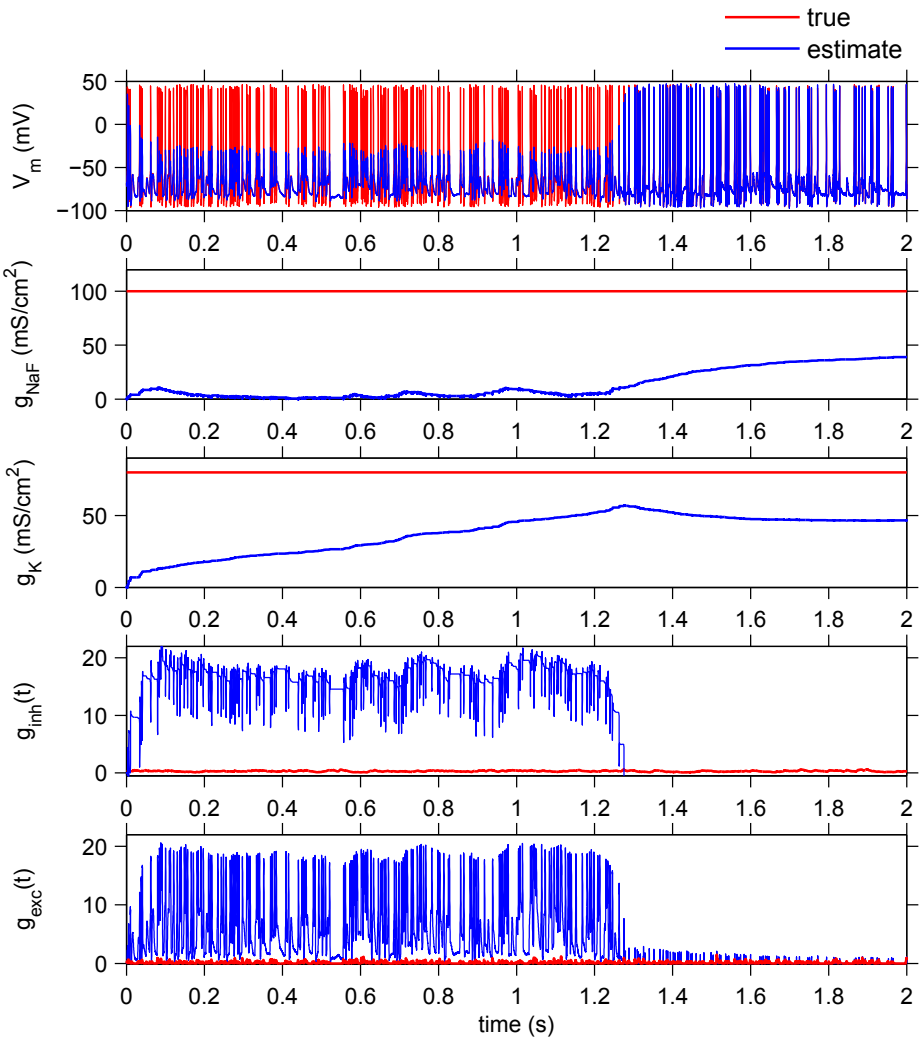

Figure 51: Estimating external excitatory and inhibitory Poisson conductance inputs to the Hodgkin-Huxley model. The UKF is able to accurately track the membrane potential and ion channel activation variables after ∼1.2 seconds of collecting information.
Simulation parameters: sampling rate = 10 kHz, $Q_w = 0.016$

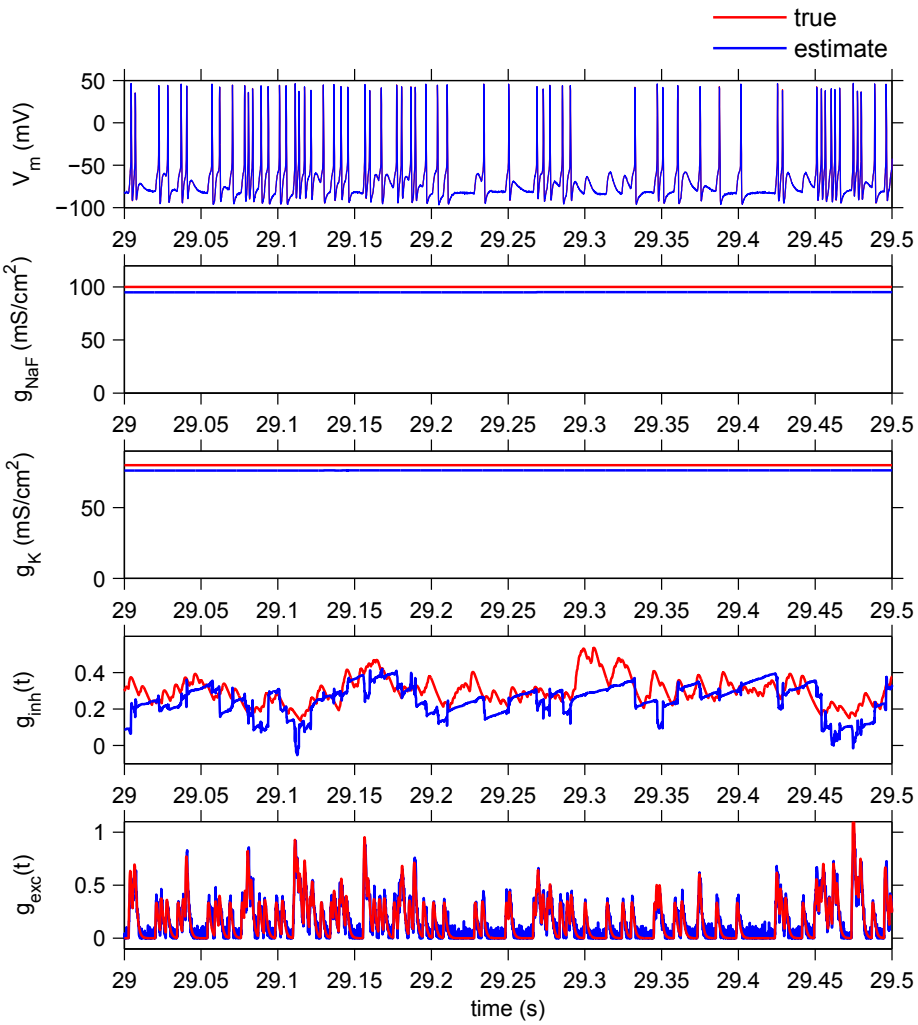

Figure 52: Estimating external excitatory and inhibitory Poisson conductance inputs to the Hodgkin-Huxley model. When the values of g_{NaF} and g_K are sufficiently close to their true values (within 5 mS/cm^2), the UKF is able to track the time-varying external conductances.
Simulation parameters: sampling rate = 10 kHz, $Q_w = 0.016$

A spike-triggered average of the excitatory and inhibitory conductance in a window of time around each spike shows that the Hodgkin-Huxley model spikes preferentially to a transient depolarizing fluctation in excitation. On average, the excitatory conductance increases to ∼2.5X that of its mean value immediately before a spike while the inhibitory conductance is relatively flat around each spike. Since the membrane potential is the only information that the filter observes and the inhibitory input places a minimal role during the spikes, there is very little relation between the dynamics of the membrane potential and the inhibitory input. One reason for this is that the driving force for excitation is so much larger than for inhibition in this simulation; the average subthreshold membrane potential for the Hodgkin-Huxley neuron is approximately -75 mV. Other techniques report a similar difficulty in extracting inhibitory presynaptic input at physiological resting potentials [182] or when the variance in one conductance input stream is much higher than in the other [188]. In the latter study, the firing activity of neurons in a high conductance state were driven by fluctuations in the membrane potential caused by synaptic input rather than a depolarized average voltage. The success of this technique in extracting the time course of synaptic input for different neuron types will depend on what membrane mechanisms dominate their subthreshold dynamics.

5.3 Discussion

5.3.1 Validity of the Kalman filter assumptions

A fundamental assumption of the Kalman filter is that the distribution of the system states can be described by a normal distribution. The membrane potential has been shown to have a normal distribution under certain conditions, specifically in the high conductance state for cortical neurons during which thousands of synaptic inputs are bombarding the membrane per second [66]. The gating variables for each ion channel, however, are restricted to values between 0 and 1 and are not described by a normal distribution. The Kalman filter also assumes that the noise inherent in the system and the measurement noise can be well-described as Gaussians and are uncorrelated. For a real experiment this is generally not true due to various hardware that may introduce correlations or other biases into the signals.

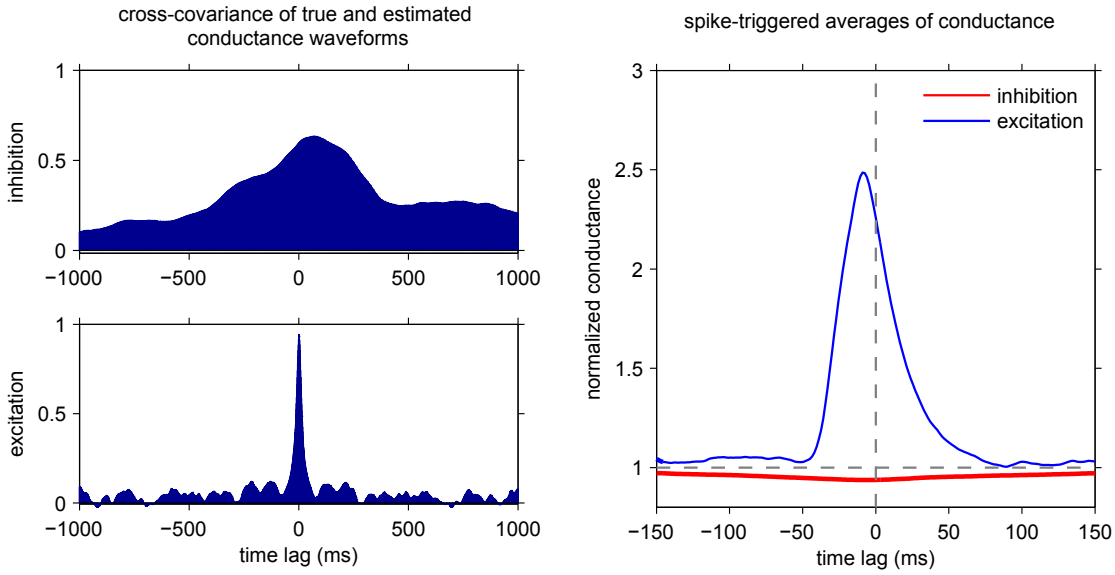

Figure 53: The cross-covariances between the true conductance waveforms and the estimates produced by the filter were computed for the simulation shown in Figs. 51 and 52. The spike-triggered conductances are normalized to a value of one based on the mean inhibitory or excitatory conductance level.

Despite the violations of these assumption, the greatest challenge is finding appropriate neuron models to embed in the Kalman filter.

The results of parameter estimation will depend on the amount of noise, or uncertainty, that is injected for that term on each time step. This allowed variability can be quite large as shown in database approaches to neuron model construction [198]. Similarly, the efficacy of the filter also depends on the reliability of the "measurements." This will be assessed by separately systematically increasing the amount of process and measurement noise. It is not expected that the amount of noise that will numerically allow the Kalman gain to converge will match the amount of noise in the actual system or in the measurements. A greater amount of noise may be needed to compensate for model order mismatch.

For the Kalman filter, usually Gaussian white noise is simply added to each state estimate. For the neuron models used here, this is equivalent to the stochastic differential equations base on subunit noise developed by Fox and Lu and described in Section 3.4.3 in which noise is added to each subunit in the Hodgkin-Huxley equations (Eqn. 15). However,

simulations have shown that actually adding fluctuation in conductance terms, or equivalently in the fractions of open channels, should be the preferred way for including channel noise [91, 92]. Using Markov chain models as the gold standard, conductance-based rather than subunit noise produces more accurate statistics (mean and CV) of the interspike intervals as well as the fractions of open channels. While this approach is computationally simple, solving stochastic Hodgkin-Huxley type differential equations for sufficient numbers of channels may not be feasible in real-time at the necessary sampling rates.

5.3.2 Performance of the UKF in state and parameter estimation for neuron models

Our results reproduce previous work demonstrating that the the UKF can successfully reconstruct the states and parameters of a known model. It performs well when the input to the filter is extremely nonstationary, such as with irregular spiking, and can handle realistic levels of measurement noise that would be encountered during experiments. As such, it could be used as a model-fitting algorithm as well as a means for generating a command signal for a model-based control protocol. For parameter estimation, a recursive technique like the UKF provides more information than simply the final suggested value. The dynamics of how the filter converges on a final value indicates which membrane mechanisms are dominant in different regions of the spike cycle. For example, during the interspike interval, the membrane potential is relatively stationary and outside the active voltage ranges of the fast sodium and potassium channels so that not much new information is gained. Consequently, the estimates produced by the filter for these conductances do not vary much during the ISI.

The ability of the filter to produce a membrane potential output that closely tracks the observed voltage is not a good indicator of the quality of the estimates for the underlying states and variables. In general, the spike waveform is successfully reproduced well before the parameter estimates have converged. For the models used in this study, these estimates converged within 15 s of simulation time, or equivalently at $\sim$900 spikes since the models were driven to spike at 60 Hz. In comparison, regular spiking cortical neurons typically fire around 10 Hz though some fast spiking neurons can reach rates up to several hundred hertz

[177]. For slowly spiking neurons, a much longer convergence time would be expected and may actually be comparable to offline automated model-fitting algorithms. The benefit of an online method, however, is that it is continuously updated and changes in the parameter estimates throughout the course of the experiment may provide quantitative information about changes in the cell's properties over long time scales. An important difference between model-fitting using a recursive algorithm and typical approaches based on matching the spike shape is that the UKF can handle both irregular and regular spiking activity and does not need to use the spike rate as a target feature. The current-voltage relationship or f-I curve is one of the most common metrics for validating neuron models. The UKF simultaneously matches the spike shape and spike frequency without perturbing the neuron.

The actual implementation of the unscented Kalman filter for online parameter fitting and state tracking in real experiments is limited by the computational demands of the algorithm. The unscented transformation generates $2n$ points in the system's state space and propagates each point through the full model equations. The largest state vector used in the simulations described here had 10 dimensions so that on each cycle, the algorithm numerically integrated 20 models and performed a Cholesky factorization on a 10-dimensional matrix. A UKF module was developed for RTXI based on the GNU Scientific Library (GSL, http://www.gnu.org/software/gsl/), a open-source C++ collection of numerical routines for scientific computing. Rather than compute a matrix inversion, Eqn. 30 is implemented using a singular value decomposition and the sigma points are generated using the library's default Cholesky decomposition function. This module can execute the UKF algorithm on a 5-dimensional state vector at a sampling rate of 8 kHz, which in our simulations, was sufficient for good convergence of the filter. The performance of the filter might be improved by using different numerical libraries. The GSL library is a pre-compiled, easy-to-use cross-platform library based on the default CBLAS library. CBLAS can be replaced by ATLAS, a machine-specific tuned library that provides optimal linear algebra software for different processor architectures. Another option is to use the Linear Algebra PACKage (LAPACK, http://www.netlib.org/lapack/) or the Class Library for High Energy Physics (CLHEP, http://proj-clhep.web.cern.ch/proj-clhep/). LAPACK is generally at least several

times faster than the GSL library and since it is recompiled with the executable, it takes advantage of compiler optimizations. For state vectors that are 6 dimensions or smaller, CLHEP offers further speed improvements since it uses hand-optimized algorithms for small matrices. While other dynamic clamp systems could implement the UKF algorithm, RTXI should provide the best performance because it has lower overhead since it is based on the Linux OS and has a modular architecture that links only the necessary shared libraries at runtime. Furthermore, this architecture allows for memory allocation on the stack rather than on the heap since the size of the required matrices can be predefined and no dynamic allocation is necessary.

Numerically integrating the model equations is relatively straightforward and the same heuristics that apply to choosing a sampling rate for dynamic clamp applies to integrating the models embedded inside the Kalman filter. Dynamic clamp sampling rates are currently chosen based on the limits of the hardware platform being used and the temporal dynamics being simulated. While it is possible to compute the time step necessary for the Euler and exponential Euler methods to achieve a desired one-step integration accuracy for a known voltage measurement error, few studies employ this technique [35]. In simulations of dynamic clamp, Euler integration was insufficient to model fast sodium Na_v channels at sampling rates under 30 kHz and nearly identical integration results for three different deterministic integration methods was only achieved at rates $\geq$50 kHz [167]. In these simulations, both the Euler method and the 4th order Runge-Kutta method were tested. Euler integration is commonly used in dynamic clamp experiments at sampling rates as low as 4-5 kHz. While it is $\sim$4X faster than the RK4 method, it can only be used at small enough time steps. In several simulations, a filter that did not converge using the Euler method did converge using the RK4 method at the same sampling rate. Given the additional overhead of the Kalman filter calculations, for high-dimensional models, switching to a higher order integration method embedded in the filter may be more advantageous than increasing the sampling rate. An alternative solution is to subdivide each Kalman filter cycle and numerically integrate the equations using the Euler method multiple times on each cycle.

5.3.3 Online model discrimination and hypotheses testing

It is expected that the greater the difference between the model embedded in the Kalman filter and the actual data to be fitted, the worse the filter will perform. We saw numerous cases in which the filter failed to track the membrane potential entirely or arbitrarily adjusted the underlying state variables and parameters to produce the correct output. This problem is commonly tackled by increasing the uncertainty in the model by increasing the process noise Q_w. Another approach is to add an arbitrary term to the membrane equation, which would not necessarily correspond to any biophysical process but may promote a better fit to the data. While the UKF did not result in a viable parameter set for describing the Connor-Stevens dynamics with the Wang-Buzsaki model, it did produce useful results for evaluating the appropriateness of Wang-Buzsaki and even suggested in what ways it could be modified. We have already seen that the dynamics of the filter output reveal which conductance terms play a dominant role in certain phases of spiking activity and when additional conductance terms may be needed. This kind of information is not available from the previously described model-fitting techniques that use global error measures that do not capture the time-varying dynamics of the system.

While it will certainly always be the case when using this technique that the filter simplifies the dynamics of the real cell, it may be possible to perform model selection online given a broad set of functional classes of ion channels. Minimal models for spiking and bursting neurons have already been developed that can describe a wide range of neuronal responses using common ion channel types [86, 190]. In general, a globally reduced model does not produce the best approximation to a transient feature in a neuron's activity but a Kalman filter approach can identify temporal intervals in which certain dynamics play an important role. The dynamics of the parameter estimates produced by a filter may also indicate when a model is insufficient and reveal quantitative suggestions for how to adjust it. This information would also be useful in the development of hybrid dynamical systems in which a differential equation describing the full dynamics of a process may be replaced with a simpler piecewise function. Rather than adding conductance mechanisms with arbitrary kinetic schemes, the user can form mechanistic hypotheses without making

explicit assumptions about the form of the model equations. It has been shown that locally reduced hybrid models can still exhibit the same modes of activity as a full model of a bursting neuron [45–47]. These lower dimensional models are more amenable to approaches such as bifurcation analysis and are important tools for testing mechanistic hypotheses about complex neural responses.

An interesting feature of the filtering approach is that multiple Kalman filter with different embedded models can be implemented in parallel. Since the Kalman filter produces estimates of the error in each state variable as well, this approach also serves as an online hypothesis-testing method with little additional computational overhead. While each filter may produce output that closely tracks the same observed state, they may produce very different error bounds for the state estimates. The filter with the lowest error presumably contains the model that best describes the observed data. This approach has seen increasing interest in systems biology where it is used to evaluate the fitness of models describing the topology of biochemical pathways, reaction kinetic schemes, and parameter values [130, 142, 158, 248]. An extension of this method is that coupled with a maximization algorithm, it can be used to dynamically determine the optimal stimuli to the system that maximizes the difference between each filter's output and allows model discrimination with greater confidence. In systems biology, observations from these systems are generally discrete measurements of biomass and substrate concentrations at much lower sampling rates than those discussed in this study. Sequential optimal design of neurophysiology experiments is still relatively new and has been primarily focused on improving the efficiency of experiments investigating receptive fields based on spike rate and spike time responses [154, 155]. In sensory physiology, model discrimination has been performed using the iso-response or stimulus reconstruction methods [20, 71]. Instead of a standard input-output experimental procedure and comparing it with the predictions of the different models, we can identify the optimal stimuli that correspond to a specified response. This stimuli is then injected back into competing models and the output is used to evaluate their fitness.

5.3.4 Dynamic clamp and model-based real-time control algorithms for biological experiments

In neural electrophysiology, the dynamic clamp is a first step towards introducing the principle of model-based control to biological applications. However, it is common to use the same ion channel model and parameters in a dynamic clamp experiment without taking into account the intrinsic biological variability between multiple cells and multiple animals. The parameters for these models are generally determined by averaging over experimental results from yet a different set of preparations. Furthermore, multiple system components are often technically not able to be measured in the same preparation. It has been shown in simulations of conductance-based neurons that averages over multiple samples can fail to describe a system whose behavior depends on the interactions between highly variable components [93]. Simply knowing the mean and variance of typical parameter measurements only captures the variability of linear combinations of parameters that are assumed to be independent. While these can provide useful heuristics for producing desired responses [120, 227], low-order statistical measures generally do a poor job of defining the boundary of a multi-dimensional region. A method that can simultaneously fit relevant parameters online for each preparation allows the experimenter to automatically capture the variability of multiple components and optimize the model used in the dynamic clamp for that same cell.

Since the Kalman filter is a recursive technique that generates predictions of the system's behavior, it is also a candidate for generating control signals to change that behavior. These model-based techniques can simultaneously provide information about the system that cannot be directly measured and guidelines for online feedback during an experiment. Model reference control is commonly used in industry for applications such as supply chain management, automotive control, and flight control in aviation. Rather than generating control signals that are derived directly from noisy observed data, the signal can be generated from estimates of state variables in a model of how that system behaves. In neural electrophysiology, these could be quantities that are difficult to experimentally measure continuously or accurately at the required time scales. For example, in the context of dynamic clamp,

an artificial calcium- and voltage-dependent conductance could be created that incorporates details of how intracellular calcium levels are affected by other activity-dependent processes. This framework has the advantage that the control signal is determined from a more complete description of the system's dynamics combined with a strategy for handling uncertainty in the model and in the measurements.

In combination with standard minimization and/or closed-loop feedback techniques, model reference control can also be used to drive the system on a specific target trajectory or towards a target value by using the result of the Kalman filter prediction step to compute a feedback signal. Control-based approaches are not common in biological applications for several reasons. Until recently, we lacked sufficiently accurate computational models of the biological system. The models that do exist have extremely nonlinear dynamics and most control engineering approaches depend on the ability to linearize a system. Some of these methods are too computationally inefficient for real-time observation and control. Finally, implementing these approaches has been difficult due to a lack of experiment platforms and actuators that can accommodate acquisition and control of biological signals in real-time with the required spatial and temporal resolutions for different modalities [151]. While a control algorithm using a deterministic model relies on multiple simultaneous measurements from the system, the Kalman filter can be formulated to infer the states of the model in between potentially asynchronously sampled measurements. This framework may provide more control points for regulating the system and bring the technical requirements of control-based approaches in biology into realistic range.

5.4 Acknowledgments

Sample code for the UKF was made available by Henning Voss from his 2004 paper in which he used the Fitzhugh-Nagumo model to demonstrate the technique [253]. I modified this code in MATLAB based on suggestions in published papers by Steven Schiff [218, 243]. I performed all simulations and data analysis in this section.

APPENDIX A

DEEP CEREBELLAR NEURON MODEL

A.1 Channel Kinetics

All channel conductances are modeled based on the Hodgkin & Huxley (1952) formalism and calculated as the product of a maximal conductance $\bar{g}_i$ and voltage- or calcium-dependent activation and inactivation variables m, h and z:

$$I_i = g_i(V_m)(V_m - E_i) \tag{34}$$

$$g_i(V_m) = \bar{g}_i m^{\mathrm{p}} h^{\mathrm{q}} \tag{35}$$

The temporal evolution of all activation and inactivation variables $x = \{m, h, z\}$ is determined by their steady state values x_∞ and their time constants τ_x:

$$\frac{dx}{dt} = \frac{x_\infty(V_m) - x}{\tau_x(V_m)} \tag{36}$$

For all voltage-gated channels, the voltage dependences of the steady state activation and inactivation variables $x_\infty = \{m_\infty, h_\infty\}$ are represented by Boltzmann functions:

$$x_\infty = \frac{1}{1 + \exp\left[\frac{V_m - V_h}{k}\right]} \tag{37}$$

Where indicated, the time constants for activation and inactivation are described by:

$$\tau_x = \frac{A}{\exp\left[\frac{V_m - B}{C}\right] + \exp\left[\frac{V_m - D}{E}\right]} + F \tag{38}$$

All equations are for 32°C.

A.1.1 Fast sodium current NaF

$$I_{NaF} = \bar{g}_{NaF} m^3 h s (V_m - E_{Na}) \tag{39}$$

with E_{Na} = 71 mV.

Activation m: V_h = -35 mV, k = -7.3 mV. The activation time constant is voltage independent and given by τ_m = 0.025 ms.

Inactivation h: V_h = -32 mV, k = 5.9 mV. The inactivation time constant τ_h also follows Eqn. (38), with A = 25 ms, B = 23.3 mV, C = -29 mV, D = -51 mV, E = 9 mV and F = 0.3 ms.

Slow inactivation s: The inactivation variable is described by:

$$s_\infty = s_{min} \frac{1 - s_{min}}{1 + \exp\left[\frac{V_m - V_0}{k_s}\right]} \tag{40}$$

where s_{min} = 0.50, V_0 = -40 mV, and k_s = 5.4 mV. The slow inactivation time constant is described by:

$$\tau_s = \tau_{smin} + \frac{\tau_{smax} - \tau_{smin}}{\exp\left[\frac{V_0 - V}{k_1}\right] + \exp\left[\frac{V_m - V_0}{k_2}\right]} \tag{41}$$

where τ_{smin} = 70 ms, τ_{smax} = 1 s, V_0 = -40 mV, k_1 = 18.3 mV, and k_2 = 10 mV.

A.1.2 Persistent sodium current NaP

$$I_{NaP} = \bar{g}_{NaP} m^3 h (V_m - E_{Na}) \tag{42}$$

with E_{Na} = 71 mV.

Activation m: V_h = -65 mV, k = -4.1 mV. The activation time constant is voltage independent and given by τ_m = 0.3 ms.

Inactivation h: V_h = -75 mV, k = 5 mV. The inactivation time constant is described by:

$$\tau_h = \frac{1750 \text{ ms}}{1 + \exp\left[\frac{V_m + 60 \text{ mV}}{-8 \text{ mV}}\right]} + 250 \text{ ms} \tag{43}$$

A.1.3 High voltage activated calcium current CaHVA

The current through high voltage activated calcium channels is modeled by the Goldman-Hodgkin-Katz equation:

$$I_{CaHVA} = \bar{p}_{CaHVA} m^3 \frac{z^2 F^2 V_m}{RT} \frac{[Ca^{2+}]_i - [Ca^{2+}]_0 \exp\left[\frac{-zFV_m}{RT}\right]}{1 - \exp\left[\frac{-zFV_m}{RT}\right]} \tag{44}$$

where $\bar{p}_{CaHVA}$ is the maximum Ca^{2+} permeability, $z = 2$ is the valency of Ca^{2+}, $R = 8.3145$ J K^{-1} mol^{-1} is the gas constant, $F = 96480$ C mol^{-1} is the Faraday constant and T is the thermodynamic temperature in K. The voltage dependence of the activation variable m is described by a Boltzmann function (Eqn. 37) with V_h = -24.5 mV and k = -9 mV, and the activation time constant is given by:

$$\tau_m = \frac{1 \text{ ms}}{31.746(\exp\left[\frac{V_m - 5}{-13.89}\right] + 1)^{-1} + 3.97 * 10^{-4}(V_m + 8.9)(\exp\left[\frac{V_m + 8.9}{5}\right] - 1)} \tag{45}$$

A.1.4 Low voltage activated calcium current CaLVA

$$I_{CaLVA} = \bar{g}_{CaLVA} m^2 h (V_m - E_{Ca}) \tag{46}$$

with $E_{Ca} = 139$ mV.

Activation m: V_h = -56 mV, k = -6.2 mV. The activation time constant τ_m is described by Eqn. (38) with $A = 0.333$ ms, B = -131 mV, C = -16.7 mV, D = -15.8 mV, E = 18.2 mV and $F = 0.204$ ms.

Inactivation h: V_h = -80 mV, $k = 4$ mV. The inactivation time constant is given by

$$\tau_h = \begin{cases} 0.333 \text{ ms} * \exp\left[\frac{V_m + 466 \text{ mV}}{66 \text{ mV}}\right] & \text{for} \quad V_m < -81 \text{ mV} \\ 0.333 \text{ ms} * \exp\left[\frac{V_m + 21 \text{ mV}}{-10.5 \text{ mV}}\right] + 9.32 \text{ ms} & \text{for} \quad V_m \geq -81 \text{ mV} \end{cases} \tag{47}$$

A.1.5 Tonic non-specific cation current TNC

This is a mixed cation current with a reversal potential E_{TNC} = -35 mV and a voltage independent conductance:

$$I_{TNC} = \bar{g}_{TNC}(V_m - E_{TNC}) \tag{48}$$

A.1.6 Hyperpolarization activated HCN current

$$I_h = \bar{g}_h m^2 (V_m - E_h) \tag{49}$$

with E_h = -45 mV.

Activation m: V_h = -80 mV, k = 5 mV, τ_m = 400 ms.

A.1.7 Fast delayed rectifier fKdr

$$I_{fKdr} = \bar{g}_{fKdr} m^4 (V_m - E_K) \tag{50}$$

with E_K = -90 mV.

Activation m: V_h = -30 mV, k = -7.8 mV, τ_m given by Eqn. (38) with A = 13.9 ms, B = -30 mV, C = 12 mV, D = -30 mV, E = -13 mV, F = 0.1 ms.

A.1.8 Slow delayed rectifier sKdr

$$I_{sKdr} = \bar{g}_{sKdr} m^4 (V_m - E_K) \tag{51}$$

with E_K = -90 mV.

Activation m: V_h = -40 mV, k = -9.1 mV, τ_m given by Eqn. (38) with A = 14.95 ms, B = -40 mV, C = 21.74 mV, D = -40 mV, E = -13.91 mV, F = 0.05 ms.

A.1.9 Small conductance calcium-dependent potassium current SK

$$I_{SK} = \bar{g}_{SK} z (V_m - E_K) \tag{52}$$

with E_K = -90 mV.

The calcium-dependent activation variable z is given by:

$$z_\infty = \frac{[Ca^{2+}]^4}{[Ca^{2+}]^4 + (3 * 10^{-4}\ \text{mM})^4} \tag{53}$$

The calcium dependence of the activation time constant is described by:

$$\tau_z = \begin{cases} 60\ \text{ms} - 11.2 * 10^3\ \text{ms mM}^{-1}[Ca^{2+}] & \text{for} \quad [Ca^{2+}] < 0.005\ \text{mM} \\ 4\ \text{ms} & \text{for} \quad [Ca^{2+}] \geq 0.005\ \text{mM} \end{cases} \tag{54}$$

A.1.10 Calcium concentration

We assume that the SK channel is selectively activated by calcium ions that enter the cell through CaHVA channels, and calculate the effective calcium concentrations using a simple phenomenological model:

$$\frac{d[Ca^{2+}]}{dt} = BI_{CaHVA} - \frac{[Ca^{2+}] - [Ca^{2+}]_{base}}{\tau_{Ca^{2+}}} \tag{55}$$

where $[Ca^{2+}]_{base}$ = 50 nM is the baseline calcium concentration, $\tau_{Ca^{2+}}$ = 70 ms is the decay time constant and $B = k_{Ca^{2+}}/v_{shell}$ is a free parameter that scales inversely with the volume of a hypothetical submembrane shell with a thickness of 200 nm. Tuning the model resulted in $k_{Ca^{2+}}$ = 3.45 x 10^{-7} mol C^{-1} in the soma and $k_{Ca^{2+}}$ = 1.04 x 10^{-6} mol C^{-1} in the dendritic compartments.

A.2 Channel conductance densities

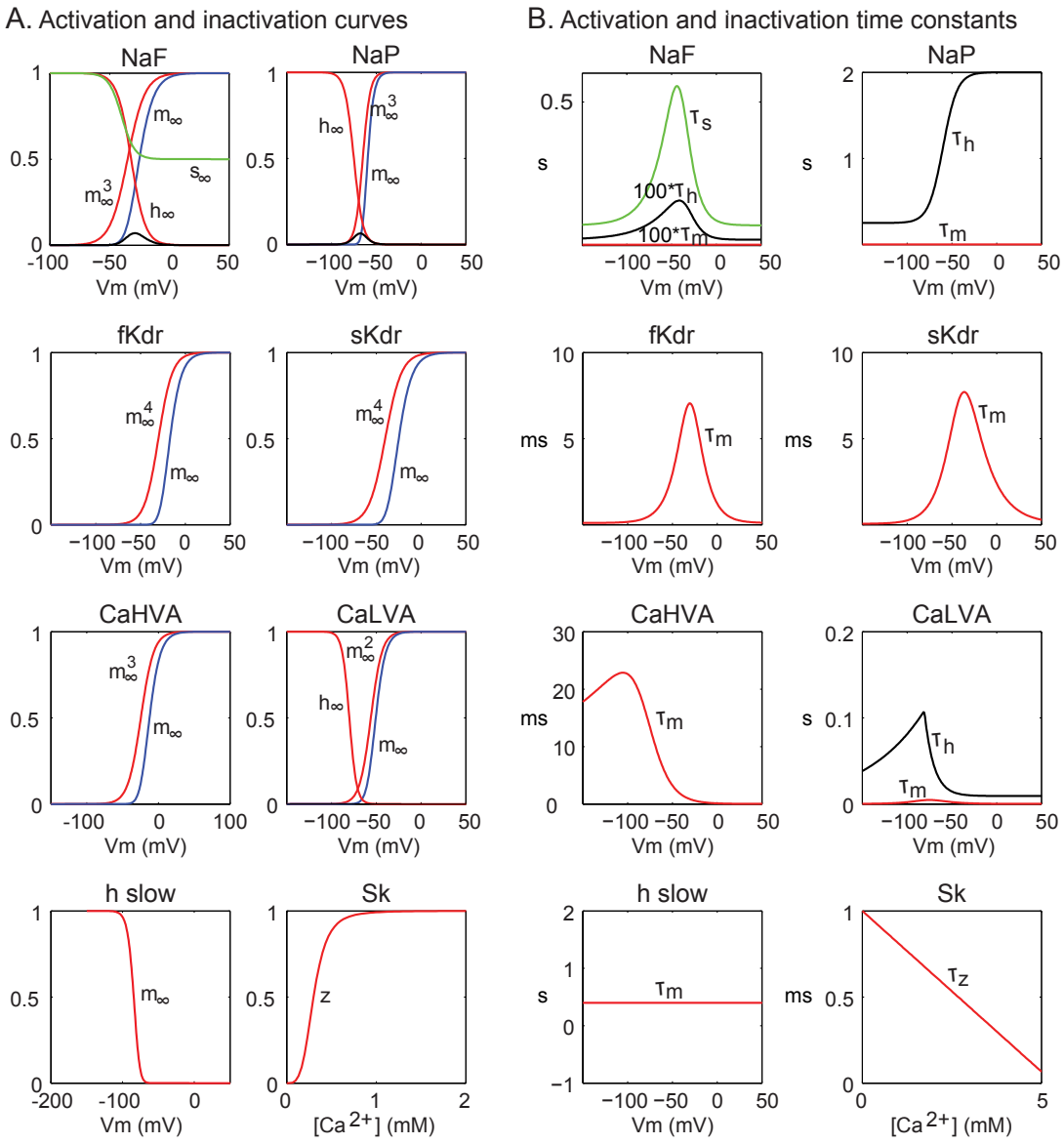

Figure 54: A) Steady-state voltage and calcium dependencies of activation and inactivation for the membrane conductances. B) Voltage and calcium dependencies of activation and inactivation time constants.

Table 7: Channel conductance densities in S/m^2 (and for CaHVA, permeability in m/s) for the different compartment types in the DCN model. Axon refers to the conductance densities and CaHVA permeability in the axon hillock and initial segment.

Section	NaF	fKdr	sKdr	TNC	SK	CaHVA	CaT	NaP	IH
Soma	330	150	90	0.09	2	7.5e-8	0.6	2	1.5
Proximal Dendrite	33	45	27	0.018	0.6	5e-8	0	0	0
Distal Dendrite	0	0	0	0	0.6	5e-8	0	0	0
Axon	495	300	270	0.12	0	0	0	0	0

APPENDIX B

KALMAN FILTER EQUATIONS

B.1 Kalman filter equations for a linear system

Table 8: The discrete Kalman filter for a linear state space model. $P(n)$ are the error covariance matrices and Q_w and Q_v are the covariance of the model noise process, $w(n)$, and measurement noise process, $v(n)$. $w(n)$ and $v(n)$ are uncorrelated Gaussian processes with zero mean. Adapted from Hayes 2006 [105].

State Equation:	$x(n) = A(n-1)x(n-1) + w(n)$
Measurement Equation:	$y(n) = C(n)x(n) + v(n)$
Initialization:	$\hat{x}(0\|0) = E\{x(0)\}$
	$P(0\|0) = E\{x(0)x^H(0)\}$
Computation:	For n=1,2,...
	$\hat{x}(n\|n-1) = A(n-1)\hat{x}(n-1\|n-1)$
	$P(n\|n-1) = A(n-1)P(n-1\|n-1)A^H(n-1) + Q_w(n)$
	$K(n) = P(n\|n-1)C^H(n)\left[C(n)P(n\|n-1)C^H(n) + Q_v(n)\right]^{-1}$
	$\hat{x}(n\|n) = \hat{x}(n\|n-1) + K(n)\left[y(n) - C(n)\hat{x}(n\|n-1)\right]$
	$P(n\|n) = \left[I - K(n)C(n)\right]P(n\|n-1)$

B.2 Unscented Kalman filter equations for a nonlinear system

The discrete Kalman filter gives the optimal recursive estimate of the system states in a least-squares sense for a linear system, which biological systems are not. For weakly nonlinear systems, the *extended Kalman filter* (EKF) approximates the system with locally linear functions using low-order Taylor expansions [131]. This linearization can produce unstable filters if the local linearity is violated. Furthermore, for many systems, the determination of the Jacobian matrices are nontrivial and would be difficult to implement. The *unscented Kalman filter* (UKF) preserves the exact nonlinearity of the model system by approximating the probability density of the possible state values [134,136]. This approach is motivated by the fact that is easier to approximate this distribution as a Gaussian than to approximate an arbitrary nonlinear function by linearization.

The state and measurement equations for the UKF are given by:

$$\mathbf{x}_{i+1} = F(\mathbf{x}_i) + \mathbf{w}_i \tag{56}$$

$$\mathbf{y}_{i+1} = G(\mathbf{x}_i) + \mathbf{v}_i \tag{57}$$

$$\mathbf{w} \sim (0, Q_w) \tag{58}$$

$$\mathbf{v} \sim (0, Q_v) \tag{59}$$

where $\mathbf{w}$ and $\mathbf{v}$ are random numbers sampled from a Gaussian distribution with zero mean and standard deviations of Q_w and Q_v. $F(\mathbf{x}_i)$ are the nonlinear system equations and $G(\mathbf{x}_i)$ relates the system states to the actual measurements made from the system.

The UKF uses the "unscented transform" to propagate mean and covariance information through nonlinear transformations [134, 136]. The unscented transform works by constructing a set of points, referred to as sigma points, χ_i, that as a population capture the same known statistics, mean and covariance, as a given measurement or state estimate. A specified nonlinear transformation can be applied to each sigma point, and the unscented estimate can be obtained by computing the statistics of the transformed set. For example, the mean and covariance of the transformed set approximates the nonlinear transformation of the original mean and covariance estimate. sThe sigma points are determined by computing the square root of the error covariance matrix and adding the resulting plus or minus standard deviation to the state estimates:

$$\tilde{\chi}_i = \bar{\mathbf{x}} \pm (\sqrt{n\mathbf{P}})_i \text{ with i=1,...,n} \tag{60}$$

There are $2n$ sigma points, twice as many points as states in the filter. Each sigma point is propagated through the complete nonlinear equations of the neuron model to produce a set of state estimates. This set is then averaged back into a single new state estimate with an updated mean and covariance and constitute the *a priori* estimate before any measurements are made from the system:

$$\tilde{\mathbf{x}} = \frac{1}{2n}\sum_{i=1}^{2n}\tilde{\chi}_i \tag{61}$$

$$\tilde{\mathbf{P}}_{xx} = \frac{1}{2n}\sum_{i=1}^{2n}(\tilde{\chi}_i - \tilde{\mathbf{x}})(\tilde{\chi}_i - \tilde{\mathbf{x}})' + \mathbf{Q}_{\mathbf{w}} \tag{62}$$

The UKF transformation method preserves the second order accuracy in mean and covariance and guarantees the same performance as a truncated second order filter with the same order of calculations as the extended Kalman filter. The UKF can give good results for even higher order nonlinearities if the time steps are small enough that the temporal dynamics of the systems are only weakly nonlinear [253].

Similarly, a set of measurement vectors, $\mathcal{Y}_i$, is determined from the sigma points and they are also averaged to a single measurement, where $\tilde{\mathbf{P}}_{yy}$ represents the error in the model's predicted measurements:

$$\tilde{\mathbf{y}} = \frac{1}{2n}\sum_{i=1}^{2n}\mathcal{Y}_i \tag{63}$$

$$\tilde{\mathbf{P}}_{yy} = \frac{1}{2n}\sum_{i=1}^{2n}(\tilde{\mathcal{Y}}_i - \tilde{\mathbf{y}})(\tilde{\mathcal{Y}}_i - \tilde{\mathbf{y}})' + \mathbf{Q}_{\mathbf{v}} \tag{64}$$

We also compute the cross-covariance between the model's state predictions and the measurement predictions:

$$\tilde{\mathbf{P}}_{xy} = \frac{1}{2n}\sum_{i=1}^{2n}(\tilde{\chi}_i - \tilde{\mathbf{x}})(\tilde{\mathcal{Y}}_i - \tilde{\mathbf{y}})' \tag{65}$$

The ratio between this cross covariance and the error in the model's measurement prediction gives the Kalman gain:

$$K = \tilde{\mathbf{P}}_{xy}\tilde{\mathbf{P}}_{yy}^{-1} \tag{66}$$

The final state estimate is:

$$\hat{\mathbf{x}} = \tilde{\mathbf{x}} + K(\mathbf{y} - \tilde{\mathbf{y}}) \tag{67}$$

The last step is to update the *a posteriori* error covariance matrix:

$$\hat{\mathbf{P}}_{xx} = \tilde{\mathbf{P}}_{xx} - K\tilde{\mathbf{P}}'_{xy} \tag{68}$$

B.3 Neuron models for evaluating the Kalman Filter

B.3.1 Hodgkin-Huxley Model

The Hodgkin-Huxley model was developed to reproduce the action potential based on data from the giant axon of the squid [114–118].

$$C_m \frac{dV_m}{dt} = -\bar{g}_{NaF} m^3 h (V_m - E_{Na}) - \bar{g}_K n^4 (V_m - E_K) - \bar{g}_L (V_m - E_L) \tag{69}$$

$$\frac{dx}{dt} = \alpha_x (1 - x) - \beta_x x \text{ with } x = \{m, h, n\} \tag{70}$$

$$\alpha_m = 0.32 \frac{V_m + 54}{1 - \exp\left[\frac{-(V_m+54)}{4}\right]} \tag{71}$$

$$\beta_m = 0.28 \frac{V_m + 27}{\exp\left[\frac{(V_m+27)}{5}\right] - 1} \tag{72}$$

$$\alpha_h = 0.128 \exp\left[\frac{-(V_m + 50)}{18}\right] \tag{73}$$

$$\beta_h = \frac{4}{1 + \exp\left[\frac{-(V_m+27)}{5}\right]} \tag{74}$$

$$\alpha_n = 0.032 \frac{V_m + 52}{1 - \exp\left[\frac{-(V_m+52)}{5}\right]} \tag{75}$$

$$\beta_n = 0.5 \exp\left[\frac{-(V_m + 57)}{40}\right] \tag{76}$$

with $\bar{g}_{NaF} = 100 \frac{\text{mS}}{\text{cm}^2}, \bar{g}_K = 80 \frac{\text{mS}}{\text{cm}^2}, g_L = 0.1 \frac{\text{mS}}{\text{cm}^2}, E_{Na} = 50\,\text{mV}, E_K = -100\,\text{mV}$, $E_L = -67\,\text{mV}, C_m = 1 \frac{\mu\text{F}}{\text{cm}^2}$.

B.3.2 Connor-Stevens Model

Compared to the Hodgkin-Huxley model, the Connor-Stevens model contains an additional A-type potassium channel. The specific channel properties are different and the Connor-Stevens model has shorter action potentials and a more depolarized average membrane potential [49, 50].

$$C_m \frac{dV_m}{dt} = -\bar{g}_{NaF} m^3 h (V_m - E_{Na}) - \bar{g}_K n^4 (V_m - E_K) - \bar{g}_{KA} a^3 b (V_m - E_{KA}) \tag{77}$$

$$- \bar{g}_L (V_m - E_L) \tag{78}$$

$$x_\infty = \frac{\alpha_x}{\alpha_x + \beta_x} \text{ with } x = \{m, h, n, a, b\} \tag{79}$$

$$\tau_x = \frac{1}{\alpha_x + \beta_x} \tag{80}$$

$$\frac{dx}{dt} = \frac{x_\infty - x}{\tau_x} \tag{81}$$

$$\alpha_m = 0.38 \frac{V_m + 29.7}{1 - \exp\left[\frac{-(V_m + 29.7)}{10}\right]} \tag{82}$$

$$\beta_m = 15.2 \exp\left[-0.0556 * (V_m + 54.7)\right] \tag{83}$$

$$\alpha_h = 0.266 \exp\left[-0.05 * (V_m + 48)\right] \tag{84}$$

$$\beta_h = \frac{3.8}{1 + \exp\left[-0.1 * (V_m + 18)\right]} \tag{85}$$

$$\alpha_n = 0.02 * \frac{V_m + 45.7}{1 - \exp\left[-0.1 * (V_m + 45.7)\right]} \tag{86}$$

$$\beta_n = 0.25 \exp\left[-0.0125 * (V_m + 55.7)\right] \tag{87}$$

$$a_\infty = \left(\frac{0.0761 * \exp\left[0.0314 (V_m + 94.22)\right]}{1 + \exp\left[0.0346 (V_m + 1.17)\right]}\right)^{1/3} \tag{88}$$

$$\tau_a = 0.3632 + 1.158 / (1 + \exp\left[0.0497 (V_m + 55.96)\right]) \tag{89}$$

$$b_\infty = \left(\frac{1}{1 + \exp\left[0.0688 (V_m + 53.3)\right]}\right)^4 \tag{90}$$

$$\tau_b = 1.24 + 2.678 / (1 + \exp\left[0.0624 (V_m + 50)\right]) \tag{91}$$

with $\bar{g}_{NaF} = 120 \frac{\text{mS}}{\text{cm}^2}, \bar{g}_K = 20 \frac{\text{mS}}{\text{cm}^2}, \bar{g}_{KA} = 47.7 \frac{\text{mS}}{\text{cm}^2}, g_L = 0.3 \frac{\text{mS}}{\text{cm}^2}, E_{Na} = 55 \text{ mV}$,
$E_K = -72 \text{ mV}, E_{KA} = -75 \text{ mV}, E_L = -17 \text{ mV}, C_m = 1 \frac{\mu\text{F}}{\text{cm}^2}$.

B.3.3 Wang-Buzsaki Model

The Wang-Buzsaki model was developed for a study of fast oscillations in the neocortex and hippocampus [256]. It features a single fast sodium channel and a potassium channel like the Hodgkin-Huxley model. However, the kinetics of the m activation variable for the sodium channel are approximated using its steady-state value, which eliminates a differential equation from the system.

$$C_m \frac{dV_m}{dt} = -\bar{g}_{NaF} m_\infty^3 h(V_m - E_{Na}) - \bar{g}_K n^4 (V_m - E_K) - \bar{g}_L (V_m - E_L) \tag{92}$$

$$x_\infty = \frac{\alpha_x}{\alpha_x + \beta_x} \text{ with } x = \{m, h, n\} \tag{93}$$

$$\tau_x = \frac{1}{\alpha_x + \beta_x} \tag{94}$$

$$\frac{dx}{dt} = \frac{x_\infty - x}{\tau_x} \text{ with } x = \{m\} \tag{95}$$

$$\frac{dx}{dt} = \frac{5 * (x_\infty - h)}{\tau_x} \text{ with } x = \{h, n\} \tag{96}$$

$$\alpha_m = 0.1 \frac{V_m + 35}{1 - \exp\left[\frac{-(V_m + 35)}{10}\right]} \tag{97}$$

$$\beta_m = 4 \exp\left[\frac{-(V_m + 60)}{18}\right] \tag{98}$$

$$\alpha_h = 0.07 \exp\left[\frac{-(V_m + 58)}{20}\right] \tag{99}$$

$$\beta_h = \frac{1}{1 + \exp\left[\frac{-(V_m + 28)}{10}\right]} \tag{100}$$

$$\alpha_n = 0.01 * \frac{V_m + 34}{1 - \exp\left[\frac{-(V_m + 34)}{10}\right]} \tag{101}$$

$$\beta_n = 0.125 \exp\left[\frac{-(V_m + 44)}{80}\right] \tag{102}$$

with $\bar{g}_{NaF} = 35 \frac{\text{mS}}{\text{cm}^2}, \bar{g}_K = 9 \frac{\text{mS}}{\text{cm}^2}, g_L = 0.1 \frac{\text{mS}}{\text{cm}^2}, E_{Na} = 55 \text{ mV}, E_K = -90 \text{ mV}, E_L = -65 \text{ mV}, C_m = 1 \frac{\mu\text{F}}{\text{cm}^2}$.

REFERENCES

[1] Achard, P. and De Schutter, E., "Complex parameter landscape for a complex neuron model," *PLoS Comput Biol*, vol. 2, p. e94, July 2006.

[2] Agüera y Arcas, B. and Fairhall, A. L., "What causes a neuron to spike?," *Neural Comput*, vol. 15, pp. 1789–1807, Aug. 2003.

[3] Aizenman, C. and Linden, D., "Regulation of the rebound depolarization and spontaneous firing patterns of deep nuclear neurons in slices of rat cerebellum," *J Neurophysiol*, vol. 82, pp. 1697–1709, Oct. 1999.

[4] Akemann, W. and Knopfel, T., "Interaction of Kv3 potassium channels and resurgent sodium current influences the rate of spontaneous firing of Purkinje neurons," *J Neurosci*, vol. 26, pp. 4602–4612, Apr. 2006.

[5] Alviña, K., "The therapeutic mode of action of 4-aminopyridine in cerebellar ataxia," *J. Neurosci.*, 2010.

[6] Alviña, K., Walter, J. T., Kohn, A., Ellis-Davies, G., and Khodakhah, K., "Questioning the role of rebound firing in the cerebellum," *Nat Neurosci*, vol. 11, pp. 1256–1258, Nov. 2008.

[7] Aman, T. and Raman, I. M., "Subunit dependence of Na channel slow inactivation and open channel block in cerebellar neurons," *Biophys J*, vol. 92, pp. 1938–1951, Mar. 2007.

[8] Anchisi, D., Scelfo, B., and Tempia, F., "Postsynaptic currents in deep cerebellar nuclei," *J Neurophysiol*, vol. 85, no. 1, pp. 323–331, 2001.

[9] Anderson, J. S., Carandini, M., and Ferster, D., "Orientation tuning of input conductance, excitation, and inhibition in cat primary visual cortex," *J Neurophysiol*, vol. 84, pp. 909–926, Aug. 2000.

[10] Andrews, R. J., "Chapter 7 - Neuromodulation: Deep brain stimulation, sensory neuroprostheses, and the neural-electrical interface," *Prog Brain Res*, vol. 180, pp. 127–139, 2009.

[11] Armstrong, D. and Rawson, J., "Activity patterns of cerebellar cortical neurones and climbing fibre afferents in the awake cat," *J Physiol*, vol. 289, pp. 425–448, Apr. 1979.

[12] Baranauskas, G., Tkatch, T., Nagata, K., Yeh, J., and Surmeier, D. J., "Kv3.4 subunits enhance the repolarizing efficiency of Kv3.1 channels in fast-spiking neurons," *Nat Neurosci*, vol. 6, pp. 258–266, Mar. 2003.

[13] Baranauskas, G., Tkatch, T., and Surmeier, D. J., "Delayed rectifier currents in rat globus pallidus neurons are attributable to Kv2.1 and Kv3.1/3.2 K+ channels," *J Neurosci*, vol. 19, pp. 6394–6404, Aug. 1999.

[14] Barry, P., "JPCalc, a software package for calculating liquid junction potential corrections in patch-clamp, intracellular, epithelial and bilayer measurements and for correcting junction potential measurements," *J Neurosci Methods*, vol. 51, pp. 107–116, 1994.

[15] Bartos, M., Manor, Y., Nadim, F., Marder, E., and Nusbaum, M., "Coordination of fast and slow rhythmic neuronal circuits," *J Neurosci*, vol. 19, pp. 6650–6660, Aug. 1999.

[16] Beck, H., "Plasticity of intrinsic neuronal properties in CNS disorders," *Nat Rev Neurosci*, 2008.

[17] Bédard, C., Béhuret, S., Deleuze, C., Bal, T., and Destexhe, A., "Oversampling method to extract excitatory and inhibitory conductances from single-trial membrane potential recordings.," *J Neurosci Methods*, Sept. 2011.

[18] Beeman, D. and Bower, J., *The Book of Genesis*. Springer, 1993.

[19] Belmeguenai, A., Hosy, E., Bengtsson, F., Pedroarena, C. M., Piochon, C., Teuling, E., He, Q., Ohtsuki, G., De Jeu, M. T. G., Elgersma, Y., De Zeeuw, C. I., Jörntell, H., and Hansel, C., "Intrinsic plasticity complements long-term potentiation in parallel fiber input gain control in cerebellar Purkinje cells.," *J Neurosci*, vol. 30, pp. 13630–13643, Oct. 2010.

[20] Benda, J., Gollisch, T., Machens, C. K., and Herz, A. V. M., "From response to stimulus: adaptive sampling in sensory physiology," *Current Opinion in Neurobiology*, vol. 17, pp. 430–436, Aug. 2007.

[21] Bennett, B. D., Callaway, J. C., and Wilson, C. J., "Intrinsic membrane properties underlying spontaneous tonic firing in neostriatal cholinergic interneurons.," *J Neurosci*, vol. 20, pp. 8493–8503, Nov. 2000.

[22] Berecki, G., Zegers, J. G., Verkerk, A. O., Bhuiyan, Z. A., de Jonge, B., Veldkamp, M. W., Wilders, R., and van Ginneken, A. C. G., "HERG channel (dys)function revealed by dynamic action potential clamp technique," *Biophys J*, vol. 88, no. 1, pp. 566–578, 2005.

[23] Bernander, O., Douglas, R. J., Martin, K. A., and Koch, C., "Synaptic background activity influences spatiotemporal integration in single pyramidal cells," *Proc Natl Acad Sci U S A*, vol. 88, pp. 11569–11573, Dec. 1991.

[24] Bettencourt, J. C., Lillis, K. P., Stupin, L. R., and White, J. A., "Effects of imperfect dynamic clamp: Computational and experimental results," *J Neurosci Methods*, vol. 169, no. 2, pp. 282–289, 2008.

[25] Bhalla, U. S. and Bower, J., "Exploring parameter space in detailed single neuron models: simulations of the mitral and granule cells of the olfactory bulb," *J Neurophysiol*, vol. 69, pp. 1948–1965, June 1993.

[26] Bialek, W. and Rieke, F., "Reliability and information transmission in spiking neurons," *Trends Neurosci*, vol. 15, pp. 428–434, Nov. 1992.

[27] Bond, C. T., Herson, P. S., Strassmaier, T., Hammond, R., Stackman, R., Maylie, J., and Adelman, J. P., "Small conductance Ca2+-activated K+ channel knock-out mice reveal the identity of calcium-dependent afterhyperpolarization currents.," *J Neurosci*, vol. 24, pp. 5301–5306, June 2004.

[28] Bond, C. and Maylie, J., "SK channels in excitability, pacemaking and synaptic integration," *Current Opinion in Neurobiology*, 2005.

[29] Borg-Graham, L. J., Monier, C., and Fregnac, Y., "Visual input evokes transient and strong shunting inhibition in visual cortical neurons," *Nature*, vol. 393, pp. 369–373, May 1998.

[30] Brickley, S. G., Revilla, V., Cull-Candy, S. G., Wisden, W., and Farrant, M., "Adaptive regulation of neuronal excitability by a voltage-independent potassium conductance.," *Nature*, vol. 409, pp. 88–92, Jan. 2001.

[31] Brizzi, L., Meunier, C., Zytnicki, D., Donnet, M., Hansel, D., D'Incamps, B., and Van Vreeswijk, C., "How shunting inhibition affects the discharge of lumbar motoneurones: a dynamic clamp study in anaesthetized cats," *J Physiol*, vol. 558, pp. 671–683, July 2004.

[32] Bronstein, J. M., Tagliati, M., Alterman, R. L., Lozano, A. M., Volkmann, J., Stefani, A., Horak, F. B., Okun, M. S., Foote, K. D., Krack, P., Pahwa, R., Henderson, J. M., Hariz, M. I., Bakay, R. A., Rezai, A., Marks, W. J., Moro, E., Vitek, J. L., Weaver, F. M., Gross, R. E., and Delong, M. R., "Deep brain stimulation for Parkinson disease: an expert consensus and review of key issues," *Arch Neurol*, vol. 68, p. 165, Feb. 2011.

[33] Brown, R. G., *Introduction to Random Signal Analysis and Kalman Filtering*. New York: John Wiley & Sons, 1983.

[34] Brumberg, J. S. and Guenther, F. H., "Development of speech prostheses: current status and recent advances," *Expert Rev Med Devices*, vol. 7, pp. 667–679, Sept. 2010.

[35] Butera, R. J. and McCarthy, M., "Analysis of real-time numerical integration methods applied to dynamic clamp experiments," *J Neural Eng*, vol. 1, pp. 187–194, Dec. 2004.

[36] Butera, R. J., Wilson, C. J., Del Negro, C. A., and Smith, J. C., "A methodology for achieving high-speed rates for artificial conductance injection in electrically excitable biological cells," *IEEE Trans Biomed Eng*, vol. 48, pp. 1460–1470, Dec. 2001.

[37] Calderon, D. P., Fremont, R., Kraenzlin, F., and Khodakhah, K., "The neural substrates of rapid-onset Dystonia-Parkinsonism.," *Nat Neurosci*, vol. 14, pp. 357–365, Mar. 2011.

[38] Campanac, E., Daoudal, G., Ankri, N., and Debanne, D., "Downregulation of dendritic I(h) in CA1 pyramidal neurons after LTP," *J Neurosci*, vol. 28, pp. 8635–8643, Aug. 2008.

[39] Canavier, C. C. and Landry, R. S., "An increase in AMPA and a decrease in SK conductance increase burst firing by different mechanisms in a model of a dopamine neuron in vivo.," *J Neurophysiol*, vol. 96, pp. 2549–2563, Nov. 2006.

[40] Cannon, R. C., O'Donnell, C., and Nolan, M. F., "Stochastic ion channel gating in dendritic neurons: morphology dependence and probabilistic synaptic activation of dendritic spikes.," *PLoS Comput Biol*, vol. 6, no. 8, 2010.

[41] Chan-Palay, V., *Cerebellar dentate nucleus: Organization, cytology and transmitters*. Springer-Verlag, 1977.

[42] Chance, F., Abbott, L. F., and Reyes, A., "Gain modulation from background synaptic input," *Neuron*, vol. 35, no. 4, pp. 773–782, 2002.

[43] Christini, D. J., Stein, K. M., Markowitz, S. M., Mittal, S., Slotwiner, D. J., Scheiner, M. A., Iwai, S., and Lerman, B. B., "Nonlinear-dynamical arrhythmia control in humans," *Proc Natl Acad Sci U S A*, vol. 98, pp. 5827–5832, May 2001.

[44] Clewley, R., Sherwood, W., Lamar, M., and Guckenheimer, J., "PyDSTool, a software environment for dynamical systems modeling," May 2007, Available: http://pydstool.sourceforge.net.

[45] Clewley, R., "Inferring and quantifying the role of an intrinsic current in a mechanism for a half-center bursting oscillation: A dominant scale and hybrid dynamical systems analysis," *Journal of Biological Physics*, 2011.

[46] Clewley, R., Rotstein, H. G., and Kopell, N., "A Computational Tool for the Reduction of Nonlinear ODE Systems Possessing Multiple Scales," *Multiscale modeling & simulation*, vol. 4, pp. 732–759, Feb. 2005.

[47] Clewley, R., Soto-Treviño, C., and Nadim, F., "Dominant ionic mechanisms explored in spiking and bursting using local low-dimensional reductions of a biophysically realistic model neuron," *J Comput Neurosci*, vol. 26, pp. 75–90, Feb. 2009.

[48] Conductance, C., "Real-time models in electrophysiology." Available: http://www.cambridgeconductance.com/.

[49] Connor, J. A. and Stevens, C. F., "Prediction of repetitive firing behaviour from voltage clamp data on an isolated neurone soma.," *J Physiol (Lond)*, vol. 213, pp. 31–53, Feb. 1971.

[50] Connor, J., "Neural repetitive firing: a comparative study of membrane properties of crustacean walking leg axons," *J Neurophysiol*, 1975.

[51] Crunelli, V., Toth, T., Cope, D., Blethyn, K., and Hughes, S., "The "window' T-type calcium current in brain dynamics of different behavioural states," *J Physiol (Lond)*, vol. 562, no. 1, pp. 121–129, 2005.

[52] Crunelli, V., Cope, D. W., and Hughes, S. W., "Thalamic T-type Ca2+ channels and NREM sleep," *Cell Calcium*, vol. 40, pp. 175–190, Aug. 2006.

[53] Culianu, C. A. and Christini, D. J., "Real-time experiment interface system: RTLab," in *3rd Real-Time Linux Workshop*, (Milan, Italy), Nov. 2001.

[54] Culianu, C. A. and Christini, D. J., "A sample data acquisition and control application using RTLab," in *4th Real-Time Linux Workshop*, (Boston, MA), Dec. 2002.

[55] de Boer, R. and Kuyper, P., "Triggered correlation," *IEEE Trans Biomed Eng*, vol. 15, pp. 169–179, July 1968.

[56] De Schutter, E. and Steuber, V., "Patterns and pauses in Purkinje cell simple spike trains: experiments, modeling and theory," *Neuroscience*, vol. 162, pp. 816–826, Sept. 2009.

[57] de Waele, C., Serafin, M., Khateb, A., Yabe, T., Vidal, P. P., and Muhlethaler, M., "Medial vestibular nucleus in the guinea-pig: apamin-induced rhythmic burst firing–an in vitro and in vivo study.," *Exp Brain Res*, vol. 95, no. 2, pp. 213–222, 1993.

[58] De Zeeuw, C. I. and Berrebi, A. S., "Postsynaptic targets of Purkinje cell terminals in the cerebellar and vestibular nuclei of the rat," *Eur J Neurosci*, vol. 7, pp. 2322–2333, Nov. 1995.

[59] Debay, D., Wolfart, J., Le Franc, Y., Le Masson, G., and Bal, T., "Exploring spike transfer through the thalamus using hybrid artificial-biological neuronal networks," *J Physiol Paris*, vol. 98, pp. 540–558, July 2004.

[60] Deister, C. A., Teagarden, M. A., Wilson, C. J., and Paladini, C. A., "An intrinsic neuronal oscillator underlies dopaminergic neuron bursting," *J Neurosci*, vol. 29, pp. 15888–15897, Dec. 2009.

[61] Desai, N. S. and Walcott, E., "Synaptic bombardment modulates muscarinic effects in forelimb motor cortex," *J Neurosci*, vol. 26, pp. 2215–2226, Feb. 2006.

[62] Design, C. E., "Signal Version 5: Sweep-based data acquisition and analysis system." Available: http://www.ced.co.uk/.

[63] Destexhe, A., Neubig, M., Ulrich, D., and Huguenard, J., "Dendritic Low-Threshold Calcium Currents in Thalamic Relay Cells," *J Neurosci*, vol. 18, pp. 3574–3588, May 1998.

[64] Destexhe, A. and Rudolph, M., "Extracting information from the power spectrum of synaptic noise.," *J Comput Neurosci*, vol. 17, pp. 327–345, Oct. 2004.

[65] Destexhe, A., Rudolph-Lilith, M., Fellous, J., and Sejnowski, T. J., "Fluctuating synaptic conductances recreate in vivo-like activity in neocortical neurons," *Neuroscience*, vol. 107, no. 1, pp. 13–24, 2001.

[66] Destexhe, A., Rudolph-Lilith, M., and Pare, D., "The high-conductance state of neocortical neurons in vivo," *Nat Rev Neurosci*, vol. 4, no. 9, pp. 739–751, 2003.

[67] Dorval, A. D., Christini, D. J., and White, J. A., "Real-Time Linux dynamic clamp: a fast and flexible way to construct virtual ion channels in living cells," *Annals of Biomedical Engineering*, vol. 29, pp. 897–907, Oct. 2001.

[68] Druckmann, S., Banitt, Y., Gidon, A. A., Schürmann, F., Markram, H., and Segev, I., "A novel multiple objective optimization framework for constraining conductance-based neuron models by experimental data," *Front Neurosci*, vol. 1, pp. 7–18, Aug. 2007.

[69] Druckmann, S., Berger, T. K., Hill, S., Schürmann, F., Markram, H., and Segev, I., "Evaluating automated parameter constraining procedures of neuron models by experimental and surrogate data," *Biol Cybern*, vol. 99, pp. 371–379, Nov. 2008.

[70] Economo, M. and Fernandez, F., "Dynamic clamp: alteration of response properties and creation of virtual realities in neurophysiology," *J Neurosci*, vol. 30, no. 7, pp. 2407–2413, 2010.

[71] Edin, F., Machens, C. K., Schütze, H., and Herz, A. V. M., "Searching for optimal sensory signals: iterative stimulus reconstruction in closed-loop experiments," *J Comput Neurosci*, vol. 17, no. 1, pp. 47–56, 2004.

[72] Eilers, J., "Dendritic signal integration," *Current Opinion in Neurobiology*, 1997.

[73] Fellous, J., Rudolph-Lilith, M., Destexhe, A., and Sejnowski, T. J., "Synaptic background noise controls the input/output characteristics of single cells in an in vitro model of in vivo activity," *Neuroscience*, vol. 122, no. 3, pp. 811–829, 2003.

[74] Feng, S. and Jaeger, D., "The Role of SK Calcium-Dependent Potassium Currents in Regulating the Activity of Deep Cerebellar Nucleus Neurons: A Dynamic Clamp Study," *Cerebellum*, vol. 7, no. 4, pp. 542–546, 2008.

[75] Fernandez, F. R. and White, J. A., "Gain control in CA1 pyramidal cells using changes in somatic conductance," *J Neurosci*, vol. 30, pp. 230–241, Jan. 2010.

[76] Fernandez, F., "Artificial synaptic conductances reduce subthreshold oscillations and periodic firing in stellate cells of the entorhinal cortex," *J. Neurosci.*, 2008.

[77] Fox, R., "Stochastic versions of the Hodgkin-Huxley equations," *Biophys J*, 1997.

[78] Fox, R. and Lu, Y., "Emergent collective behavior in large numbers of globally coupled independently stochastic ion channels.," *Phys Rev E Stat Phys Plasmas Fluids Relat Interdiscip Topics*, vol. 49, pp. 3421–3431, Apr. 1994.

[79] Fregnac, Y., Monier, C., Chavane, F., Baudot, P., and Graham, L. J., "Shunting inhibition, a silent step in visual cortical computation," *J Physiol Paris*, vol. 97, no. 4-6, pp. 441–451, 2003.

[80] Garfinkel, A., Spano, M. L., Ditto, W. L., and Weiss, J. N., "Controlling cardiac chaos," *Science*, vol. 257, pp. 1230–1235, Aug. 1992.

[81] Gasparini, S., Migliore, M., and Magee, J., "On the Initiation and Propagation of Dendritic Spikes in CA1 Pyramidal Neurons," *J Neurosci*, vol. 24, pp. 11046–11056, Dec. 2004.

[82] Gauck, V. and Jaeger, D., "The control of rate and timing of spikes in the deep cerebellar nuclei by inhibition," *J Neurosci*, vol. 20, no. 8, pp. 3006–3016, 2000.

[83] Gauck, V. and Jaeger, D., "The contribution of NMDA and AMPA conductances to the control of spiking in neurons of the deep cerebellar nuclei," *J Neurosci*, vol. 23, no. 22, pp. 8109–8118, 2003.

[84] Gauck, V., Thomann, M., Jaeger, D., and Borst, A., "Spatial distribution of low- and high-voltage-activated calcium currents in neurons of the deep cerebellar nuclei," *J Neurosci*, vol. 21, p. RC158, Aug. 2001.

[85] Gerken, W., Purvis, L., and Butera, R. J., "Genetic algorithm for optimization and specification of a neuron model," *Conf Proc IEEE Eng Med Biol Soc*, vol. 4, pp. 4321–4323, 2005.

[86] Ghigliazza, R. and Holmes, P., "Minimal Models of Bursting Neurons: How Multiple Currents, Conductances, and Timescales Affect Bifurcation Diagrams," *SIAM Journal on Applied Dynamical Systems*, vol. 3, pp. 636–670, 2004.

[87] Giessel, A. J. and Sabatini, B. L., "M1 muscarinic receptors boost synaptic potentials and calcium influx in dendritic spines by inhibiting postsynaptic SK channels.," *Neuron*, vol. 68, pp. 936–947, Dec. 2010.

[88] Gittelman, J. X., Li, N., and Pollak, G. D., "Mechanisms underlying directional selectivity for frequency-modulated sweeps in the inferior colliculus revealed by in vivo whole-cell recordings," *J Neurosci*, vol. 29, pp. 13030–13041, Oct. 2009.

[89] Gittelman, J. X. and Pollak, G. D., "It's about time: how input timing is used and not used to create emergent properties in the auditory system," *J Neurosci*, vol. 31, pp. 2576–2583, Feb. 2011.

[90] Goaillard, J.-M. and Marder, E., "Dynamic clamp analyses of cardiac, endocrine, and neural function," *Physiology (Bethesda)*, vol. 21, pp. 197–207, June 2006.

[91] Goldwyn, J. H., Imennov, N. S., Famulare, M., and Shea-Brown, E., "On stochastic differential equation models for ion channel noise in Hodgkin-Huxley neurons," *arXiv*, vol. q-bio.NC, Sept. 2010.

[92] Goldwyn, J. H. and Shea-Brown, E., "The what and where of adding channel noise to the Hodgkin-Huxley equations," *arXiv*, vol. q-bio.NC, Apr. 2011.

[93] Golowasch, J., Goldman, M. S., Abbott, L. F., and Marder, E., "Failure of averaging in the construction of a conductance-based neuron model," *J Neurophysiol*, vol. 87, pp. 1129–1131, Feb. 2002.

[94] Greenhill, S. D. and Jones, R. S. G., "Simultaneous estimation of global background synaptic inhibition and excitation from membrane potential fluctuations in layer III neurons of the rat entorhinal cortex in vitro," *Neuroscience*, vol. 147, pp. 884–892, July 2007.

[95] Guillamon, A., McLaughlin, D., and Rinzel, J., "Estimation of synaptic conductances," *J Physiol Paris*, vol. 100, no. 1-3, pp. 31–42, 2006.

[96] Gunay, C., Edgerton, J., and Jaeger, D., "Channel density distributions explain spiking variability in the globus pallidus: a combined physiology and computer simulation database approach," *J Neurosci*, vol. 28, pp. 7476–7491, Apr. 2008.

[97] Haas, J. S., Kreuz, T., Torcini, A., Politi, A., and Abarbanel, H. D. I., "Rate maintenance and resonance in the entorhinal cortex," *Eur J Neurosci*, Oct. 2010.

[98] Hahn, J., Kullmann, P., Horn, J., and Levitan, E., "D2 autoreceptors chronically enhance dopamine neuron pacemaker activity," *J Neurosci*, vol. 26, pp. 5240–5247, May 2006.

[99] Haider, B., Duque, A., Hasenstaub, A. R., and McCormick, D. A., "Neocortical network activity in vivo is generated through a dynamic balance of excitation and inhibition," *J Neurosci*, vol. 26, pp. 4535–4545, Apr. 2006.

[100] Hall, K., Christini, D. J., Tremblay, M., and Collins, J., "Dynamic control of cardiac alternans," *Physical Review Letters*, vol. 78, no. 23, pp. 4518–4521, 1997.

[101] Hanson, J., Smith, Y., and Jaeger, D., "Sodium Channels and Dendritic Spike Initiation at Excitatory Synapses in Globus Pallidus Neurons," *J Neurosci*, vol. 24, no. 2, pp. 329–340, 2004.

[102] Harris-Warrick, R., Coniglio, L., Levini, R., Gueron, S., and Guckenheimer, J., "Dopamine modulation of two subthreshold currents produces phase shifts in activity of an identified motoneuron," *J Neurophysiol*, vol. 74, pp. 1404–1420, Oct. 1995.

[103] Harsch, A. and Robinson, H., "Postsynaptic variability of firing in rat cortical neurons: The roles of input synchronization and synaptic NMDA receptor conductance," *J Neurosci*, vol. 20, no. 16, pp. 6181–6192, 2000.

[104] Hausser, M., "Revealing the properties of dendritic voltage-gated channels: a new approach to the space clamp problem," *Biophys J*, vol. 84, pp. 3497–3498, June 2003.

[105] Hayes, M. H., *Statistical Digital Signal Processing and Modeling*. New York: Wiley, 1996.

[106] Heck, D., Kummell, F., Thach, W., and Aertsen, A., "Dynamic correlation of neuronal activity in rat cerebellar cortex modulated by behavior," *Ann N Y Acad Sci*, vol. 978, pp. 156–163, Dec. 2002.

[107] Heck, D., Thach, W., and Keating, J., "On-beam synchrony in the cerebellum as the mechanism for the timing and coordination of movement," *Proc Natl Acad Sci U S A*, vol. 104, pp. 7658–7663, May 2007.

[108] HEKA, *ITC-18: 16-bit data acquisition interface*.

[109] Hendrickson, E. B., Edgerton, J. R., and Jaeger, D., "The use of automated parameter searches to improve ion channel kinetics for neural modeling," *J Comput Neurosci*, Jan. 2011.

[110] Hess, F. M. and Abbott, I., "COMEDI: Linux Control and Measurement Device Interface." Available: http://www.comedi.org/.

[111] Hille, B., *Ion Channels of Excitable Membranes*. Sinauer Associates, 3 ed., 2001.

[112] Hines, M. L. and Carnevale, N. T., "The NEURON simulation environment," *Neural Comput*, vol. 9, pp. 1179–1209, Aug. 1997.

[113] Hirsch, J. A., Alonso, J. M., Reid, R. C., and Martinez, L. M., "Synaptic integration in striate cortical simple cells," *J Neurosci*, vol. 18, pp. 9517–9528, Nov. 1998.

[114] HODGKIN, A. L. and HUXLEY, A. F., "The components of membrane conductance in the giant axon of Loligo.," *J Physiol (Lond)*, vol. 116, pp. 473–496, Apr. 1952.

[115] Hodgkin, A., "A quantitative description of membrane current and its application to conduction and excitation in nerve," *The Journal of Physiology*, 1952.

[116] Hodgkin, A., "Currents carried by sodium and potassium ions through the membrane of the giant axon of Loligo," *The Journal of Physiology*, 1952.

[117] Hodgkin, A., "The dual effect of membrane potential on sodium conductance in the giant axon of Loligo," *The Journal of Physiology*, 1952.

[118] Hodgkin, A. and Huxley, A., "Measurement of current-voltage relations in the membrane of the giant axon of Loligo," *The Journal of Physiology*, 1952.

[119] Howland, R. H., Shutt, L. S., Berman, S. R., Spotts, C. R., and Denko, T., "The emerging use of technology for the treatment of depression and other neuropsychiatric disorders," *Ann Clin Psychiatry*, vol. 23, pp. 48–62, Feb. 2011.

[120] Hudson, A. E. and Prinz, A. A., "Conductance ratios and cellular identity.," *PLoS Comput Biol*, vol. 6, no. 7, pp. e1000838–e1000838, 2010.

[121] Hughes, S. W., Lorincz, M., Cope, D. W., and Crunelli, V., "NeuReal: an interactive simulation system for implementing artificial dendrites and large hybrid networks.," *J Neurosci Methods*, vol. 169, pp. 290–301, Apr. 2008.

[122] Hunt, B. R., Kostelich, E. J., and Szunyogh, I., "Efficient data assimilation for spatiotemporal chaos: A local ensemble transform Kalman filter," *Physica D: Nonlinear Phenomena*, vol. 230, no. 1-2, pp. 112–126, 2007.

[123] Hutcheon, B., Miura, R., and Puil, E., "Models of subthreshold membrane resonance in neocortical neurons," *J Neurophysiol*, vol. 76, no. 2, pp. 698–714, 1996.

[124] Huys, Q. J. M., Ahrens, M. B., and Paninski, L., "Efficient estimation of detailed single-neuron models," *J Neurophysiol*, vol. 96, pp. 872–890, Aug. 2006.

[125] Huys, Q. J. M. and Paninski, L., "Smoothing of, and Parameter Estimation from, Noisy Biophysical Recordings," *PLoS Comput Biol*, vol. 5, no. 5, pp. 1–16, 2009.

[126] Jaeger, D. and Bower, J., "Synaptic control of spiking in cerebellar Purkinje cells: Dynamic current clamp based on model conductances," *J Neurosci*, vol. 19, no. 14, pp. 6090–6101, 1999.

[127] Jaeger, D., De Schutter, E., and Bower, J., "The role of synaptic and voltage-gated currents in the control of Purkinje cell spiking: A modeling study," *J Neurosci*, vol. 17, no. 1, pp. 91–106, 1997.

[128] Jahnsen, H., "Electrophysiological characteristics of neurones in the guinea-pig deep cerebellar nuclei in vitro," *J Physiol*, vol. 372, pp. 129–147, Mar. 1986.

[129] Jahnsen, H., "Extracellular activation and membrane conductances of neurones in the guinea-pig deep cerebellar nuclei in vitro," *J Physiol*, vol. 372, pp. 149–168, Mar. 1986.

[130] Jaqaman, K. and Danuser, G., "Linking data to models: data regression.," *Nat Rev Mol Cell Biol*, vol. 7, pp. 813–819, Nov. 2006.

[131] Jazwinski, A. H., *Stochastic Processes and Filtering Theory*. New York: Academic Press, 1970.

[132] Jinnah, H. A., Hess, E. J., LeDoux, M. S., Sharma, N., Baxter, M. G., and Delong, M. R., "Rodent models for dystonia research: Characteristics, evaluation, and utility," *Mov Disord.*, vol. 20, no. 3, pp. 283–292, 2005.

[133] Johnston, D., Magee, J., and Colbert, C., "Active properties of neuronal dendrites," *Annu Rev Neurosci*, 1996.

[134] Julier, S., "A new extension of the Kalman filter to nonlinear systems," *Int. Symp. Aerospace/Defense Sensing*, 1997.

[135] Julier, S., "Reduced sigma point filters for the propagation of means and covariances through nonlinear transformations," *American Control Conference*, vol. 2, pp. 887–892 vol.2, 2002.

[136] Julier, S., "Unscented filtering and nonlinear estimation," *Proceedings of the IEEE*, vol. 92, no. 3, pp. 401–422, 2004.

[137] Kemenes, I., Marra, V., Crossley, M., Samu, D., Staras, K., Kemenes, G., and Nowotny, T., "Dynamic clamp with StdpC software," *Nat Protoc*, vol. 6, pp. 405–417, Mar. 2011.

[138] Kerr, A. M. and Capogna, M., "Unitary IPSPs enhance hilar mossy cell gain in the rat hippocampus.," *J Physiol (Lond)*, vol. 578, pp. 451–470, Jan. 2007.

[139] Kinard, T., de Vries, G., Sherman, A., and Satin, L., "Modulation of the bursting properties of single mouse pancreatic beta-cells by artificial conductances," *Biophys J*, vol. 76, pp. 1423–1435, Mar. 1999.

[140] Kispersky, T., White, J. A., and Rotstein, H. G., "The Mechanism of Abrupt Transition between Theta and Hyper-Excitable Spiking Activity in Medial Entorhinal Cortex Layer II Stellate Cells," *PLoS One*, vol. 5, no. 11, p. e13697, 2010.

[141] Krack, P., Hariz, M. I., Baunez, C., Guridi, J., and Obeso, J. A., "Deep brain stimulation: from neurology to psychiatry?," *Trends Neurosci*, vol. 33, pp. 474–484, Oct. 2010.

[142] Kremling, A. and Saez-Rodriguez, J., "Systems biology–an engineering perspective.," *J. Biotechnol.*, vol. 129, pp. 329–351, Apr. 2007.

[143] Kullmann, P., Wheeler, D., Beacom, J., and Horn, J., "Implementation of a fast 16-Bit dynamic clamp using LabVIEW-RT," *J Neurophysiol*, vol. 91, no. 1, pp. 542–554, 2004.

[144] Kumar, A., Schrader, S., Aertsen, A., and Rotter, S., "The high-conductance state of cortical networks," *Neural Comput*, vol. 20, no. 1, pp. 1–43, 2008.

[145] Lang, E., Sugihara, I., Welsh, J., and Llinas, R., "Patterns of Spontaneous Purkinje Cell Complex Spike Activity in the Awake Rat," *J Neurosci*, vol. 19, pp. 2728–2739, Apr. 1999.

[146] Le Masson, G., Le Masson, S., and Moulins, M., "From conductances to neural network properties: analysis of simple circuits using the hybrid network method," *Prog Biophys Mol Biol*, vol. 64, no. 2-3, pp. 201–220, 1995.

[147] Le Masson, G., Renaud-Le Masson, S., Debay, D., and Bal, T., "Feedback inhibition controls spike transfer in hybrid thalamic circuits," *Nature*, vol. 417, no. 6891, pp. 854–858, 2002.

[148] LeDoux, M., Hurst, D., and Lorden, J., "Single-unit activity of cerebellar nuclear cells in the awake genetically dystonic rat," *Neuroscience*, vol. 86, pp. 533–545, Sept. 1998.

[149] LeDoux, M. S., "Animal models of dystonia: Lessons from a mutant rat.," *Neurobiol. Dis.*, vol. 42, pp. 152–161, May 2011.

[150] LeDoux, M. S. and Lorden, J. F., "Abnormal spontaneous and harmaline-stimulated Purkinje cell activity in the awake genetically dystonic rat.," *Exp Brain Res*, vol. 145, pp. 457–467, Aug. 2002.

[151] Leduc, P., Messner, W., and Wikswo, J., "How Do Control-Based Approaches Enter into Biology?," *Annual Review of Biomedical Engineering*, vol. 13, pp. 369–396, 2011.

[152] Leuthardt, E. C., Schalk, G., Roland, J., Rouse, A., and Moran, D. W., "Evolution of brain-computer interfaces: going beyond classic motor physiology," *Neurosurg Focus*, vol. 27, p. E4, July 2009.

[153] Lev-Tov, A., Miller, J. P., Burke, R. E., and Rall, W., "Factors that control amplitude of EPSPs in dendritic neurons.," *J Neurophysiol*, vol. 50, pp. 399–412, Aug. 1983.

[154] Lewi, J., Butera, R. J., and Paninski, L., "Sequential optimal design of neurophysiology experiments," *Neural Comput*, vol. 21, no. 3, pp. 619–687, 2009.

[155] Lewi, J., Schneider, D., and Woolley, S., "Automating the design of informative sequences of sensory stimuli," *J Comput Neurosci*, pp. 1–20, 2010.

[156] Lewis, J., Lindner, B., Laliberte, B., and Groothuis, S., "Control of neuronal firing by dynamic parallel fiber feedback: implications for electrosensory reafference suppression," *J Exp Biol*, vol. 210, pp. 4437–4447, Dec. 2007.

[157] Lien, C. and Jonas, P., "Kv3 potassium conductance is necessary and kinetically optimized for high-frequency action potential generation in hippocampal interneurons," *J Neurosci*, vol. 23, pp. 2058–2068, Mar. 2003.

[158] Lillacci, G. and Khammash, M., "Parameter estimation and model selection in computational biology.," *PLoS Comput Biol*, vol. 6, p. e1000696, Mar. 2010.

[159] Lin, R. J., Bettencourt, J., White, J. A., Christini, D. J., and Butera, R. J., "Real-time Experiment Interface for biological control applications," *Conf Proc IEEE Eng Med Biol Soc*, vol. 1, pp. 4160–4163, 2010.

[160] Llinas, R. and Muhlethaler, M., "Electrophysiology of guinea-pig cerebellar nuclear cells in the in vitro brain stem-cerebellar preparation," *J Physiol*, vol. 404, pp. 241–258, Oct. 1988.

[161] Lobb, C. J., Wilson, C. J., and Paladini, C. A., "A dynamic role for GABA receptors on the firing pattern of midbrain dopaminergic neurons," *J Neurophysiol*, vol. 104, pp. 403–413, July 2010.

[162] Lobb, C. J., Wilson, C. J., and Paladini, C. A., "High Frequency, Short Latency Disinhibition Bursting of Midbrain Dopaminergic Neurons," *J Neurophysiol*, Mar. 2011.

[163] Loewenstein, Y., Mahon, S., Chadderton, P., Kitamura, K., Sompolinsky, H., Yarom, Y., and Hausser, M., "Bistability of cerebellar Purkinje cells modulated by sensory stimulation," *Nat Neurosci*, vol. 8, pp. 202–211, Feb. 2005.

[164] London, M. and Hausser, M., "Dendritic computation.," *Annu Rev Neurosci*, vol. 28, pp. 503–532, 2005.

[165] Maylie, J. and Adelman, J. P., "Cholinergic signaling through synaptic SK channels: it's a protein kinase but which one?," *Neuron*, vol. 68, pp. 809–811, Dec. 2010.

[166] Medina, J. and Lisberger, S., "Links from complex spikes to local plasticity and motor learning in the cerebellum of awake-behaving monkeys," *Nat Neurosci*, vol. 11, pp. 1185–1192, Oct. 2008.

[167] Milescu, L. S., Yamanishi, T., Ptak, K., Mogri, M. Z., and Smith, J. C., "Real-time kinetic modeling of voltage-gated ion channels using dynamic clamp," *Biophys J*, vol. 95, pp. 66–87, July 2008.

[168] Millán, J. D. R., Rupp, R., Müller-Putz, G. R., Murray-Smith, R., Giugliemma, C., Tangermann, M., Vidaurre, C., Cincotti, F., Kübler, A., Leeb, R., Neuper, C., Müller, K.-R., and Mattia, D., "Combining Brain-Computer Interfaces and Assistive Technologies: State-of-the-Art and Challenges," *Front Neurosci*, vol. 4, 2010.

[169] Molineux, M. L., McRory, J., McKay, B., Hamid, J., Mehaffey, W., Rehak, R., Snutch, T., Zamponi, G., and Turner, R., "Specific T-type calcium channel isoforms are associated with distinct burst phenotypes in deep cerebellar nuclear neurons," *Proc Natl Acad Sci U S A*, vol. 103, pp. 5555–5560, Apr. 2006.

[170] Molineux, M. L., Mehaffey, W., Tadayonnejad, R., Anderson, D., Tennent, A., and Turner, R., "Ionic factors governing rebound burst phenotype in rat deep cerebellar neurons," *J Neurophysiol*, vol. 100, pp. 2684–2701, Nov. 2008.

[171] Monier, C., Fournier, J., and Fregnac, Y., "In vitro and in vivo measures of evoked excitatory and inhibitory conductance dynamics in sensory cortices," *J Neurosci Methods*, vol. 169, pp. 323–365, Apr. 2008.

[172] Monier, C., Chavane, F., Baudot, P., Graham, L. J., and Fregnac, Y., "Orientation and direction selectivity of synaptic inputs in visual cortical neurons: a diversity of combinations produces spike tuning," *Neuron*, vol. 37, pp. 663–680, Feb. 2003.

[173] Morita, K., Kalra, R., Aihara, K., and Robinson, H., "Recurrent synaptic input and the timing of gamma-frequency-modulated firing of pyramidal cells during neocortical "UP" states," *J Neurosci*, vol. 28, pp. 1871–1881, Feb. 2008.

[174] Muri, R. and Knopfel, T., "Activity induced elevations of intracellular calcium concentration in neurons of the deep cerebellar nuclei," *J Neurophysiol*, vol. 71, no. 1, pp. 420–428, 1994.

[175] National Instruments, *NI LabWindows/CVI*.

[176] Nedergaard, S. and Flatman, J., "Nifedipine-and omega-conotoxin-sensitive Ca2+ conductances in guinea-pig substantia nigra pars compacta neurones.," *The Journal of Physiology*, 1993.

[177] Nowak, L. G., Azouz, R., Sanchez-Vives, M. V., Gray, C. M., and McCormick, D. A., "Electrophysiological classes of cat primary visual cortical neurons in vivo as revealed by quantitative analyses.," *J Neurophysiol*, vol. 89, pp. 1541–1566, Mar. 2003.

[178] Nowotny, T., Szucs, A., Pinto, R. D., and Selverston, A. I., "StdpC: A modern dynamic clamp," *J Neurosci Methods*, vol. 158, no. 2, pp. 287–299, 2006.

[179] Otte, S., Hasenstaub, A. R., and Callaway, E., "Cell type-specific control of neuronal responsiveness by gamma-band oscillatory inhibition," *J Neurosci*, vol. 30, pp. 2150–2159, Feb. 2010.

[180] Pal, S., Rosengren, S. M., and Colebatch, J. G., "Stochastic galvanic vestibular stimulation produces a small reduction in sway in Parkinson's disease," *J Vestib Res*, vol. 19, no. 3-4, pp. 137–142, 2009.

[181] Palkovits, M., Mezey, E., Hamori, J., and Szentagothai, J., "Quantitative histological analysis of the cerebellar nuclei in the cat. I. Numerical data on cells and synapses," *Exp Brain Res*, vol. 28, pp. 189–209, 1977.

[182] Paninski, L., Vidne, M., and DePasquale, B., "Inferring synaptic inputs given a noisy voltage trace via sequential Monte Carlo methods," *J Comput Neurosci*, 2011.

[183] Paninski, L., Ahmadian, Y., Ferreira, D. G., Koyama, S., Rahnama Rad, K., Vidne, M., Vogelstein, J., and Wu, W., "A new look at state-space models for neural data," *J Comput Neurosci*, vol. 29, pp. 107–126, Aug. 2010.

[184] Paré, D., Shink, E., Gaudreau, H., Destexhe, A., and Lang, E. J., "Impact of spontaneous synaptic activity on the resting properties of cat neocortical pyramidal neurons in vivo," *J Neurophysiol*, vol. 79, pp. 1450–1460, Mar. 1998.

[185] Perreault, M.-C. and Raastad, M., "Contribution of morphology and membrane resistance to integration of fast synaptic signals in two thalamic cell types," *J Physiol (Lond)*, vol. 577, pp. 205–220, Nov. 2006.

[186] Pervouchine, D., Netoff, T. I., Rotstein, H., White, J. A., Cunningham, M., Whittington, M., and Kopell, N., "Low-dimensional maps encoding dynamics in entorhinal cortex and hippocampus," *Neural Comput*, vol. 18, pp. 2617–2650, Nov. 2006.

[187] Pinto, R., Elson, R., Szucs, A., Rabinovich, M. I., Selverston, A. I., and Abarbanel, H. D. I., "Extended dynamic clamp: controlling up to four neurons using a single desktop computer and interface," *J Neurosci Methods*, vol. 108, pp. 39–48, July 2001.

[188] Piwkowska, Z., Pospischil, M., Brette, R., Sliwa, J., Rudolph-Lilith, M., Bal, T., and Destexhe, A., "Characterizing synaptic conductance fluctuations in cortical neurons and their influence on spike generation," *J Neurosci Methods*, vol. 169, no. 2, pp. 302–322, 2008.

[189] Politecnico di Milano - Dipartimento di Ingegneria Aerospaziale, *RTAI - the RealTime Application Interface for Linux*.

[190] Pospischil, M., Toledo-Rodriguez, M., Monier, C., Piwkowska, Z., Bal, T., Fregnac, Y., Markram, H., and Destexhe, A., "Minimal Hodgkin–Huxley type models for different classes of cortical and thalamic neurons," *Biol Cybern*, vol. 99, pp. 427–441, Nov. 2008.

[191] Potter, S. and Wagenaar, D., "Closing the loop: stimulation feedback systems for embodied MEA cultures," in *Advances in Network Electrophysiology*, Springer Verlag, Nov. 2010.

[192] Prescott, S. A., Ratté, S., De Koninck, Y., and Sejnowski, T. J., "Nonlinear interaction between shunting and adaptation controls a switch between integration and coincidence detection in pyramidal neuron," *J Neurosci*, vol. 26, no. 36, pp. 9084–9097, 2006.

[193] Prescott, S. A., Ratté, S., De Koninck, Y., and Sejnowski, T. J., "Pyramidal neurons switch from integrators in vitro to resonators under in vivo-like conditions," *J Neurophysiol*, vol. 100, pp. 3030–3042, Dec. 2008.

[194] Preyer, A. J. and Butera, R. J., "The effect of residual electrode resistance and sampling delay on transient instability in the dynamic clamp system," *Conf Proc IEEE Eng Med Biol Soc*, vol. 2007, pp. 430–433, 2007.

[195] Preyer, A. J. and Butera, R. J., "Causes of Transient Instabilities in the Dynamic Clamp," *IEEE Trans Neural Syst Rehabil Eng*, vol. 17, no. 2, pp. 190–198, 2009.

[196] Priebe, N. J. and Ferster, D., "Direction selectivity of excitation and inhibition in simple cells of the cat primary visual cortex," *Neuron*, vol. 45, pp. 133–145, Jan. 2005.

[197] Prinz, A. A., Abbott, L. F., and Marder, E., "The dynamic clamp comes of age," *Trends Neurosci*, vol. 27, pp. 218–224, Apr. 2004.

[198] Prinz, A. A., Billimoria, C. P., and Marder, E., "Alternative to hand-tuning conductance-based models: construction and analysis of databases of model neurons," *J Neurophysiol*, vol. 90, pp. 3998–4015, Dec. 2003.

[199] Pugh, J. R. and Raman, I. M., "Potentiation of mossy fiber EPSCs in the cerebellar nuclei by NMDA receptor activation followed by postinhibitory rebound current," *Neuron*, vol. 51, pp. 113–123, July 2006.

[200] Pugh, J. R. and Raman, I. M., "Mechanisms of potentiation of mossy fiber EPSCs in the cerebellar nuclei by coincident synaptic excitation and inhibition," *J Neurosci*, vol. 28, pp. 10549–10560, Oct. 2008.

[201] Raikov, I., Preyer, A. J., and Butera, R. J., "MRCI: a flexible real-time dynamic clamp system for electrophysiology experiments," *J Neurosci Methods*, vol. 132, pp. 109–123, Jan. 2004.

[202] Rall, W., "Distinguishing theoretical synaptic potentials computed for different soma-dendritic distributions of synaptic input.," *J Neurophysiol*, vol. 30, pp. 1138–1168, Sept. 1967.

[203] Raman, I. M., Gustafson, A., and Padgett, D., "Ionic currents and spontaneous firing in neurons isolated from the cerebellar nuclei," *J Neurosci*, vol. 20, pp. 9004–9016, Dec. 2000.

[204] Rancz, E. A., Ishikawa, T., Duguid, I., Chadderton, P., Mahon, S., and Häusser, M., "High-fidelity transmission of sensory information by single cerebellar mossy fibre boutons," *Nature*, vol. 450, pp. 1245–1248, Dec. 2007.

[205] Rinalduzzi, S., Cipriani, A. M., Capozza, M., and Accornero, N., "Postural responses to low-intensity, short-duration, galvanic vestibular stimulation as a possible differential diagnostic procedure," *Acta Neurol Scand*, vol. 123, pp. 111–116, Feb. 2011.

[206] Robinson, H., "A scriptable DSP-based system for dynamic conductance injection," *J Neurosci Methods*, vol. 169, pp. 271–281, Apr. 2008.

[207] Robinson, H. and Kawai, N., "Injection of digitally synthesized synaptic conductance transients to measure the integrative properties of neurons," *J Neurosci Methods*, vol. 49, pp. 157–165, Sept. 1993.

[208] Robinson, H. P. C. and Harsch, A., "Stages of spike time variability during neuronal responses to transient inputs," *Phys Rev E*, vol. 66, p. 061902, Dec. 2002.

[209] Rowat, P., "Interspike Interval Statistics in the Stochastic Hodgkin-Huxley Model: Coexistence of Gamma Frequency Bursts and Highly Irregular Firing," *Neural Comput*, vol. 19, no. 5, pp. 1215–1250, 2007.

[210] Rudolph, M., Guillaume Pelletier, J., Paré, D., and Destexhe, A., "Estimation of synaptic conductances and their variances from intracellular recordings of neocortical neurons in vivo," *Neurocomputing*, vol. 58, pp. 387–392, 2004.

[211] Rudolph, M. and Destexhe, A., "A fast-conducting, stochastic integrative mode for neocortical neurons in vivo," *J Neurosci*, vol. 23, pp. 2466–2476, Mar. 2003.

[212] Rudolph, M. and Destexhe, A., "Tuning neocortical pyramidal neurons between integrators and coincidence detectors," *J Comput Neurosci*, vol. 14, no. 3, pp. 239–251, 2003.

[213] Rudolph-Lilith, M., Piwkowska, Z., Badoual, M., Bal, T., and Destexhe, A., "A method to estimate synaptic conductances from membrane potential fluctuations," *J Neurophysiol*, vol. 91, pp. 2884–2896, June 2004.

[214] Salinas, E. and Sejnowski, T. J., "Impact of correlated synaptic input on output firing rate and variability in simple neuronal models," *J Neurosci*, vol. 20, pp. 6193–6209, Aug. 2000.

[215] Sangrey, T. and Jaeger, D., "Analysis of distinct short and prolonged components in rebound spiking of deep cerebellar nucleus neurons," *Eur J Neurosci*, Oct. 2010.

[216] Sceniak, M. P. and Sabo, S. L., "Modulation of firing rate by background synaptic noise statistics in rat visual cortical neurons," *J Neurophysiol*, vol. 104, pp. 2792–2805, Aug. 2010.

[217] Schiff, S. J., Jerger, K., Duong, D. H., Chang, T., Spano, M. L., and Ditto, W. L., "Controlling chaos in the brain," *Nature*, vol. 370, pp. 615–620, Aug. 1994.

[218] Schiff, S. J. and Sauer, T., "Kalman filter control of a model of spatiotemporal cortical dynamics," *J Neural Eng*, vol. 5, pp. 1–13, Mar. 2008.

[219] Schneidman, E., Freedman, B., and Segev, I., "Ion Channel Stochasticity May Be Critical in Determining the Reliability and Precision of Spike Timing," *Neural Comput*, vol. 10, no. 7, pp. 1679–1703, 1998.

[220] Sharp, A., O'Neil, M., Abbott, L. F., and Marder, E., "Dynamic clamp: computer-generated conductances in real neurons," *J Neurophysiol*, vol. 69, pp. 992–995, Mar. 1993.

[221] Sharp, A., O'Neil, M., Abbott, L. F., and Marder, E., "The dynamic clamp: artificial conductances in biological neurons," *Trends Neurosci*, vol. 16, pp. 389–394, Oct. 1993.

[222] Shelley, M., McLaughlin, D., Shapley, R., and Wielaard, J., "States of high conductance in a large-scale model of the visual cortex," *J Comput Neurosci*, vol. 13, no. 2, pp. 93–109, 2002.

[223] Shen, G., Chen, W., Midtgaard, J., Shepherd, G., and Hines, M. L., "Computational analysis of action potential initiation in mitral cell soma and dendrites based on dual patch recordings," *J Neurophysiol*, vol. 82, pp. 3006–3020, Dec. 1999.

[224] Shin, S. and De Schutter, E., "Dynamic synchronization of Purkinje cell simple spikes," *J Neurophysiol*, vol. 96, pp. 3485–3491, Dec. 2006.

[225] Shin, S., Hoebeek, F., Schonewille, M., De Zeeuw, C. I., Aertsen, A., and De Schutter, E., "Regular patterns in cerebellar Purkinje cell simple spike trains," *PLoS One*, vol. 2, no. 5, p. e485, 2007.

[226] Sohal, V., Pangratz-Fuehrer, S., Rudolph, U., and Huguenard, J., "Intrinsic and synaptic dynamics interact to generate emergent patterns of rhythmic bursting in thalamocortical neurons," *J Neurosci*, vol. 26, pp. 4247–4255, Apr. 2006.

[227] Soofi, W., Archila, S., and Prinz, A. A., "Co-variation of ionic conductances supports phase maintenance in stomatogastric neurons.," *J Comput Neurosci*, pp. –, Dec. 2011.

[228] Sorensen, M., DeWeerth, S., Cymbalyuk, G. S., and Calabrese, R. L., "Using a hybrid neural system to reveal regulation of neuronal network activity by an intrinsic current," *J Neurosci*, vol. 24, pp. 5427–5438, June 2004.

[229] Sourdet, V., Russier, M., Daoudal, G., Ankri, N., and Debanne, D., "Long-term enhancement of neuronal excitability and temporal fidelity mediated by metabotropic glutamate receptor subtype 5," *J Neurosci*, vol. 23, no. 32, pp. 10238–10248, 2003.

[230] Steinmetz, P., Manwani, A., Koch, C., London, M., and Segev, I., "Subthreshold Voltage Noise Due to Channel Fluctuations in Active Neuronal Membranes," *J Comput Neurosci*, vol. 9, no. 2, pp. 133–148, 2000.

[231] Steriade, M., "Impact of network activities on neuronal properties in corticothalamic systems," *J Neurophysiol*, vol. 86, pp. 1–39, July 2001.

[232] Steuber, V. and De Schutter, E., "Passive models of neurons in the deep cerebellar nuclei: the effect of reconstruction errors," *Neurocomputing*, vol. 58-60, pp. 563–568, 2004.

[233] Steuber, V., Schultheiss, N., Silver, A., De Schutter, E., and Jaeger, D., "Determinants of synaptic integration and heterogeneity in rebound firing explored with data-driven models of deep cerebellar nucleus cells," *J Comput Neurosci*, vol. 30, no. 3, pp. 633–658, 2010.

[234] Stuart W Hughes, D. W. C. T. I. T. S. R. W. V. C., "All thalamocortical neurones possess a T-type Ca2+ 'window' current that enables the expression of bistability-mediated activities," *The Journal of Physiology*, vol. 517, pp. 805–151P, June 1999.

[235] Tabak, J. J., Murphey, C. R. C., and Moore, L. E. L., "Parameter estimation methods for single neuron models.," *J Comput Neurosci*, vol. 9, pp. 215–236, Jan. 2000.

[236] Tateno, T. and Robinson, H., "Integration of broadband conductance input in rat somatosensory cortical inhibitory interneurons: an inhibition-controlled switch between intrinsic and input-driven spiking in fast-spiking cells," *J Neurophysiol*, vol. 101, pp. 1056–1072, Feb. 2009.

[237] Telgkamp, P., Padgett, D., Ledoux, V., Woolley, C., and Raman, I. M., "Maintenance of high-frequency transmission at Purkinje to cerebellar nuclear synapses by spillover from boutons with multiple release sites," *Neuron*, vol. 41, no. 1, pp. 113–126, 2004.

[238] Thach, W., "Discharge of Purkinje and cerebellar nuclear neurons during rapidly alternating arm movements in the monkey," *J Neurophysiol*, vol. 31, pp. 785–797, Sept. 1968.

[239] Tien, J. H. and Guckenheimer, J., "Parameter estimation for bursting neural models," *J Comput Neurosci*, vol. 24, pp. 358–373, June 2008.

[240] Tiesinga, P., Jose, J., and Sejnowski, T. J., "Comparison of current-driven and conductance-driven neocortical model neurons with Hodgkin-Huxley voltage-gated channels," *Phys Rev E*, vol. 62, no. 6, pp. 8413–8419, 2000.

[241] Tobin, A. E. and Calabrese, R. L., "Endogenous and half-center bursting in morphologically inspired models of leech heart interneuron," *J Neurophysiol*, vol. 96, pp. 2089–2106, Apr. 2006.

[242] Turrigiano, G., "Hebb and homeostasis in neuronal plasticity," *Current Opinion in Neurobiology*, 2000.

[243] Ullah, G. and Schiff, S. J., "Tracking and control of neuronal Hodgkin-Huxley dynamics," *Phys Rev E*, vol. 79, p. 040901, Apr. 2009.

[244] Ulrich, D. and Huguenard, J., "Gamma-aminobutyric acid type B receptor-dependent burst-firing in thalamic neurons: a dynamic clamp study," *Proc Natl Acad Sci U S A*, vol. 93, pp. 13245–13249, Nov. 1996.

[245] Uusisaari, M., Obata, K., and Knopfel, T., "Morphological and Electrophysiological Properties of GABAergic and Non-GABAergic Cells in the Deep Cerebellar Nuclei," *J Neurophysiol*, vol. 97, pp. 901–911, 2007.

[246] Van Geit, W., Achard, P., and De Schutter, E., "Neurofitter: a parameter tuning package for a wide range of electrophysiological neuron models," *Front Neuroinform*, vol. 1, p. 1, 2007.

[247] van Kan, P., Gibson, A., and Houk, J., "Movement-related inputs to intermediate cerebellum of the monkey," *J Neurophysiol*, vol. 69, no. 1, pp. 74–94, 1993.

[248] van Riel, N. A. W. N., "Dynamic modelling and analysis of biochemical networks: mechanism-based models and model-based experiments.," *Brief Bioinformatics*, vol. 7, pp. 364–374, Dec. 2006.

[249] Vanier, M. C. and Bower, J., "A comparative survey of automated parameter-search methods for compartmental neural models," *J Comput Neurosci*, vol. 7, no. 2, pp. 149–171, 1999.

[250] Verheijck, E., Wilders, R., Joyner, R. W., Golod, D., Kumar, R., Jongsma, H., Bouman, L., and van Ginneken, A., "Pacemaker synchronization of electrically coupled rabbit sinoatrial node cells," *J Gen Physiol*, vol. 111, no. 1, pp. 95–112, 1998.

[251] Vervaeke, K., Hu, H., Graham, L. J., and Storm, J., "Contrasting effects of the persistent Na+ current on neuronal excitability and spike timing," *Neuron*, vol. 49, pp. 257–270, Jan. 2006.

[252] Vida, I., Bartos, M., and Jonas, P., "Shunting inhibition improves robustness of gamma oscillations in hippocampal interneuron networks by homogenizing firing rates," *Neuron*, vol. 49, no. 1, pp. 107–117, 2006.

[253] Voss, H. U., Timmer, J., and Kurths, J., "Nonlinear dynamical system identification from uncertain and indirect measurements ," *International Journal of Bifurcation and Chaos*, vol. 14, pp. 1905–1933, July 2004.

[254] Wagenaar, D. A., Madhavan, R., Pine, J., and Potter, S. M., "Controlling bursting in cortical cultures with closed-loop multi-electrode stimulation," *J Neurosci*, vol. 25, pp. 680–688, Jan. 2005.

[255] Walter, J., "The linear computational algorithm of cerebellar Purkinje cells," *J. Neurosci.*, vol. 26, no. 50, pp. 12861–12872, 2006.

[256] Wang, X. J. and Buzsáki, G., "Gamma oscillation by synaptic inhibition in a hippocampal interneuronal network model.," *J. Neurosci.*, vol. 16, pp. 6402–6413, Oct. 1996.

[257] Wang, Y. and Manis, P., "Temporal coding by cochlear nucleus bushy cells in DBA/2J mice with early onset hearing loss," *J Assoc Res Otolaryngol*, vol. 7, pp. 412–424, Dec. 2006.

[258] Weaver, C., "The role of action potential shape and parameter constraints in optimization of compartment models," *Neurocomputing*, vol. 69, pp. 1053–1057, 2006.

[259] Wehr, M. and Zador, A. M., "Balanced inhibition underlies tuning and sharpens spike timing in auditory cortex," *Nature*, vol. 426, pp. 442–446, Nov. 2003.

[260] Wheeler, D., Kullmann, P., and Horn, J., "Estimating use-dependent synaptic gain in autonomic ganglia by computational simulation and dynamic-clamp analysis," *J Neurophysiol*, vol. 92, pp. 2659–2671, Nov. 2004.

[261] White, J. A., Klink, R., Alonso, A., and Kay, A., "Noise from voltage-gated ion channels may influence neuronal dynamics in the entorhinal cortex," *J Neurophysiol*, vol. 80, pp. 262–269, July 1998.

[262] Wilders, R., "Dynamic clamp: a powerful tool in cardiac electrophysiology ," *J Physiol*, vol. 576, pp. 349–359, July 2006.

[263] Wilent, W. B. and Contreras, D., "Dynamics of excitation and inhibition underlying stimulus selectivity in rat somatosensory cortex," *Nat Neurosci*, vol. 8, pp. 1364–1370, Oct. 2005.

[264] Wolfart, J., Debay, D., Le Masson, G., Destexhe, A., and Bal, T., "Synaptic background activity controls spike transfer from thalamus to cortex," *Nat Neurosci*, vol. 8, no. 12, pp. 1760–1767, 2005.

[265] Wolfart, J. and Roeper, J., "Selective coupling of T-type calcium channels to SK potassium channels prevents intrinsic bursting in dopaminergic midbrain neurons.," *J Neurosci*, vol. 22, pp. 3404–3413, May 2002.

[266] Wylie, D., De Zeeuw, C. I., and Simpson, J., "Temporal relations of the complex spike activity of Purkinje cell pairs in the vestibulocerebellum of rabbits," *J Neurosci*, vol. 15, pp. 2875–2887, Apr. 1995.

[267] Yamamoto, T., Fukuda, M., and Llinás, R., "Bilaterally synchronous complex spike Purkinje cell activity in the mammalian cerebellum," *Eur J Neurosci*, vol. 13, no. 2, pp. 327–339, 2001.

[268] Yaron-Jakoubovitch, A., Jacobson, G., Koch, C., Segev, I., and Yarom, Y., "A paradoxical isopotentiality: a spatially uniform noise spectrum in neocortical pyramidal cells," *Front Cell Neurosci*, vol. 2, p. 3, 2008.

[269] Zheng, N. and Raman, I. M., "Ca Currents Activated by Spontaneous Firing and Synaptic Disinhibition in Neurons of the Cerebellar Nuclei," *J Neurosci*, vol. 29, pp. 9826–9838, Aug. 2009.

[270] Zou, Q., Rudolph, M., Roy, N., Sanchez-Vives, M., Contreras, D., and Destexhe, A., "Reconstructing synaptic background activity from conductance measurements in vivo," *Neurocomputing*, vol. 65, pp. 673–678, 2005.